

Towards turbulence modulation in concentrated solid-liquid flows

by

Yogesh Kumar Agrawal

A thesis submitted in partial fulfillment of the requirements for the degree of

Master of Science

Department of Mechanical Engineering  
University of Alberta

©Yogesh Kumar Agrawal, 2016

## ABSTRACT

There are numerous examples of dispersed turbulent two-phase flows in engineering and environmental processes. In particular, dispersed solid-liquid flows, also known as slurry flows, have many industrial applications such as transportation of coal, ore, and oil sands. Slurry transportation through pipelines is typically highly turbulent in nature. The addition of solid particles affects the turbulence intensity of the liquid phase, which is called turbulence modulation. The physical mechanisms through which particles affect fluid turbulence are poorly understood. Experimental studies on turbulence modulation are limited to low slurry concentration and relatively low Reynolds numbers. No experiments have been conducted to investigate turbulence modulation in coarse particle concentrated slurries at high Reynolds numbers.

In the present study, a non-intrusive optical measurement method, particle image velocimetry, and refractive index matching technique is applied to investigate turbulence modulation in concentrated solid-liquid flow in a large scale vertical pipe loop for a relatively high Reynolds number ( $Re = 198\ 000$ ). Bench scale refractive index matching is performed to investigate the refractive index of the potassium thiocyanate (KSCN) / water solution as function of temperature and concentration, quantitatively and qualitatively. A large scale vertical pipe loop facility is designed and commissioned to handle the corrosive, toxic, and abrasive nature of the concentrated slurry. This project also highlights many of challenges associated with large-scale refractive index matching tests and subsequent data analysis.

## ACKNOWLEDGEMENT

I would like to thank my supervisor Dr. David Nobes and co-supervisor Dr. Sean Sanders for their continuous support, patience and guidance throughout the project. Further, I would like to thank Terry Runyon for her administrative support during my research. Special thanks to Master's student Jake Hadfield and co-op student Parsa Amini to helping me with large-scale vertical loop experiments. I would also like to express my gratitude to Dr. Ryan Spelay from Saskatchewan Research Council to provide valuable suggestion on design and operation of the large-scale vertical loop. I thank to David Breakey for providing valuable feedback on my thesis. I would like to thank my parents, elder brother and younger sister for their moral supports throughout my studies. Finally, thanks to my friends and colleagues at university for their continuous support, friendship and help throughout my studies.

I gratefully acknowledge Natural Sciences and Engineering Research Council (NSERC) of Canada the Alberta Ingenuity Fund, the Canadian Foundation for Innovation (CFI), and the NSERC Industrial Research Chair in Pipeline Transport Processes to funding this project.

# TABLE OF CONTENTS

CHAPTER 1: Introduction .....	1
1.1 Problem Statement .....	1
1.2 Thesis outline .....	7
CHAPTER 2: Literature review.....	9
2.1 Turbulence modulation in slurry flow .....	9
2.2 Particle image velocimetry .....	19
2.3 Refractive index matching .....	24
CHAPTER 3: Bench scale refractive index matching <sup>1</sup> .....	30
3.1 Experimental Methodologies .....	30
3.1.1 Refractometer measurement .....	31
3.1.2 Reflectance measurement .....	33
3.1.3 Refractive index matching in a solid–liquid mixture.....	35
3.2 Results and Discussions .....	35
3.2.1 Refractive index results.....	36
3.2.2 Discussion on reflectance measurement .....	44
3.2.3 Results on index matching for solid-liquid interfaces .....	54
3.3 Properties of index matched fluid.....	59
3.4 Summary and conclusions .....	60

CHAPTER 4: Large scale vertical flow loop for refractive index matching suspensions 62

4.1 Introduction.....	62
4.2 Experimental apparatus and instrumentation for vertical loop.....	65
4.3 Materials .....	69
4.4 Experimental procedure.....	70
4.4.1 Preparation of KSCN solution.....	70
4.4.2 Feeding the solution from mixing tank into the feed tank.....	72
4.4.3 Equalizing the level of feed tank and dampening pot.....	74
4.4.4 Charging solution into the flow loop.....	74
4.4.5 Loading slurry particles .....	76
4.4.6 Pressurization of the loop.....	77
4.4.7 PIV measurement.....	78
4.4.8 Depressurization of the loop.....	78
4.4.9 Unloading the slurry particles.....	79
4.4.10 Unload the solution into storage tank .....	79
4.5 Commissioning of vertical pipe flow loop.....	81
4.5.1 Pressure loss measurement .....	81
4.5.2 Slurry flow rate measurement.....	84
4.6 Pump performance and its compatibility .....	96
4.6.1 Pump selection for RIM loop.....	96
4.6.2 Discussion on pump performance.....	97

4.6.3 Pump incompatibility for vertical loop .....	98
4.7 Summary and conclusion .....	102
CHAPTER 5: Particle image velocimetry in solid-liquid flows.....	104
5.1 PIV set-up .....	104
5.2 PIV in single phase flow .....	106
5.2.1 Checking for fully developed flow .....	106
5.2.2 Convergence criteria .....	111
5.2.3 Mean velocity profile.....	114
5.2.4 Turbulence statistics.....	117
5.3 PIV in solid-liquid flow .....	120
5.3.1 PIV without RIM .....	120
5.3.2 PIV with RIM .....	121
5.3.3 Pump incompatibility during measurement .....	123
5.4 Flow around a slurry particle .....	126
5.5 Summary and conclusion.....	132
CHAPTER 6: Conclusions and recommendations .....	134
6.1 Conclusions.....	134
6.2 Recommendations.....	138
REFERENCES .....	140

Appendix.....	145
Appendix A1: Clean-up procedure of the loop with fresh water.....	145
Appendix A2: Reference check list to operate slurry loop.....	146
Appendix A3: Standard operational procedure for pressure loss measurement.....	147

## LIST OF TABLES

Table 2.1: Properties of salt solutions , rated on the scale of 0-5, 0 = the lowest level ....	26
Table 2.2: An overview of aqueous potassium thiocyanate as index matched fluid .....	27
Table 3.1: Refractive index of water at different temperatures .....	36
Table 3.2: Properties of index matched KSCN solution at 25 °C.....	60
Table 4.1: Key changes in present and past made vertical flow loop.....	64
Table 4.2: Safe work procedure to prepare KSCN solution .....	71
Table 4.3: Procedure of feeding the solution from mixing tank into the feed tank .....	73
Table 4.4: Procedure of equalizing the level of feed tank and dampening pot.....	74
Table 4.5: Procedure of charging solution into the flow loop .....	75
Table 4.6: Standard operating procedure for loading slurry particles .....	76
Table 4.7: Procedure for pressurization the loop .....	77
Table 4.8: Procedure for PIV measurements .....	78
Table 4.9: Standard operating procedure to depressurize the loop.....	78
Table 4.10: Procedure of unloading the slurry particles .....	79
Table 4.11: Procedure to unload the solution into storage tank.....	79
Table A.1: Check list of valves at different step in procedure.....	146

## LIST OF FIGURES

Figure 2.1: Classification of experimental methodologies in two-phase systems [1] .....	19
Figure 2.2: Sample PIV image having flow around a rising air bubble in two phase flow [23].....	22
Figure 3.1: Experimental schematic of reflectance method.....	33
Figure 3.2: Refractive indices of sodium iodide solutions (a) Present and Bai and Katz [31] measurements at 23°C (b) present and Narrow et al. [49] studies at 25 °C .....	38
Figure 3.3: KSCN solution refractive index varying with salt concentration and solution temperature .....	39
Figure 3.4: Refractive index of KSCN solution as a function of temperature of the solution and salt concentration levels .....	40
Figure 3.5: Surface plot to show variation in refractive index of KSCN solution with different temperatures and salt concentrations .....	41
Figure 3.6: KSCN solution refractive index on empirical model at 25 °C .....	42
Figure 3.7: KSCN refractive index experimental data on fitted empirical model for concentration range 60 - 70 % .....	43
Figure 3.8: Signal and reference beam intensity in pixel space at (a) 10% (b) 60% concentrated KSCN solution.....	45
Figure 3.9: Percent reflectance for (a) <i>s</i> -polarized (b) <i>p</i> -polarized (c) un-polarized light from solid Pyrex slide in different refractive index of KSCN solution based on Fresnel equations .....	50
Figure 3.10: Signal to reference intensity ratio versus KSCN refractive index at 23° C .	52

Figure 3.11: Calibration target in packed bed beads for KSCN concentration (a) 60.8%	
(b) 62.4 (c) 64.3 (d) 68.2 w/w .....	55
Figure 3.12: Gradient of KSCN and NaI solution for concentration sensitivity .....	57
Figure 3.13: Refractive index matched KSCN solution for temperature sensitivity .....	58
Figure 3.14: Variation in shear stress with shear rate for index matched fluid .....	59
Figure 4.1: Isometric view of 50 mm vertical loop facility for RIM suspensions.....	66
Figure 4.2: Layout of experimental vertical loop facility .....	72
Figure 4.3: Variation in measured and calculated pressure loss with bulk velocity for	
water.....	83
Figure 4.4: Variation in flow rates of water for (a) upstream and (b) downstream flow	
meter for certain time period.....	86
Figure 4.5: Distribution of flow rate for (a) upstream flow meter ( $Q_{avg}=225.3$ ) (b)	
downstream flow meter ( $Q_{avg}=223.5$ ).....	87
Figure 4.6: Variation of flow rate with time for water and 3 mm beads in very dilute	
slurry using upstream flow meter .....	88
Figure 4.7: Variation in flow rate for upstream and downstream flow meters $\phi_v = 5\%$ and	
3 mm beads slurry over certain loop cycles.....	90
Figure 4.8: Flow rate comparison for 3 mm size slurry concentrations (a) $\phi_v = 0.05$ (b) $\phi_v$	
= 0.15 .....	91
Figure 4.9: Flow rate variation with time for two different size of slurry in upstream flow	
meter .....	94
Figure 4.10 : Pump performance for water before and after running a set of experiments	
with 3 mm size RIM slurry .....	97

Figure 4.11: (a) New and (b) Scratched/damaged 3 mm size Borosilicate beads .....	99
Figure 4.12: Upstream transparent section of loop (a) before adding particles (b) after adding particles into loop (c) fine and coarse residue of lobe from rotary pump...	100
Figure 4.13: New Borosilicate beads in (a) DI Water (b) RIM solution and (c) damaged beads in RIM solution.....	101
Figure 5.1: Optical PIV measurement system .....	105
Figure 5.2: PIV measurement streamwise location (a) Position 1: $85D$ (b) Position 2: $90D$ above the bottom bend position of the loop.....	107
Figure 5.3: Normalized mean velocity profile in streamwise direction at Reynolds number (a) 118 000, (b) 164 000, and (c) 236 000 for two measurement locations .....	108
Figure 5.4: Normalized mean axial velocity profile at (a) position 1: $85D$ (b) position 2: $90D$ for three different Reynolds numbers .....	110
Figure 5.5: Measured mean axial velocity averaged over a finite number of PIV images .....	112
Figure 5.6: Measured fluctuating velocity (a) $u^2$ (b) $v^2$ (c) $uv$ averaged over a finite number of PIV images .....	113
Figure 5.7: Mean streamwise velocity profiles for water at $Re = 198\ 000$ .....	115
Figure 5.8: Variation in mean radial velocity in cross-streamwise direction. ....	116
Figure 5.9 (a) Streamwise Reynolds normal stress (b) Radial Reynolds normal stress (c) Reynolds shear stress velocity profiles for single phase water.....	118
Figure 5.10: Raw PIV images for concentrated non-RIM slurry.....	121
Figure 5.11: Raw PIV image for concentrated RIM slurry .....	122

Figure 5.12: PIV image number (a) 100 (b) 1000 (c) 5000 collected using RIM technique  
for 5 % concentrated RIM slurry ..... 124

Figure 5.13: (a) Flow field around a bead in Eulerian reference frame (b) flow field  
around a bead relative to its own velocity in Lagrangian reference frame at bead  
centre radial location  $y/R = 0.09$  ..... 127

Figure 5.14: (a) Flow field around a bead in Eulerian reference (b) flow field around a  
bead relative to its own velocity in Lagrangian reference at bead centre radial  
location  $y/R = -0.43$  ..... 128

Figure 5.15: (a) Flow field around a slurry bead in Eulerian reference (b) flow field  
around a bead relative to its own velocity in Lagrangian reference at bead centre  
radial location  $y/R = -0.61$  ..... 129

Figure 5.16: (a) Flow field around a bead in Eulerian reference (b) flow field around a  
bead relative to its own velocity in Lagrangian reference at bead centre radial  
location  $y/R = -0.80$  ..... 130

## LIST OF NOMENCLATURE

Symbol	Descriptions	Units
$A$	Cross sectional area	$\text{mm}^2$
$Ar$	Particle Archimedes number	-
$c$	Mass concentration	w/w
$C_d$	Drag coefficient	-
$D$	Pipe inner diameter	mm
$d$	Slurry particle diameter	mm
$f$	Fanning friction factor	-
$g$	Gravitational acceleration	$\text{m/s}^2$
$I$	Turbulent intensity	-
$L$	Characteristic length of the geometry	m
$l_e$	Turbulent length scale	mm
$l$	Length of pipe section	m
$M$	Turbulence modulation	-
$m$	Sample number	-
$N$	Image number	-
$n$	Refractive index	-
$N_d$	Number density	-
$P$	Pressure	kPa
$\Delta P$	Pressure loss	kPa

$Pa$	Particle momentum number	-
$Q_{avg}$	Average volumetric flow rate	L/min
$Q$	Volumetric flow rate	L/min
$R$	Pipe radius	mm
$R_x$	Reflectance	-
$Re_p$	Reynolds number for the particle	-
$Re$	Reynolds number for pipe flow	-
$\frac{S}{S_R}$	Signal to reference intensity ratio	-
$St$	Stokes number	-
$t$	Time	s
$T$	Temperature	°C
$U$	Axial average velocity	m/s
$U_c$	Axial centerline average velocity	m/s
$U_\tau$	Friction velocity	m/s
$U_{max}$	Axial maximum average velocity	m/s
$u$	Axial fluctuating velocity	m/s
$V$	Mean or Bulk velocity of pipe flow	m/s
$V_\infty$	Terminal settling velocity	m/s
$V_s$	Slip velocity	m/s
$V_r$	Radial average velocity	m/s
$v$	Radial fluctuating velocity	m/s

$x$	Axial coordinate position	mm
$y$	Radial coordinate position	mm
$\tau_p$	Particle response time	s
$\tau_f$	Fluid characteristic time	s
$\eta$	Kolmogorov length scale	mm
$\rho$	Density of fluid	Kg/m <sup>3</sup>
$\rho_s$	Density of solid (slurry particles)	Kg/m <sup>3</sup>
$\mu$	Dynamic viscosity	Pa-s
$\lambda$	Wavelength	nm
$\phi_v$	Volumetric concentration	v/v
$\varepsilon$	Pipe wall equivalent roughness	mm
$\tau_w$	Wall shear stress	Pa
$\sigma$	Shear stress of fluid	Pa
$\dot{\gamma}$	Shear rate	s <sup>-1</sup>

## Acronyms

<b>EFM</b>	Electromagnetic flow meter
<b>KSCN</b>	Potassium thiocyanate
<b>LDV</b>	Laser Doppler anemometry
<b>NaI</b>	Sodium iodide
<b>PIV</b>	Particle image velocimetry
<b>PTV</b>	Particle tracking velocimetry
<b>PDV</b>	Phase Doppler velocimetry
<b>RIM</b>	Refractive index matching

# CHAPTER 1: INTRODUCTION

## *1.1 Problem Statement*

Single phase turbulence has been a focus of extensive research for many years. Researchers still find it difficult to model and quantify turbulence and its impact on mass, momentum and energy transfer; especially at high Reynolds number [1, 2]. Turbulent flow is characterized by irregularity or randomness in the flow, large Reynolds number, and a high level of fluctuating vorticity. Transport phenomena such as rapid mixing and enhancement in the rate of mass, momentum, and energy transfer are explained by the high diffusivity of turbulent flow [3]. In the context of turbulent flows, multiphase systems become highly challenging in term of their fluid dynamics [4]. The understanding of turbulence in a multiphase flow is still at an early stage because the correct formulation of the governing equations continues to be debated [1].

A multiphase flow is defined as flow consisting of two or more phases. Such flows are categorized into gas-liquid, solid-liquid, solid-gas, and three-phase flows [1]. Turbulent multiphase flows are encountered in engineering and environmental systems [4]. Natural phenomenon such as rain, mud slides, sediment transport, and debris flows come under the category of environmental applications of multiphase flows [5]. Multiphase flows also occur in industrial and chemical processes such as injection, sprays, chemical or combustion [6]. Examples of industrial applications include

pneumatic conveying, slurry pipeline transport, fluidized beds, bubble columns, and hydrocyclones [1].

The present study focuses specifically on dispersed solid-liquid flows (also known as slurry flows). Slurry flows have important applications ranging from the transportation of coal, ore, and oil sands by pipelines to the flow of mud [1]. These types of flows are often turbulent in nature [4]. A slurry flow can either be homogenous or heterogeneous in nature based on its innate particle size. Homogenous slurries are generally comprised of fine particles whereas heterogeneous slurries are composed of coarse particles. In homogenous slurries, the turbulence of the liquid phase keeps the particles in suspension. Heterogeneous slurries have a tendency to settle to the bottom of the pipe [7]. The current study focuses on heterogeneous slurries where coarse particles are investigated.

Slurry flows are further classified into a dilute and dense flow depending on the particle concentration. When the particle volume fraction ( $\phi_v$ ), defined as solid particle volume to total mixture (solids + liquid) volume, falls below  $10^{-3}$ , the flow is called dilute. A dense slurry has particle concentrations of more than  $10^{-3}$  [8]. Dense slurry can vary in concentration from low (0.1 %) to high (50 %) by volume. Such dense heterogeneous slurry flows are discussed and studied in this thesis. Solid-liquid systems are poorly understood due to inherent gap in the knowledge of concentrated solid-liquid flows which leads to design inefficiency in solid-liquid systems in industrial applications. For example, deficiency in design can result in operational issues and ineffective utilization of resources like oversized or undersized pumps and other accessories [9].

Bulk flow quantities such as deposition velocity, pressure drops, in-situ and delivered concentrations, average velocities etc. are important parameters to design solid-liquid pipeline systems. There have been numerous studies to understand bulk properties of solid-liquid flow [10]. Additionally, significant data has been accumulated for bulk flow quantities over the years. However, the knowledge required to design efficient solid-liquid slurry systems is still limited [9]. This is due to the lack of understanding of the physical mechanisms that governs dispersed turbulent slurry flows. Physical mechanisms are understood by detailed measurements of solid-liquid flows. Detailed measurements not only include bulk quantities but also consider local properties like mean and fluctuating velocities and Reynolds stress distribution for continuous and dispersed phases [11].

Depending on the application, slurry pipelines can be horizontal, vertical or inclined in configuration. Vertical slurry pipe flow is studied in the present research mainly for two reasons. First, the flow mechanism is much less complicated in vertical pipelines than in horizontal ones due to asymmetric structure of flow created by gravity in horizontal pipelines. The physical mechanism of flow can be understood more easily by avoiding asymmetric structure found in horizontal pipes [12]. Second, there have been fewer vertical flow experiments discussed in literature to investigate local properties of slurry flow [10]. It provides the motivation to design and build a vertical flow pipe loop to explore turbulence in solid-liquid flows.

The structure of turbulence in solid-liquid flow is quite complicated due to complex interaction between continuous and dispersed phases [4]. The presence of solid particles influences the turbulence level of the liquid phase in solid-liquid flows. A

change in the turbulence intensity of the liquid in the existence of the dispersed phase is called turbulence modulation [13]. Turbulence modulation is based on a critical parameter, defined as ratio of the particle size ( $d$ ) to the turbulent length scale ( $l_e$ ) [13]. This critical parameter only tells about increments or decrements in turbulence intensity but does not relate turbulence modulation qualitatively [14]. It is commonly advised that value of  $d/l_e$  below 0.1 tends to decrease the turbulence intensity. Whereas, enhancement in turbulence augmentation is recorded for  $d/l_e > 0.1$  [15]. It is generally accepted that turbulence intensity of the liquid phase is attenuated by small size particles and enhanced by large particles [15]. However, particle concentrations, length or time scale of turbulence, and relative velocity between both the phases can also have a huge impact on turbulence modulation [16].

In the context of turbulent two-phase flows, heat and momentum transfers of the continuous phase become strong dependent on dispersed phase or particles [14, 17, 18]. Researchers argue that since smaller particles are smaller than energetic eddies in the slurry flow, a part of the energy is supplied to particles through drag force. Turbulence energy is hence transformed into the kinetic energy of particles that attenuates the turbulence intensity. Large particles enhances the turbulent intensity since turbulence is created in the wake region generated by particles, in which scale of both wake region and energetic eddies are close [13].

So far, experimental studies have been conducted to measure turbulence modulation for relatively small particles, dilute flows and relatively low Reynolds number [11, 19, 20]. Based on the literature, no experiments have been conducted to investigate the turbulence modulation for coarse particles and concentrated slurries at

high Reynolds number. It provides additional motivation to measure turbulence statistics for concentrated solid-liquid flow. Additionally, analytical and numerical simulations are also limited to low particle concentrations and relatively low Reynolds numbers due to the complex turbulence structure in dispersed two phase flows.

Quantification of turbulence modulation is estimated by measuring the local flow quantities such as mean and turbulent intensity of solid and liquid phases in dispersed phase flow. Local flow properties are usually measured by application of optical measurement techniques [1]. Examples of non-invasive classical optical measurement techniques are laser Doppler velocimetry (LDV), particle image velocimetry (PIV), and particle tracking velocimetry (PTV). Laser Doppler velocimetry (LDV) has been used to measure local flow quantities in low concentrated dense flows [10, 12]. Particle image velocimetry (PIV) has become a common spatially resolved and non-intrusive technique, largely replacing LDV for flow visualization in experimental flow studies [4].

In PIV, a laser light sheet illuminates the flow having seeding or tracer particles. The velocity field of the fluid is calculated by measuring the displacement of seeding particles over a fixed time delay between two laser light pulses [21]. PIV has been used to investigate flow visualization and quantitative flow measurements mainly in single phase flows. However, PIV measurements for the dispersed slurry flows are comparatively more difficult than that of single-phase flows. In solid-liquid flow, light refracts and reflects through the solid-liquid interfaces that restricts optical access. Solid-liquid interface further creates significant light scattering and generating light flare [22]. However, significant advances have been made in the application of PIV in low

concentration dense two-phase flows using special phase discrimination and processing techniques to remove solid-liquid interface [23].

PIV in conjunction with phase discrimination and processing techniques does not work for concentrated slurries ( $\phi_v > 5-10\%$ ) since excessive solids completely block the optical path to the measurement location [24]. Additionally, each solid-liquid interface also leads to minor variation in the refractive index that leads to reflection/refraction from interface boundary. The method to eliminate solid-liquid interface consists in matching the refractive index of solid and liquid to achieve optical transparency and accessibility in slurry flows. In past, the refractive index matching (RIM) method has been implemented to provide optical access in a variety of flow visualization applications, more recently in concentrated suspensions [25]. In this study, RIM technique in combination with PIV is implemented to study turbulence modulation for concentrated particle suspensions.

In the RIM technique, the refractive index of the dispersed phase is matched with corresponding continuous phase or liquid. Various organic and inorganic index-matched solutions such as zinc iodide, sodium iodide, alcohols, and mineral oil are used to achieve optical transparency [26]. Index-matched fluid selection is based on parameters like toxicity, flammability, reactivity, viscosity, density, and cost selection for a particular application [26]. Aqueous sodium iodide (NaI) solution is widely used as an index-matched in concentrated particle suspensions [27, 28]. Additionally, extensive research has been completed to comprehend the properties of sodium iodide in the literature. Nevertheless, it seems that there have been no previous studies to understand the properties of the alternative index-matched fluid, aqueous potassium thiocyanate

(KSCN), especially with regards to refractive index. However, aqueous KSCN has been used in a few studies as an index-matched fluid [29, 30]. Potassium thiocyanate salt has a benefit over sodium iodide salt in term of toxicity and cost. Additionally, KSCN solutions are colorless whereas NaI solutions are yellowish due to its exposure with oxygen [31]. It has motivated to do a complete study on the refractive index of KSCN solutions at different temperatures and concentrations to use as index-matched fluid for future studies.

Present study has following research objectives:

- To measure the refractive index of an alternative refractive index matching fluid, aqueous KSCN, at different temperatures and concentrations and to compare it with a commonly used index-matched fluid, aqueous NaI;
- To determine the exact concentration of KSCN solution for index matching with borosilicate beads by conducting bench scale refractive index matching experiments;
- To design, commission, and operate a larger-scale vertical slurry flow loop that can be used to safely test the toxic, corrosive, and abrasive nature of index matched suspensions for turbulence modulation studies in concentrated solid-liquid flows.

## ***1.2 Thesis outline***

This dissertation is organized into six chapters. Chapter 2 provides a review of the past literature on turbulence modulation in solid-liquid flows. The background theory related to PIV and RIM are summarized for slurry flows. Chapter 3 deals with

experimental methods used to achieve bench scale refractive index matching. Experimental methodologies include refractometer measurements, reflectance measurements, and refractive index matching performance with a solid-liquid mixture. This chapter gives confidence in implementing the index matching technique for the measurement of turbulence statistics on a pilot-scale vertical slurry pipe loop. Chapter 4 presents the details of the large-scale vertical pipe loop facility designed for refractive index matching to safely test the toxic, corrosive, and abrasive nature of solid-liquid flow for turbulence measurements. Experimental difficulties and challenges especially due to slurry pump failure are also explained in Chapter 4. Experimental PIV results are analyzed in Chapter 5 for mean and turbulence statistics in single phase flow. Additionally, general features of PIV images in conjunction with index matching technique are discussed for solid-liquid flow in Chapter 5. Finally, Chapter 6 gives major contributions from the present study and provides recommendations for future work to augment the research in turbulent dispersed solid-liquid flow.

## CHAPTER 2: LITERATURE REVIEW

In present study, the primary objective is to investigate the turbulence modulation in concentrated solid-liquid flow. To achieve this goal, a classical optical method, PIV, and refractive index matching technique are implemented to analyze the effect of particles (dispersed phase) on fluid turbulence. This chapter is divided into three sections. First, turbulence modulation in solid-liquid flows is reviewed. Second, PIV is discussed and the difficulties associated with PIV in two-phase flow, especially in slurry flows, are discussed. Third, a review of the refractive index matching technique is provided in detail for facilitating the application of modern optical measurement methods. Some examples are suggested for using refractive index matching in combination with optical measurement techniques in concentrated slurry flows. Additionally, a detailed literature review on the unconventional index-matched fluid KSCN solution is studied.

### *2.1 Turbulence modulation in slurry flow*

Turbulence modulation is defined as change in turbulence intensity of carrier or continuous phase in the existence of a dispersed phase in two-phase flows. The change in turbulence intensity or turbulence modulation is defined by [15]:

$$M = \frac{I_{TP} - I_{SP}}{I_{SP}} \quad (2.1)$$

where  $M$  is turbulent modulation and  $I$  is the turbulence intensity. The subscripts  $SP$  and  $TP$  are designated to single and two phase, respectively.

For pipe flows, the axial turbulence intensity of a fluid is given by [15]:

$$I_x = \frac{\sqrt{\langle u^2 \rangle}}{U} \quad (2.2)$$

where  $U$  and  $u$  are the local average axial velocity and axial velocity fluctuations of the fluid phase, respectively. Mean square local axial velocity fluctuations are denoted by  $\langle u^2 \rangle$ .

In the same way, turbulence intensity of the continuous phase in radial direction is specified by:

$$I_r = \frac{\sqrt{\langle v^2 \rangle}}{U} \quad (2.3)$$

where  $v$  denotes velocity fluctuations of the fluid in radial direction.

Crowe and Gore [15] proposed a physical model by combining all the past studies to find change in fluid turbulence intensity due to presence of solid particles in dispersed two-phase flow. They compiled all the available experimental data on turbulence modulation in two-phase flows. Based on their model, they defined a critical length scale ratio. This critical ratio is specified by  $d/l_e$  along the centerline of the flow [15].

They [15] plotted variation in turbulence intensity against the ratio of particle diameter and integral turbulent length scale to comprehend the particles' effect on fluid turbulence. They showed that with the exception of a few data points,  $\frac{d}{l_e} \simeq 0.1$  is the demarcation point that decides turbulence augmentation or attenuation in the presence of particles [13, 15]. This parameter is valid only along the centerline of the flow. Turbulence enhancement (termed augmentation) will occur for  $d/l_e > 0.1$ , whereas turbulence suppression (termed attenuation) will happen at  $d/l_e < 0.1$ . Turbulent intensity

of fluid is increased in presence of large size particles. Whereas, turbulence fluctuations of the fluid phase are suppressed by small size particles. Turbulence length scale ( $l_e$ ) was defined from the work of Hutchinson et al. [32] for single-phase fully-developed pipe flows. They suggested that the characteristic turbulent length scale for fully developed pipe flow is equal to  $0.1 D$  excluding near wall [32]. Turbulent length scale was defined as size measurement of the most energetic eddies. This critical ratio ( $d/l_e$ ) only provides the criteria whether fluid turbulent intensity will be enhanced or suppressed in presence of particles but not how much [15]. They further argued that this critical parameter was satisfied for different flow conditions in two-phase flows. However, it was impossible to check consistency of the critical parameter due to inadequate available experimental data [15].

Crowe and Gore [33] further extended their work to investigative variation in the fluid turbulence at different radial positions due to addition of particles as dispersed phase. They also examined the consequence of additional non-dimensional parameters on fluid turbulence. They suggested that critical length scale ratio increases near to the pipe wall. It means that the centerline critical  $d/l_e$  ratio is approximately 0.10 in comparison to near wall critical ratio 0.30 at  $y/R = 0.90$  (near to wall). It is also interesting to point out that turbulent intensity fluctuation decreased towards the pipe wall due to anisotropic nature of turbulence [33].

The critical ratio is the most suitable parameter to analyze the turbulence modulation in two-phase flows, reported by Crowe and Gore [33]. However, this critical ratio doesn't quantify turbulence augmentation and attenuation of carrier phase. They further analyzed the past experimental works to quantify turbulence modulation with the

addition of particles. They further argued that carrier phase turbulent intensity can be attenuated or augmented due to various parameters that include: slip velocity between disperse and continuous phases, fluid phase properties such as density and viscosity, fluid velocity, particle size, density, and their concentration, fluid turbulent length and time scale. Turbulence modulation ( $M$ ) can be a function of non-dimensionless parameters that are combined as [33]:

$$M = f\left(\frac{\rho_s}{\rho}, Re, Re_p, \frac{l_e}{d}, \phi_v, \frac{\sqrt{\langle u^2 \rangle}}{V_s}\right) \quad (2.4)$$

In above function (2.4),  $\rho_s$ ,  $d$ , and  $\phi_v$  are particle density, diameter, and volumetric concentration, respectively. Additionally,  $\rho$  and  $\mu$  denote the fluid density and dynamic viscosity, respectively. Flow Reynolds number ( $Re$ ) and particle Reynolds number ( $Re_p$ ) is given by [33]:

$$Re = \frac{\rho V D}{\mu} \quad (2.5)$$

$$Re_p = \frac{\rho d V_s}{\mu} \quad (2.6)$$

Here,  $D$  denotes pipe diameter to specify the flow Reynolds number.  $V$  and  $V_s$  indicate bulk velocity and slip velocity of the flow, respectively. Nevertheless, Crowe and Gore [33] were not able to find a direct relationship between turbulence modulation and the above mentioned parameters based on past experimental studies for dispersed two phase flows.

There has been no physical model to accurately predict the turbulence modulation in presence of particles for discrete two phase flows, claimed by Tanaka and Eaton [34]. They further argued that just one parameter such as critical length scale ratio defined by Crowe and Gore [15] cannot observe turbulence modulation effect accurately. They examined previously conducted turbulence modulation experiments in two phase internal flows. Finally, they provided the physical model by defining a dimensionless parameter called particle momentum number defined by [34] as:

$$Pa = St Re^2 \left(\frac{\eta}{L}\right)^3 \quad (2.7)$$

Here,  $\eta$ ,  $L$  denote Kolmogorov length scale and the characteristics length of geometry. Stokes number ( $St$ ) is represented in term of the ratio of response time of the particle ( $\tau_p$ ) to the fluid characteristic time ( $\tau_f$ ) specified by [33] where  $l_e$  is characteristics length scale of most energetic eddies:

$$St = \frac{\tau_p}{\tau_f} = \frac{\rho_s d^2 V}{18\mu l_e} \quad (2.8)$$

Based on their compiled data with their new dimensionless parameter, they reported that decrease in turbulence intensity occurs for particle momentum number in the range  $3 \times 10^3 \leq Pa \leq 10^5$ . Turbulence augmentation was noticed for  $Pa \leq 3 \times 10^3$  and  $Pa \geq 10^5$  with the addition of dispersed phase in two-phase flows. However, their model did not account for any turbulence modulation measurements for two-phase flows with  $Re > 30\,000$ . It shows that only few data sets are available to define a physical model based on dimensionless parameters [4].

It is clear from the literature review that there is no appropriate physical model to quantify turbulence modulation. This is due to the fact that experimental studies on turbulence modification are limited to simplified conditions and relatively low Reynolds numbers in dispersed two-phase flows. It is worth mentioning that out of all available experimental work; turbulence modification is mostly focused for gas-solid flows in past research studies. There have been few studies investigating the change in turbulence fluctuations in the presence of particles for solid-liquid flows.

For example, Tsuji et al. [12] investigated turbulence modification in a vertical pipe with dispersed gas-solid flow. Experiments were performed using LDA for low Reynolds number and low particle concentrations. Turbulence modulation was measured for different particle sizes ranging from 0.2 to 3.0 mm. It was observed that turbulence intensity decreased due to small size particles whereas augmentation in turbulence fluctuation was noticed for large particles [12]. In another study, Kulick et al. [35] inspected turbulence modulation for a solid-gas flow in a downward rectangular channel. They measured turbulence statistics for the carrier phase (air) and particles ranging from 50-90  $\mu\text{m}$  size at particle concentrations up to 0.04% at  $Re = 13\ 800$  using LDA. It was reported that carrier phase fluid turbulence was decreased by presence of particles. They also noticed that turbulence intensity reduced more with increased particle Stokes number and volumetric concentration [35].

Lee and Durst [36] used LDA to study turbulence modulation in dispersed gas-solid flow at  $Re = 8000$ . They showed significant enhancement in stream-wise turbulence intensity at pipe centre in the presence of 0.8 mm size solids. Some other experimental studies also examined turbulence statistics of disperse and continuous phase to

investigate the turbulence modulation effect in solid-gas flow. All these experiments were performed at relatively low Reynolds number, with different size of particles and low volume fraction in turbulent dispersed gas-solid pipe/channel flow [18, 37, 38].

There have been few experimental studies to explore turbulence modulation in dispersed solid-liquid flows. For example, Zisselmar and Molerus [39] measured turbulence modulation in a 50 mm horizontal slurry pipe flow for small size particles at  $Re = 100\ 000$ . Mean velocities and turbulence statistics of the both the phases were measured using LDA for the turbulent suspension having 53  $\mu\text{m}$  size particles and up to 5.6 % particle concentration. They observed that small particles ( $d = 53\ \mu\text{m}$ ) attenuated the liquid turbulence. They explained the turbulence suppression phenomenon by comparing the particle diameter and scale of turbulence. Particles followed the flow of turbulent fluctuations as particle diameter is smaller than scale of the turbulence. Additionally, increasing particle concentration further attenuates the carrier phase turbulence fluctuations in most of the pipe section.

Phase distribution and turbulence structure were studied by Alajbegovic et al. [11] in an upward vertical solid-liquid pipe flow. Turbulence statistics were estimated for dispersed and continuous phase for three Reynolds numbers lower than 68 000 using LDA. Experiments were performed for two types of particles having different specific gravity with approximate size of 2 mm in diameter. Ceramic and polystyrene particles were chosen as dispersed phase for this study. Results suggested that the axial turbulence intensity of the liquid phase had strong augmentation near to the wall for both types of particles. Magnitude of axial turbulent fluctuation for liquid phase did not change significantly with variation in Reynolds number at pipe centre for ceramic particles. A

small effect was observed in stream-wise liquid phase turbulence with change in Reynolds number for polystyrene particles. They further explained minor turbulence modulation occurring in radial turbulent intensity near to pipe centreline with Reynolds numbers. In conclusion, liquid phase turbulence does not change significantly with particle density and concentration range 0.9 - 3.6 % tested by Alajbegovic et al. [11].

The interaction between the dispersed phase and fluid turbulence for slurry flows was investigated by Sato et al. [19] using PIV in a downward channel. Experiments were conducted for particles sized 0.34 and 0.5 mm with volumetric concentration ranging from 0.2 - 1.3 % at  $Re = 5000$ . They observed that the turbulence intensity of continuous phase was augmented due to addition of dispersed phase. It is due to the fact that the particles were slightly greater than the Kolmogorov length scale. Continuous phase (fluid) turbulence was enhanced more in the streamwise direction than cross-streamwise direction in the channel flow for two-phase flows. Additionally, fluid phase Reynolds shear stress increased in particle-laden flow in comparison with un-laden flow due to increases in turbulent kinetic energy. There was streamwise fluid turbulence intensity enhancement in the core region of the pipe flow whereas negligible effect was noticed in near wall region. It was also observed that the fluid turbulence intensity augmented with an increase in particle concentration [19].

Kiger and Pan [20] examined the effect of dispersed phase on fluid turbulence for solid-liquid flows in a horizontal channel. Measurements were performed for 0.195 mm particles having volumetric concentration of 2.4 % using PIV at a Reynolds number of 25 000. They reported that streamwise and cross-streamwise liquid velocity fluctuations were increased by around 8 - 10% in central zone of the channel flow. They further

found that the dispersed phase composed of glass particles heavier than water augmented the carrier fluid turbulence. They also plotted streamwise and cross-streamwise turbulence statistics in wall units. It was noticed that turbulence intensity was comparable or slightly higher in particle-laden flow than in un-laden flow. It was due to the significant increment in friction velocity that decreased the magnitude change in the fluid turbulence level. Additionally, streamwise, cross-streamwise turbulent stress, and Reynolds shear stress had the same trend in their velocity profiles. It means that axial and radial fluid fluctuating velocities were increased in the central zone of the flow due to addition of particles. Moreover, it is worth mentioning that the streamwise fluid fluctuation attenuated significantly in near-wall region [20].

Hosokawa and Tomiyama [14] studied continuous phase turbulence modulation in presence of particles in vertical solid-liquid pipe flow. Experiments were performed with coarse particles ( $d = 1, 2.5, \text{ and } 4 \text{ mm}$ ) and particle concentration ranging from 0.7% to 1.8% in solid-liquid flow. LDV was implemented to investigate turbulence intensity of particle and fluid at  $Re = 15\,000$ . In the core region of the pipe flow, fluid turbulence was enhanced in streamwise direction, observed by Hosokawa and Tomiyama [14]. It was also reported that there was augmentation in fluid turbulence with an increase in particle size. Their experimental data satisfied the critical parameter of  $d/l_e = 0.1$  but they suggested better non dimensional parameter based on ratio of turbulence modulation and number density ( $N_d$ ). In dispersed two-phase flows, number density ( $N_d$ ) is defined by [14]:

$$N_d = \frac{6\phi_v}{\pi d^3} \quad (2.9)$$

They argued that carrier phase turbulence modulation would increase with  $N_d$ . That is the reason it is more appropriate to consider turbulence change per unit number density ( $M/N_d$ ) instead of just turbulence modulation defined by Crowe and Gore [15].

Recently, Kameyama et al. [16] investigated the turbulent flow structure in dispersed solid-liquid flow in upward/downward pipe flow at  $Re = 19\,500$ . Mean and fluctuating velocities profiles of both the phases were measured by PTV. This study was conducted on glass particles with 0.625 mm diameter having very low particle concentration of 0.6 %. They observed that the axial turbulent intensity was enhanced due to addition of particles in the downward pipe flows. It is due to fact that Kolmogorov turbulent length scale of the flow was smaller than particle size used as dispersed phase. However, there was no significant change in radial direction water turbulent intensity in comparison with the un-laden flow. It was argued that instantaneous velocity is much lower in radial direction since flow is relatively more intense in stream wise direction for downward flow. Additionally, the turbulence intensity of water at the pipe centre was not impacted by the addition of particles in both the radial and axial direction in upward flow [16].

It is clear that there are several investigations for low concentrated gas-solid flows at low Reynolds number that are available in the literature to investigate turbulence modulation in presence of disperse phase. Additionally, there are only three papers [14, 16, 39] for solid-liquid pipe flows, which are also limited to relatively low  $Re$  and low concentration, but nothing available for higher  $Re$ , higher particle concentration, and larger particle size. This provides motivation to do turbulence modulation investigation in slurry flows at higher particle concentrations and high Reynolds numbers.

## 2.2 Particle image velocimetry

The classification of experimental measurement techniques in two-phase systems is shown in Figure 2.1. Experimental studies in two phase flows are mainly categorized into two groups: sampling methods and online methods [1].

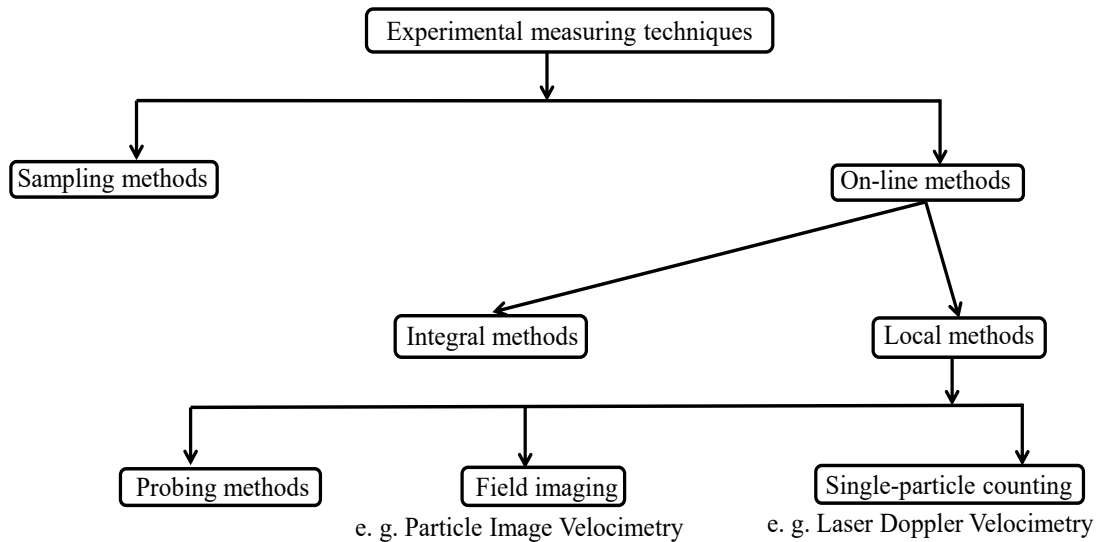


Figure 2.1: Classification of experimental methodologies in two-phase systems [1]

Sampling methods are commonly used to characterize dimensions of particles, equivalent particle diameter, and particle shape factor [1]. In two-phase systems, online methods are used to investigate bulk and local properties of both phases. These techniques are classified into two main groups: integral methods and local methods [1]. Integral methods are non-intrusive in nature and provide bulk properties of two-phase flows. However, local methods allow the investigation of local properties such as mean and fluctuating velocities for both phases and volume fraction of dispersed phase. Local measurement technique may be further categorized into intrusive and non-intrusive methods [1]. Probing methods being invasive in nature disturb the fluid flow. Both field

imaging techniques and single particle counting methods are non-intrusive optical methods. Examples of these techniques are PIV, PTV, and LDV [40].

LDV has been utilized to obtain instantaneous and time-averaged measurements of the velocity [1]. LDV is a single point measurement technique that works on the principle of the Doppler effect. The moving tracer particles, seeded in the flow, scatter the light that is emitted from the laser. This optical technique measures the Doppler shift of the light to measure the velocity of fluid flows [40]. This method has numerous applications in turbulent liquid flows, gas flows, and especially two-phase flows for the measurement of droplet or solid particle velocities [40].

Particle image velocimetry is also an optical measurement method, typically used in experimental fluid mechanics to determine instantaneous velocity of fluid flows [1, 40]. Both PIV and LDV measure the instantaneous velocity of the seeding particles which are scattered by laser light. But most interestingly, PIV allows measurements of the velocity within a plane whereas LDV is a single-point measuring technique. This gives an advantage in using PIV over LDV in practicing quantitative flow measurement and qualitative flow visualization in experimental fluid mechanics [21, 41]. Standard PIV system measures two velocity components on a planar two-dimensional flow field but it has further extended to measure three-dimensional flows by implementing tomographic PIV [40].

For enclosed flows, PIV is performed in a transparent test section that contains a flow having tracer particles. A typical PIV system has components such as a double-pulsed laser to illuminate the area of interest (plane), light sheet forming optics, tracer or seeding particles, single lens camera, and hardware to record PIV images [41, 42]. PIV

measures displacement of seed particles for small time period between two consecutive laser light pulses. It is important for small seeding particles to accurately follow the flow field [40]. Seeding particles should also be uniformly distributed in the flow with proper seeding density. In PIV, a double pulsed laser and laser optics create the thin laser sheet that illuminates the seeding particles in the area of interest. A digital imaging device (such as a CCD camera) records the light scattered by particles onto two image frames [41].

In turbulent dispersed two-phase flows, LDV has been widely used in past decades to perform experimental studies to measure local properties. In particular, most of the experimental investigations on turbulence modulation were performed using LDV. However, these experiments were performed either for dilute or very low concentrated particle laden flow. Recently, PIV has become a promising experimental tool by replacing LDV for many flows, due to the fact that it provides quantitative and instantaneous flow information over an entire plane [4].

The implementation of PIV in dispersed two-phase flows is significantly more challenging than single phase flow. Significant light scattering from particles produces light flare and light bloom or glow into the PIV images. However, PIV has been used in turbulent slurry flows for the relatively low volume fraction of the dispersed phase. For example, Kameyama et al. [16] examined the turbulent flow structure in dispersed slurry pipe flow for 0.6% particle concentration at low Reynolds number. Kiger and Pan [20] examined turbulence modulation in horizontal solid-liquid channel flow for dilute slurry having small particles ( $d = 0.195$  mm) .

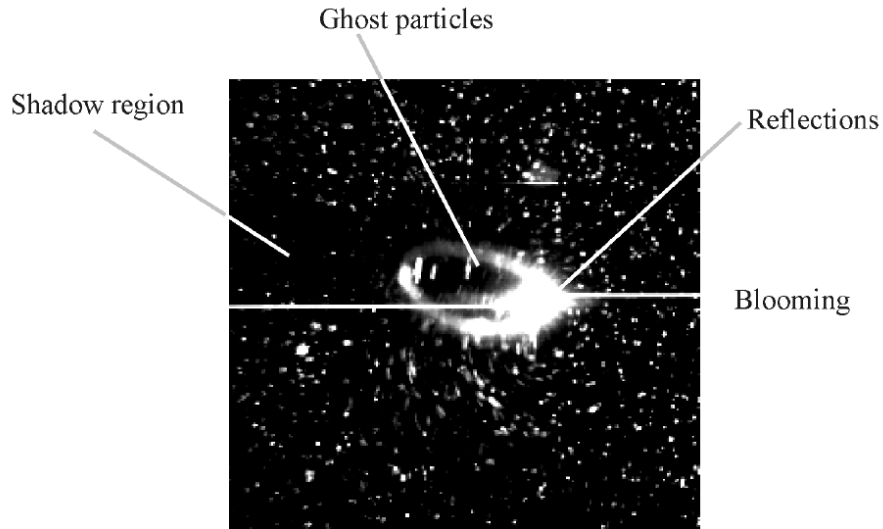


Figure 2.2: Sample PIV image having flow around a rising air bubble in two phase flow [23]

In optical methods, optical transparency is significantly influenced by phase boundaries (interface between two phases) in the flow. Figure 2.2 displays a PIV image of the flow in a laser light sheet around an air bubble rising in quiescent water [23]. Once a bubble comes into the laser sheet, strong reflection and refraction from bubble creates excessive light scattering from bubble. Shadow regions in the light sheet behind the bubble are also noticed. This further leads to lack of illumination of seeding particles in the shadow region. A mirror effect at the air-liquid interface creates ghost particles appearing to be inside the air bubble. The PIV image also shows scattering of light from bubble and blooming effect or excessive light glow. However, PIV is applied in combination with special phase discrimination technique and pre/post-processing methods to eliminate phase boundaries for dilute and low concentrated two phase flows. Some commonly used techniques are fluorescent particles with a dual camera system, particle masking, and correlation peak separation method [23].

Shokri et al. [43] give an example study of a particle-fluid interaction at high Reynolds-number and low particle concentration ( $\phi_v = 0.1 - 0.8 \%$ ) using PIV/PTV techniques in conjunction with a masking technique. They applied gradient based threshold input parameter for edge detection, based on a Hough transform for detection of circular objects. A particular value of threshold was used to detect particles from both frames of the raw images for PIV analysis of the liquid phase. The liquid phase velocity field was calculated by masking out the detected dispersed phase particles in the images. In another study, Bruker [23] did some investigation in bubbly flows using a dual camera system with fluorescent particles technique. He showed that this method could not able to remove bubble contour in two-phase system using filter due to the intense light reflections at the bubble surfaces. This technique only helped in identifies the bubbles but did not improve quality of PIV images.

Light scattering and laser light flare from the disperse phase intensifies with increasing particle concentration. It can also be impossible to penetrate optically due to high opacity of the dispersed phase. In effect, there will not be any available areas for PIV computation which indicates that conventional PIV systems, even in combination with image processing for phase separation, cannot be used for concentrated slurry flows ( $\phi_v > 5-10 \%$ ) since mixtures are challenging to penetrate optically [24]. In conclusion, PIV is quite challenging and difficult to use in the presence of phase boundaries such as solid-liquid interfaces.

### ***2.3 Refractive index matching***

The RIM technique is widely used in combination with optical methods such as PIV and LDV in various flow visualization applications. In RIM, the reflection/refraction problem at solid-liquid interface is eliminated by matching the refractive indices of the solid and liquid phases for flow visualization [44]. This technique improves visual access and reduces image distortion for both illumination and image acquisition during optical measurements. Refractive index matching has become popular method in conjunction with optical diagnostic techniques in particle suspensions, particularly in solid-liquid flows [25].

As an example, liquid and solid axial velocity profiles in concentrated solid-liquid flow loop were measured using LDV and RIM by Wildman et al. [27]. Refractive index slurries were made of 50 % w/w concentrated NaI solution as continuous phase and silica gel particles as dispersed phase, respectively. Averbakh et al. [45] investigated the velocity profiles in concentrated refractive index matched slurries in a rectangular duct using LDV. The RIM slurry was made of PMMA (polymethylmetacrylate) as the dispersed phase and a mixture of Triton X-100, Ucon Oil H-450, and Tetrabromoethane (TBE) as the continuous phase to remove solid-liquid interface [45].

Zachos et al. [46] suggested a RIM solution to remove high degree of light extinction from solids in stirred solid-liquid system during floatation process to measure solid velocity using PIV. The refractive index of glass beads (solid phase) was matched by an organic fluid (tetraline) in the solid-liquid flow. In another study, Nouri et al. [47] investigated particle mean and fluctuating velocities using RIM and LDA methods in a

vertical slurry pipe loop. RIM experiments were performed by organic oil and acrylic particles as continuous and dispersed phase, respectively.

RIM fluids are selected based on various parameters such as fluid refractive index, viscosity, density, toxicity, flammability, reactivity, clearness, transparency and cost for individual applications [26, 48]. Various organic and inorganic index-matched fluids such as zinc iodide, sodium iodide, potassium thiocyanate, alcohols, p-cymene, glycerin, ammonium thiocyanate, and mineral oil are used to achieve optical accessibility for flow visualization [26]. Out of all available index matched fluids, NaI solutions are used often as index-matched fluids in various refractive index matching applications especially in some studies in solid-liquid flows. For example, Chen and Kadambi [9] measured mean and fluctuating velocities of both continuous and dispersed phase in slurry pipe flows. RIM suspensions consisted of silica gel particles and 50 % NaI solution as solid and liquid phase, respectively.

Sodium iodide properties make it a reasonable fluid analog for the study of two-phase systems. For example, Narrow et al. [49] provided an empirical correlation for the NaI refractive index as function of solution temperature, salt concentration, and wavelength for index matching in two-phase systems. Refractive indices of solids and other transparent plastics were matched with predicted refractive index of NaI solution. Anticipated index was based on salt concentrations, calculated using empirical model at particular temperature and wavelength. In another study, Jellison et al. [50] investigated the refractive index of NaI for a wide range of wavelength ( $\lambda = 435\text{-}633\text{ nm}$ ) to understand the effect of wavelength on its index. They showed that refractive index of NaI solution does not change significantly with wavelength. Recently, Bai and Katz [31]

examined NaI refractive index for wide range of concentrations reaching the temperature-dependent solubility limit. They argued that the refractive index has a quadratic dependency on solution concentration. The effect of temperature on NaI's refractive index was also studied. It was noted that the refractive index of NaI was decreased by 0.0008 for 5 °C temperature rise. There is an abundant amount of quantitative study on refractive index of NaI solution to use it as index-matched fluid [31, 49, 50].

Other index matched fluids are also available, one of which is potassium thiocyanate (KSCN). Before selecting an index-matching fluid, properties of NaI and KSCN salt solution were compared and are summarized in Table 2.1.

Table 2.1: Properties of salt solutions , rated on the scale of 0-5, 0 = the lowest level

Fluid	Refractive index	Reactivity	Color	Hazard	cost	Fire
NaI	1.33-1.5	1	Yellowish	2	\$\$	0
KSCN	1.33-1.49	0	Colorless/ Transparent	1	\$	0

It can be noted from Table 2.1 that NaI salt is more expensive than KSCN salt. Additionally, reactivity and hazard scales are higher in NaI than KSCN solutions. It means that NaI solution is more toxic than KSCN solution. Additionally, KSCN solution remains colorless in contrast to solutions of NaI, which become yellowish with exposure to oxygen [31].

However, KSCN solutions do not have any quantitative data about their refractive index in the literature. Despite this lack of information on its refractive index as function

of temperature, concentration and wavelength, KSCN solutions have been used as index-matched fluids in a few applications. Table 2.2 summarizes several instances of the use of KSCN as an index-matched fluid. Table 2.2 explains that most of the research studies do not provide any information about the index of KSCN solution while doing index matching with particular material such as plexiglas and pyrex beads etc..

Table 2.2: An overview of aqueous potassium thiocyanate as index matched fluid

References	KSCN solution	Materials	fluid index ( $n$ )
Jan et. al [51]	Saturated	Plexiglas	---
Gijssen et. al [29]	71% w/w	Plexiglas	---
Harris et. al [52]	65% w/w	Ballotini beads	---
Trifonov et. al [30]	Saturated	Glass and Plastic	---
Anguilar et. al [53]	64% w/w	Pyrex beads	1.4744
Francois et. al [54]	64% w/w	Glass	1.476

Jan et al. [51] studied oscillatory flow in lungs using flow visualization technique in a single bifurcation having lung-type geometry. The bifurcation section was made of transparent Plexiglas that was immersed in the index-matched fluid to avoid optical distortion. Plexiglas refractive index ( $n = 1.49$ ) was matched with saturated aqueous KSCN solution. However, there was no information about the concentration of saturated KSCN solution and its refractive index. In another study, Gijssen et al. [29] conducted velocity measurement and flow visualization in artery bifurcation model using LDA to get quantitative information. The transparent test section was made of Plexiglas having an index  $n = 1.491$ . RIM was performed using concentrated 71 % w/w aqueous KSCN

solution to avoid optical distortion at 36°C. Nevertheless, this study doesn't provide the refractive index of 71 % w/w KSCN solution.

Harris et al. [52] were interested in collecting optical images of the packed glass beads in a fluid inside a three-dimensional micro model using confocal laser scanning microscopy. They implemented RIM technique by matching the indices of glass beads ( $n \sim 1.5$ ) and KSCN salt solution. Aqueous KSCN solution (65% w/w) was used to achieve clear images with an appreciable depth of around 400  $\mu\text{m}$ . They further observed that small variation of 0.01 between the indices of solid and liquid phase had quite a severe impact on image quality. In another study, a method called visible light tomographic reconstruction was developed by Trifonov et al. [30] to recover the shape of transparent objects. The method was based on index matching in which target was contained in roughly same index-matched fluid. Aqueous KSCN solution was used to match the index of transparent objects such as glass and plastic. The concentration of KSCN solution was changed manually while the target was suspended in the solution to achieve index matching. Index matching was observed visually and it was best when refractions from objects against pattern background were minimal.

Collision phenomena in a solid-liquid flow in a liquid-fluidized bed was investigated by Anguilar et al. [53]. Experiments were conducted in a fluidized bed using PTV and RIM. The refractive index of Pyrex was matched with 64 % aqueous KSCN solution. At 20 °C, the index of the Pyrex beads ( $n = 1.474$ ) was the same as the index of Potassium thiocyanate solution ( $n = 1.4744$ ). However, they argued that beads were not totally invisible within the solution due to non-homogenous structure of the beads. In another study, Francois et al. [54] measured a pulsed flow of the velocity field in glass

column. Experiments were performed in a glass (Borosilicate) column using PIV. Optical distortion from the glass was eliminated using 64 % w/w aqueous KSCN solution. There was no information about the refractive index of the glass column, whereas the solution refractive index was 1.476 at 20 °C. It was stated that the refractive index of the KSCN solution was close to the refractive index of glass to have proper index matching. RIM helped them to take recirculation measurements near to wall. It can be further concluded that Anguilar et al. [53] and Francois et al. [54] used 64 % w/w KSCN solution and quoted different refractive index of KSCN at 20 °C with an index difference of 0.0016.

It can be noted from the above mentioned literature that there is no quantitative information available about the refractive index of a KSCN solution varying as salt concentration and solution temperature to perform index matching. The lack of this information and any analysis of the benefits of the KSCN over NaI solutions provide motivation to investigate its properties quantitatively and qualitatively. Such a study of the refractive index of KSCN will help researchers to use it as an index-matched fluid for future studies in a more appropriate manner. Finally, index matched fluid KSCN is also being used in the present study to investigate turbulence modulation in large-scale vertical slurry pipe flows.

## CHAPTER 3: BENCH SCALE REFRACTIVE INDEX MATCHING<sup>1</sup>

This chapter discusses experimental methodologies used to perform bench scale refractive index matching to test fluid and solids. Three different experimental methods are presented: refractometer measurements, reflectance measurements, and refractive index matching performance with a solid and liquid mixture. The results obtained from these methodologies are reported in detail. Finally, properties of the index matched fluid are studied and discussed. The bench scale experiments help in implementing the index matching technique by matching the indices of solid and liquid for turbulence measurement in slurry flow on a large-scale vertical pipe loop.

### *3.1 Experimental Methodologies*

This section explains the experimental methods for bench scale refractive index matching in detail. Firstly, refractometer measurements were conducted to collect a wide range of refractive index data by varying the temperature and concentration of salt solutions. Secondly, reflectance measurements are performed that account for the reflection and refraction from solid objects in solid-liquid flows to obtain unobstructed optical access and minimal image distortion. Lastly, the index matching method is demonstrated with borosilicate beads as the dispersed phase in slurry experiments.

---

<sup>1</sup>Part of this chapter based on:

Agrawal YK, Shokri R, Sanders RS, Nobes DS (2015) Turbulence statistics in solid-liquid flow using a refractive index matching and particle image velocimetry technique. In: 10th Pacific Symposium on Flow Visualization and Image Processing. pp 15–18.

### 3.1.1 Refractometer measurement

Generally, the refractive index of a salt solution depends on three parameters: salt concentration, temperature, and wavelength [49]. The effects of concentration and temperature on refractive index are investigated in detail using refractometer connected with temperature controller.

KSCN and NaI salts are used for the current refractive index matching study. However, the variation of refractive index with wavelength is not considered in this study. When refractive index changes with the wavelength variation, it is called the dispersion effect. Dispersion effects are generally small over the visible light spectrum [44]. For this reason, wavelength effects are not considered for this study.

Aqueous salt solutions were prepared using de-ionized water and salts. Freshly de-ionized water was collected from a water purification system (Elix Advantage, Millipore SAS). The salt concentration ( $c$ ) was measured based on the fraction of salt mass in total mass of aqueous solution. During solution preparation, the solution temperature decreased significantly due to addition of KSCN salts into de-ionized water. This shows that KSCN dissolution was an endothermic reaction. Heat input was provided to keep the solution at room temperature (23 °C) using a hot plate. The temperature of the NaI solution increased while adding NaI salts. It required natural cooling to maintain room temperature as salt dissolution was an exothermic reaction. At 23 °C, the solubility of KSCN solution was estimated. The experimental procedure was the same as the Bai and Katz [31] experiments on NaI solution to measure solubility. Close to the solubility limit, a measured amount of salt (1 g) was added into the solution. Solution was stirred for additional 10 minutes. Following, stirring was stopped for another 10 minutes. If

there was no formation of salt crystals, 1 g extra salt was added into the solution. As long as salt crystals continue to remain invisible, the process of adding extra salt continues. The process was stopped when salt does not reform anymore due to its complete dissolution. During this process, the temperature of solution was kept at 23 °C. The solubility limit of KSCN solution was found to be 70.5 % at 23 °C. The salt solubility depends on solution temperature. However, in this study, the solubility limit was measured at room temperature (23 °C) only. Saturated KSCN solution ( $c = 70.5\%$ ) was prepared and its concentration was varied from 70.5 - 20 % for refractive index measurements. A syringe was used to add a measured amount of de-ionized water to vary the concentration of the salt solution. It was stirred until the solution was well mixed.

Refractive index of the both salt solutions were measured using refractometer (Abbe-3L, Bausch and Lomb). The refractometer was based on a wavelength of 589.3 nm, having an accuracy of  $\pm 0.0001$ . A programmable temperature controller (Polystat, Cole-Parmer) was used to change the temperature of the solution. It was connected with the refractometer to measure the refractive index as the temperature was varied. The refractive index of de-ionized water was measured for a wide range of temperatures to verify the calibration of the refractometer. The refractive index of KSCN salt solution was measured at temperature range of 25 - 40 °C. A wide range of refractive index data was collected by varying the concentration from 70.5 to 20 %. Additionally, aqueous NaI salt solution refractive indices were measured at temperature 23 °C and 25 °C. Indices were compared with KSCN refractive index at same temperatures.

### 3.1.2 Reflectance measurement

Refractometer measurements helped to understand and analyze the refractive index of the KSCN solution with concentration and temperature quantitatively. For refractive index matching, it is important to measure the scattered light from solid objects in different concentration of KSCN solution. The amount of scattered light is important for experimental optical techniques like PIV and LDV, which are used in flow visualization experiments. The reflectance method measures the reflection of light passing through a solid object or Pyrex slide in a rectangular beaker filled with KSCN solution for flow visualization.

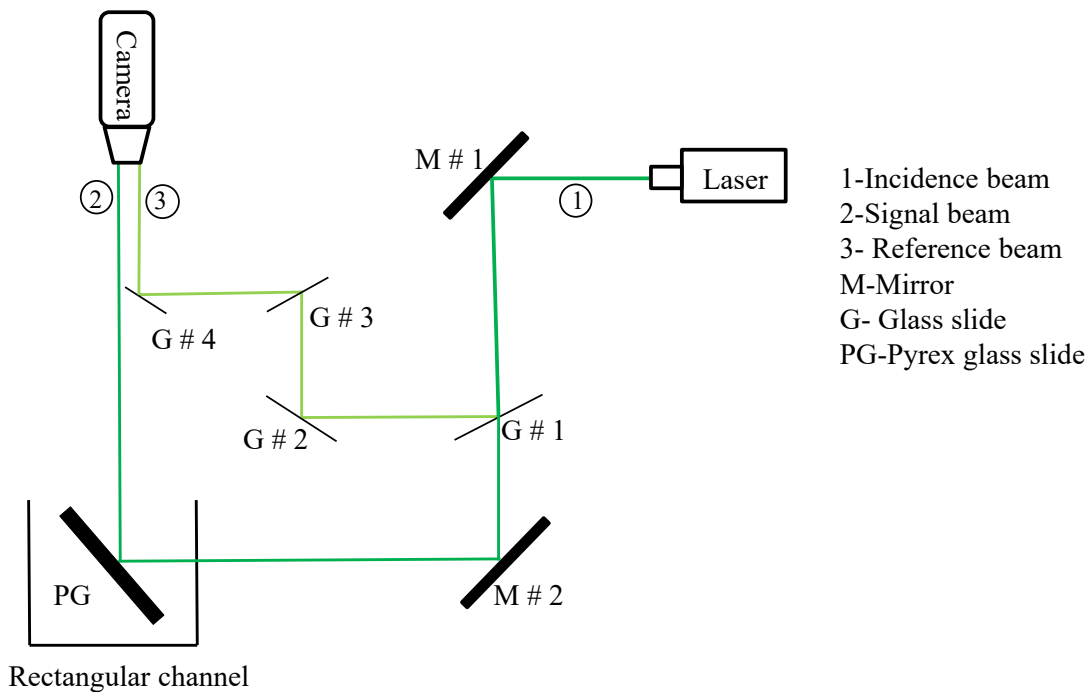


Figure 3.1: Experimental schematic of reflectance method

For reflectance measurement, a laser beam was created using diode-pumped-solid-state laser (LRS-0532-PF Series, LaserGlow technologies). The laser operated in the continuous wave mode with a stated wavelength of 532 nm. Figure 3.1 shows the

incident laser beam reflected from mirror M # 1 and hitting glass slide G # 1. Mirror M # 1 was orientated at a  $45^\circ$  angle to strike the reflected light on glass slide G # 1 perpendicularly. The laser beam from glass slide G # 1 reflected from glass slides G # 2, G # 3, and G # 4, respectively. All glass slides were orientated at angle of  $45^\circ$ . The final reflected beam from glass slide G # 4 is called the reference beam. The mirror M # 2 that was orientated at  $45^\circ$  angle redirected the transmitted beam from glass slide G # 1. Experimental apparatus for reflectance measurement to perform refractive index tuning is shown in Figure 3.1.

The reflected light beam from M # 2 intersected with Pyrex glass slide (PG). The vertical support was used to hang the Pyrex slide at  $45^\circ$  orientation within the rectangular beaker. The acrylic-made transparent beaker had dimensions of  $6.5 \times 6.5 \times 7 \text{ cm}^3$ . The reflected light beam from Pyrex slide was perpendicular to incidence beam. It is called signal beam. An 8-bit camera (TMC-4200 GE, JAI Company) was installed to capture the reference and signal beams. Reference and signal beam images had a resolution of  $2048 \times 2048$ . Both beams are labeled in Figure 3.1. Four glass slides were used to decrease the intensity of reference signal. This helped to avoid saturation limit of camera. The intensity of the reference beam was always constant. The signal beam intensity varied with the concentration of the KSCN solution in the transparent rectangular channel. The signal and reference intensities were measured for the concentration range 0 - 70 % at a temperature of  $23^\circ\text{C}$ .

### **3.1.3 Refractive index matching in a solid–liquid mixture**

The refractometer measurements provide quantitative analysis of the refractive index of KSCN. Reflectance measurements account for scattering of the light from a solid object. Both methods do not consider optical analysis for index matching with the Borosilicate beads typically used as the dispersed phase in slurry experiments. For this purpose, a transparent rectangular beaker having 6.5 cm in the depth was used. It was approximately half filled with the 3 mm size beads in a packed bed. The remaining half of the beaker was filled with  $c = 70\%$  w/w concentrated KSCN solution. In addition, a calibration target was used as an image reference. It was positioned in the middle plane of the beaker. The calibration target had equally spaced white dots of same diameter in a black background. A  $2048 \times 2048$  pixel camera (TM-4200GE, JAI) was installed to capture the calibration target images as the KSCN concentration was varied in the beaker. There were at least 22 solid-fluid interfaces to cross to see through the calibration target that were counted manually during the experiments.

## ***3.2 Results and Discussions***

This section reports results obtained from the experimental methodologies discussed in Section 3.1. The refractive index of aqueous KSCN solution is measured for a broad range of solution temperature and salt concentration using a refractometer device connected to temperature controller. Refractive index of KSCN solution is expressed by an empirical model with salt concentration and solution temperature. In the reflectance measurements, variations in the signal-to-reference intensity ratio are reported as function of solution refractive index. Finally, calibration target images obtained at

different concentration of KSCN solution in a 3 mm pack glass beads are explained in detail.

### 3.2.1 Refractive index results

To gain confidence in the refractometer calibration, the refractive index of water was measured and compared with available index data in the literature at different temperatures and a fixed wavelength ( $\lambda$ ) of 589.3 nm. Table 3.1 compares the refractive index of water measured presently with the available index in literature at temperatures  $T = 20, 30$  and  $40$  °C. It is clear from Table 3.1 that present measurements are close to indices reported in the literature. It signifies that refractometer system is being calibrated perfectly.

Table 3.1: Refractive index of water at different temperatures

Temperature (°C)	Past measured index [55]	Present measured index
20	1.33326	1.3333
30	1.3323	1.3321
40	1.33095	1.33085

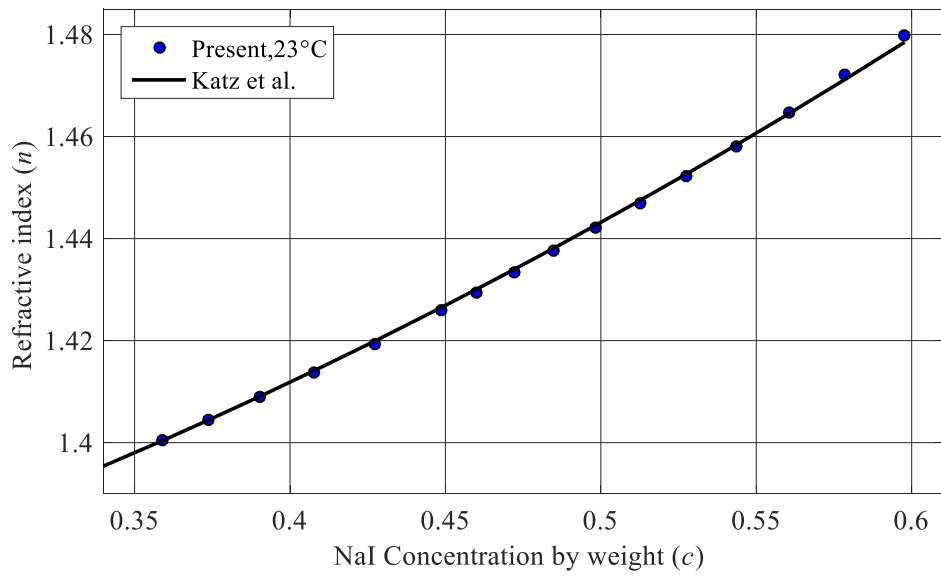
Sodium iodide solution is a common index matched solution used in flow visualization studies [31]. The refractive index of aqueous NaI solution was measured and compared with previously published results [31, 49] to validate the experimental methodologies for the refractometer measurements used currently. The refractive index of NaI solution was measured for wide range of concentrations at a temperature of  $T = 23$  °C and wavelength  $\lambda = 589.3$  nm by Bai and Katz [31]. A concentration based

refractive index correlation at temperature 23 °C and wavelength 589.3 nm is shown in Equation (3.1). It illustrates that index has quadratic dependency on concentration.

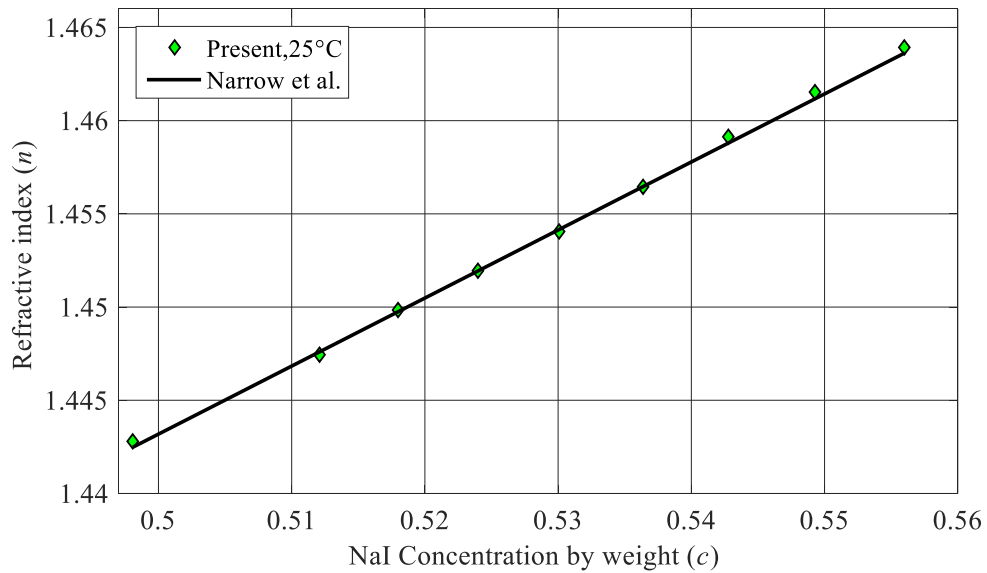
$$n_{\text{NaI}} = 0.2425 c^2 + 0.09511 c + 1.335 \quad (3.1)$$

In another study, Narrow et al. [49] did measurements of the refractive index of NaI solution for a smaller concentration range  $c = 55 - 58.5 \%$  than Bai and Katz [31] work. However, the refractive index in that study was measured for wide range of temperatures  $T = 20 - 35 \text{ }^\circ\text{C}$ , and different wavelengths  $\lambda = 589.3 \text{ nm}$  and  $632.8 \text{ nm}$  [49]. Equation (3.2) describes an empirical model based on their measurements:

$$n_{\text{NaI}} = 1.252 - (2.91 \times 10^{-4} c^{-1})T + (0.365)c + (5542) * \lambda^{-2} \quad (3.2)$$



(a)



(b)

Figure 3.2: Refractive indices of sodium iodide solutions (a) Present and Bai and Katz [31] measurements at 23°C (b) present and Narrow et al. [49] studies at 25 °C

Figure 3.2 shows the refractive index of NaI solution for present studies in comparison to past publication models. Refractive index measurements of NaI are

compared in Figure 3.2(a) at  $T = 23^\circ\text{C}$  and  $\lambda = 589.3 \text{ nm}$  for present and [31]. It shows that the present measurements fall on Bai and Katz's [31] index correlation for the concentration range (35 - 60 %) tested here. Figure 3.2(b) shows the refractive index of NaI solution for the present and Narrow et al. [49] measurement for a concentration range of 55 - 58.5 %. Results are compared by keeping the constant temperature and wavelength to  $T = 25^\circ\text{C}$  and  $\lambda = 589.3 \text{ nm}$ , respectively. It is evident that index of NaI solution varies with concentration in linear manner for the tested concentration range. The present measurements and Narrow et al.'s [49] correlation data coincide with each other. The results of NaI refractive index are entirely matched with past published empirical model. It gives assurance in the present experimental methodology.

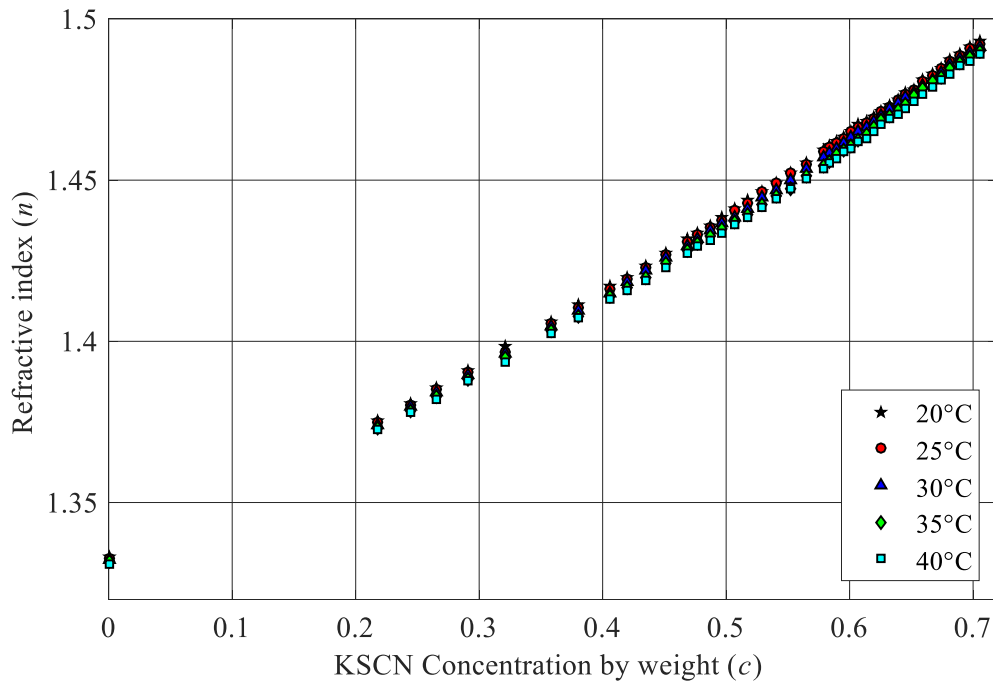


Figure 3.3: KSCN solution refractive index varying with salt concentration and solution temperature

The refractive index of KSCN solution as function of the salt concentration and solution temperature is shown in Figure 3.3. Results of refractive index measurements at temperature  $T = 20, 25, 30, 35, 40$  °C are presented for wide concentration range 0 - 70.5 %. The refractive index of KSCN solution increases continuously with concentration. Refractive index rises in a nonlinear fashion for all solution temperatures tested here. A wide range of refractive indices is achieved with change in concentration and temperature. The range starts from the index of water,  $n = 1.3308$  and ends with refractive index of saturated KSCN solution,  $n = 1.4931$ . Results further depict that there is decrease in refractive index with increase in solution temperature for the temperature ranges tested here. It was noticed that there was a decline of 0.004 in the average refractive index over the concentration range for 20 °C rise in temperature.

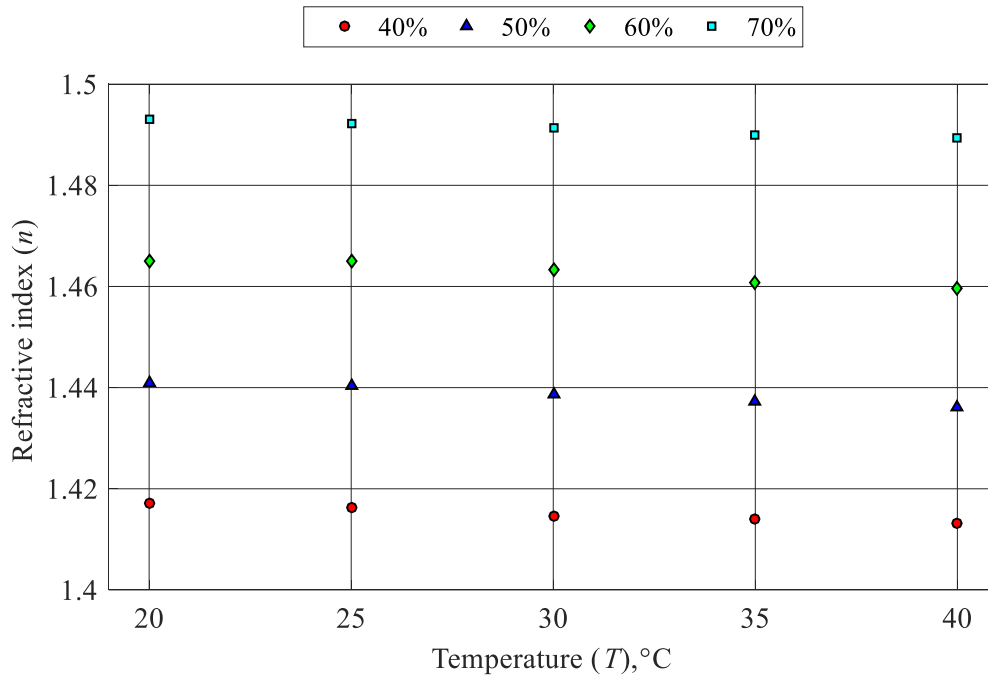


Figure 3.4: Refractive index of KSCN solution as a function of temperature of the solution and salt concentration levels

The variation in the KSCN solution refractive index by changing the solution temperature are displayed in Figure 3.4 for salt concentration levels  $c = 40, 50, 60$  and  $70\%$ . Results show that index decreases linearly with increase in solution temperature. Also, refractive index does not decline significantly with the rise in solution temperature for the temperature ranges tested here. For example, the indices are 1.4410, 1.4405, 1.4385, 1.4372, and 1.4362 at temperature of 20, 25, 30, 35, and 40 °C respectively for salt concentration  $c = 50\%$ .

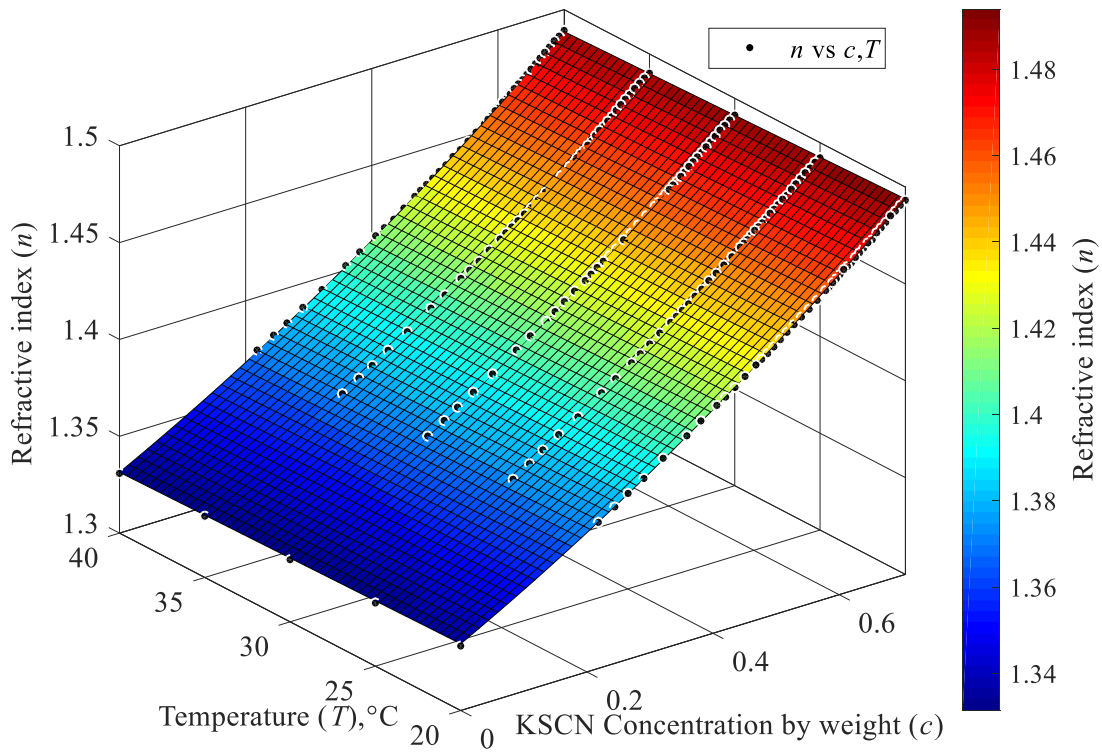


Figure 3.5: Surface plot to show variation in refractive index of KSCN solution with different temperatures and salt concentrations

To see the combined effect of temperature and concentration at the wavelength of 589.3 nm, the refractive index of KSCN solution is illustrated by Figure 3.5. The surface

plot presents that the refractive index of KSCN solution has a nonlinear dependency on concentration and linear dependency on temperature. The refractive index color map is on a scale of 1.3308 - 1.4931 to visualize the wide range of indices. This surface plot describes the surface created by empirical model defined in Equation (3.3) along with experimental data points on the surface.

Indices of KSCN solution as function of concentration and temperature were fitted in a polynomial fit (linear in  $T$  and quadratic in  $c$ ). The data fitted well with  $R^2 = 0.997$  and resulted in the following empirical model:

$$n_{\text{KSCN}} = 0.0774 c^2 - 0.00015 T(c + 1) + 0.1745 c + 1.338 \quad (3.3)$$

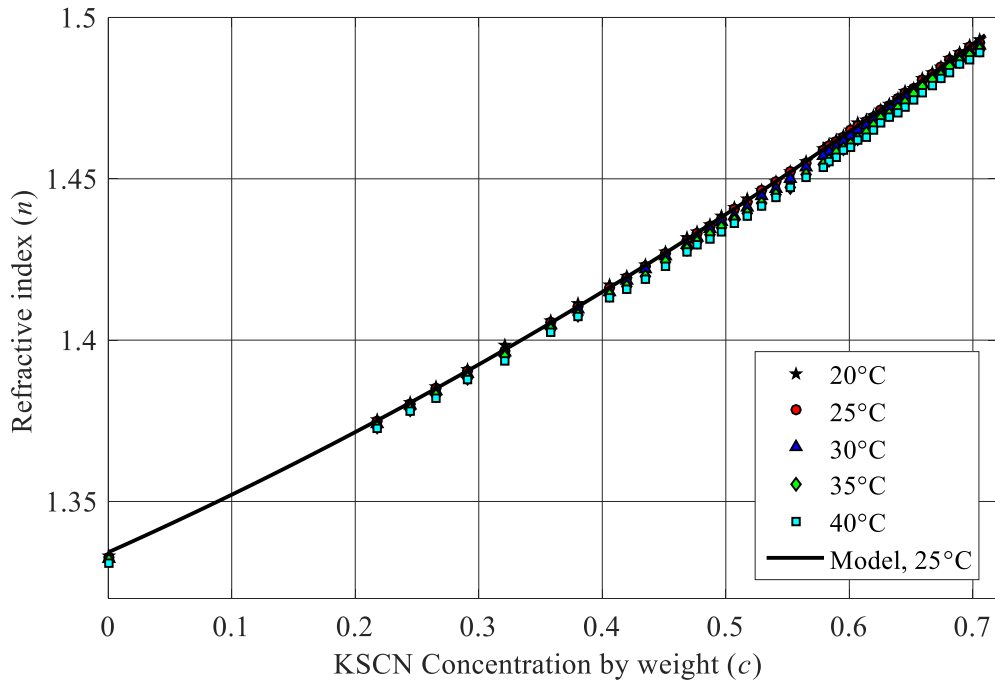


Figure 3.6: KSCN solution refractive index on empirical model at 25 °C

Figure 3.6 shows experimental measured KSCN refractive index by varying solution concentration at different temperatures and empirical model predictions defined

in Equation (3.3) at 25 °C. It is evident that experimental data of index at 25°C coincides with empirical model presented here.

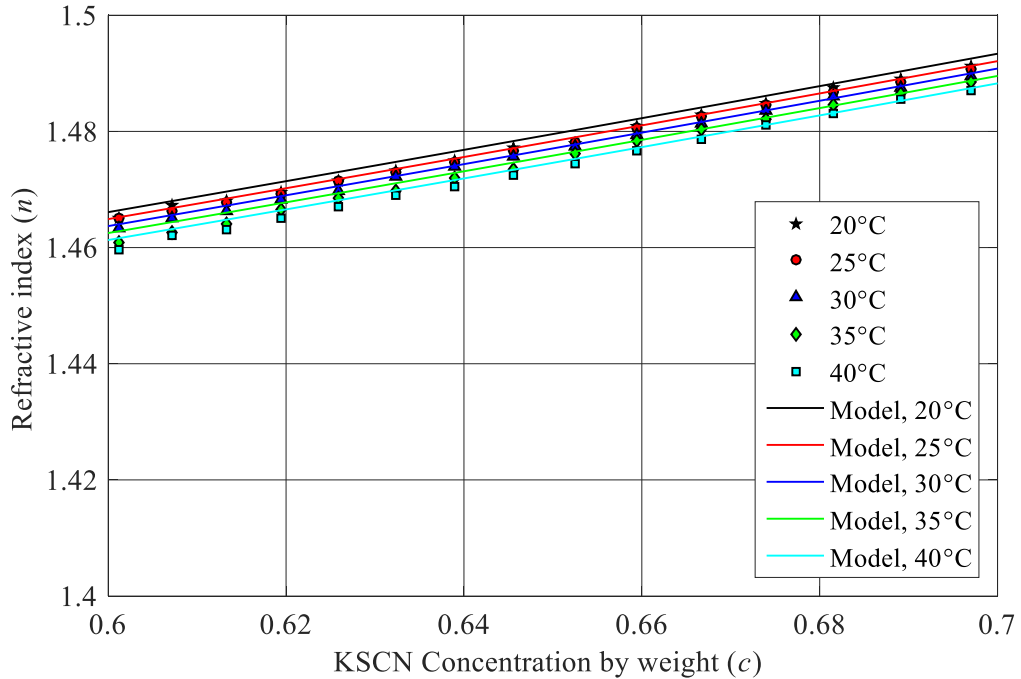


Figure 3.7: KSCN refractive index experimental data on fitted empirical model for concentration range 60 - 70 %

Figure 3.7 displays experimental data and model predictions from Equation (3.3) for narrow concentration range 60 - 70 % for temperature range 25 - 40° C. It is evident from Figure 3.7 that model predicted refractive index matches with experimental measured refractive index for a wide temperature range.

The present empirical model on the KSCN solution refractive index indicates that index is decreased by 0.004 with increase in 20 °C temperature rise at wavelength of 589.3 nm. Similarly, past publications suggest that there is drop of around 0.004 in refractive index of NaI solution with increase in temperature from 20 to 40 °C at wavelength of 589 nm [31]. In conclusion, temperature sensitivity for both solutions is

similar. Given this low sensitivity to temperature, it motivates to mainly focus on concentration sensitivity analysis of both salt solutions. The concentration gradient of NaI and KSCN solution was calculated for the entire concentration range at  $T=23\text{ }^{\circ}\text{C}$  using Equations (3.1) and (3.3) respectively. Equations (3.4) and (3.5) show the concentration gradient for NaI and KSCN solutions refractive index:

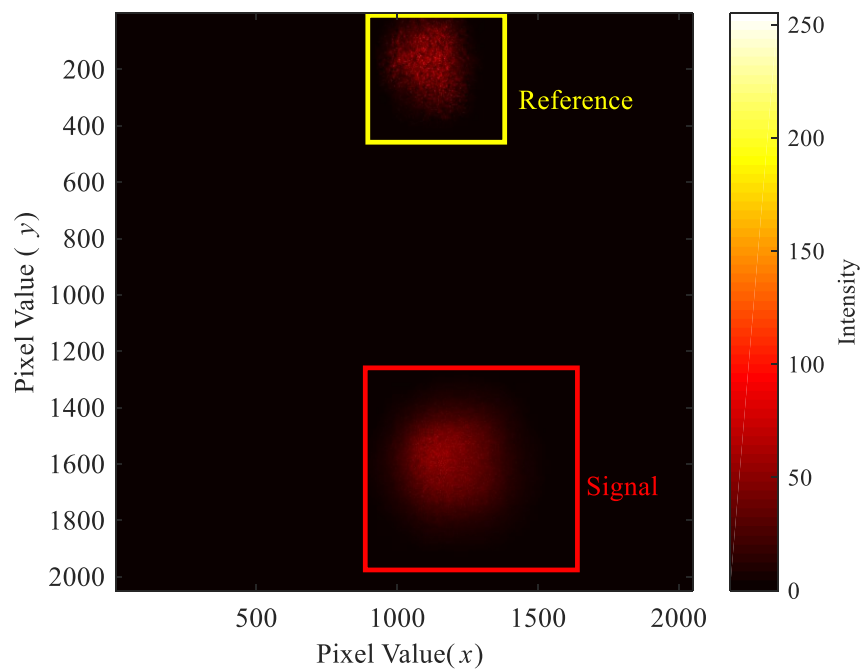
$$\frac{dn_{\text{NaI}}}{dc} = 0.485c + 0.095 \quad (3.4)$$

$$\frac{dn_{\text{KSCN}}}{dc} = 0.155c + 0.179 \quad (3.5)$$

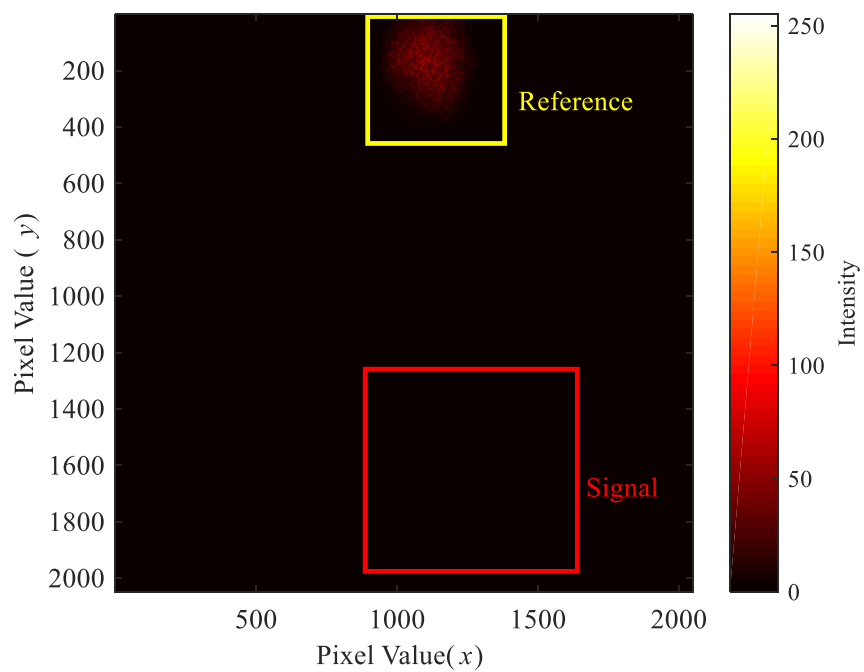
The slopes are 0.485 and 0.155 from concentration gradient equations for NaI and KSCN solution, respectively. The slope for NaI is three times higher than for KSCN. It suggests that index of NaI increases more rapidly than KSCN when concentration is changed. It gives an interesting result that KSCN is a much better index-matched fluid than NaI because the sensitivity of KSCN solution refractive index is much lower to concentration changes than NaI solution. Additionally, this also implies that index matching with KSCN will be easier to establish and maintain within an experiment.

### **3.2.2 Discussion on reflectance measurement**

The signal-to-reference intensity ratio was calculated for the concentration range 0 - 70% at a temperature of  $23\text{ }^{\circ}\text{C}$  using reflectance measurements. During measurements, the reference beam intensity was fixed. The reference beam helps to take account for any small fluctuations in the laser power. Intensity of the signal beam intensity varied by changing the KSCN salt concentration.



(a)



(b)

Figure 3.8: Signal and reference beam intensity in pixel space at (a) 10% (b) 60% concentrated KSCN solution

Figure 3.8(a) shows the reference and signal beam intensity images for 10 % KSCN concentrations whereas the reference and signal beam images for 60 % KSCN are displayed in Figure 3.8(b). Both beams' intensities are illustrated on the color map of scale 0 - 255. The reference beam does not pass through the KSCN solution so the reference beam intensity does not change with KSCN concentration. Reference intensity is always fixed for presently used laser wavelength of 532 nm. However, the signal beam which reflects from a Pyrex slide in a rectangular beaker is in direct interaction with the KSCN solution. When KSCN concentration is increased from 0 to 70 % range in a sequential rise of 10 % concentration, a change in signal beam intensity is noticed. Signal intensity drops significantly with the rise in KSCN concentrations. Finally, signal intensity reaches zero or a point where it is on the order of camera and system noise. This occurs due to the refractive index of Pyrex slides being constant for a particular wavelength and temperature. However, the refractive index of KSCN increases with concentration in a quadratic fashion, as demonstrated by the empirical model Equation (3.3). It is evident from Figure 3.8 that the signal beam intensity is much higher and brighter in 10 % than 60 % KSCN concentration. Furthermore, the reference intensity appears similar for both KSCN solutions. Minimal light scattering and flaring from solid object is noticed for 60 % KSCN solution in contrast to 10 % KSCN solution, as illustrated in Figure 3.8 for index matching.

To analyze the reflection from Pyrex slide, the signal-to-reference intensity ratio ( $S/S_R$ ) was calculated for the complete concentration range (0 – 70 %). Figure 3.8 shows effective pixel space selected for the signal and reference beams. It is outlined in red and yellow rectangular area for the signal and reference beams, respectively. Effective pixel

space was selected for images collected at different KSCN concentration. The mean value of intensity was determined by averaging over this area. Mean value of signal intensity changed with solution concentration. In other words, signal intensity varied with different refractive index of KSCN solution whereas reference intensity was approximately same for all concentration range.

In the present study, the amount of light that reflects from the solid Pyrex slide varies when the index of KSCN solution is changed due to its concentration variation at 23 °C. In classical optics, the Fresnel equations are used to explain the reflection phenomenon [56]. The Fresnel equations predict the amount of light that reflects between media of different refractive indices. These equations are applied to any linear, isotropic and homogenous media [56]. Incident light can be polarized or un-polarized in nature when it interacts at the interface between two medium. Polarized incidence light can be divided into two categories: *s*-polarized light and *p*-polarized light [56]. For *s*-polarized light, electric field and plane of incidence are mutually orthogonal. Whereas, for *p*-polarized light, electric field and incidence plane are mutually parallel.

Reflectance or reflectivity ( $R_x$ ) is defined as a fraction of incident intensity that is reflected. Fundamentally, it is the ratio between reflected light power and incidence light power. Reflectance of light from one medium to other medium having different refractive indices in *s*-polarized light and *p*-polarized light is given by, respectively [56]:

$$R_s = \left| \frac{n_1 \cos \theta_i - n_2 \cos \theta_t}{n_1 \cos \theta_i + n_2 \cos \theta_t} \right|^2 \quad (3.6)$$

$$R_p = \left| \frac{n_1 \cos \theta_t - n_2 \cos \theta_i}{n_1 \cos \theta_t + n_2 \cos \theta_i} \right|^2 \quad (3.7)$$

Here,  $\theta_i$  is the angle of incidence beam and  $\theta_t$  is angle of refracted beam measured from the normal of the interface between two mediums. Refractive index of the first and second medium is  $n_1$  and  $n_2$ , respectively. It is assumed in the above equations (3.6) and (3.7) that permeability of both mediums is same. The relationship between the angle of incidence and refractive angle is given by Snell's law [56]:

$$n_1 \sin \theta_i = n_2 \sin \theta_t \quad (3.8)$$

The  $s$  and  $p$  polarized reflectance,  $R_s$  and  $R_p$ , can be expressed in term of angle of incidence and refractive indices of media by combining Equations (3.6), (3.7), and (3.8):

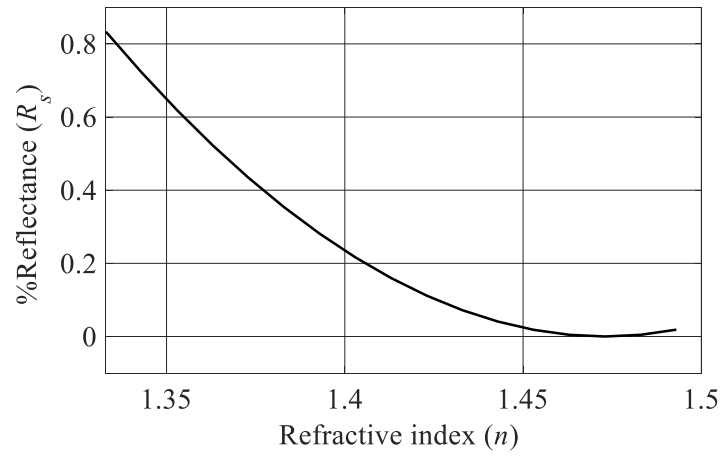
$$R_s = \left| \frac{n_1 \cos \theta_i - n_2 \sqrt{1 - \left(\frac{n_1}{n_2} \sin \theta_i\right)^2}}{n_1 \cos \theta_i + n_2 \sqrt{1 - \left(\frac{n_1}{n_2} \sin \theta_i\right)^2}} \right|^2 \quad (3.9)$$

$$R_p = \left| \frac{n_1 \sqrt{1 - \left(\frac{n_1}{n_2} \sin \theta_i\right)^2} - n_2 \cos \theta_i}{n_1 \sqrt{1 - \left(\frac{n_1}{n_2} \sin \theta_i\right)^2} + n_2 \cos \theta_i} \right|^2 \quad (3.10)$$

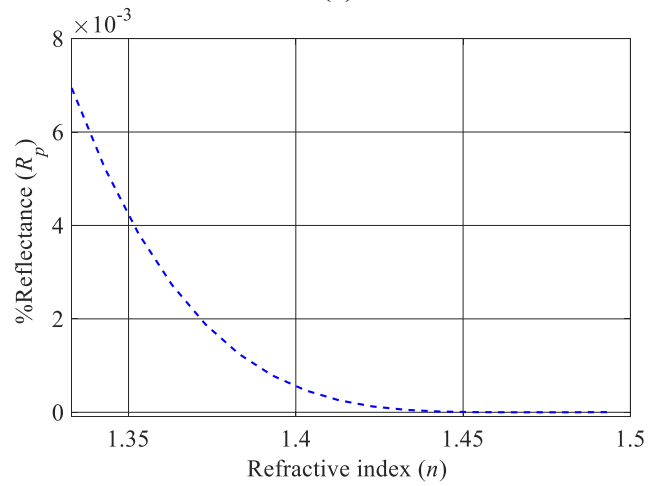
In the present reflectance measurements, angle of incidence  $\theta_i$  is  $45^\circ$ . Reflectance from unpolarized light is described as the average between the two signals by following [56]:

$$R_u = \frac{R_s + R_p}{2} \quad (3.11)$$

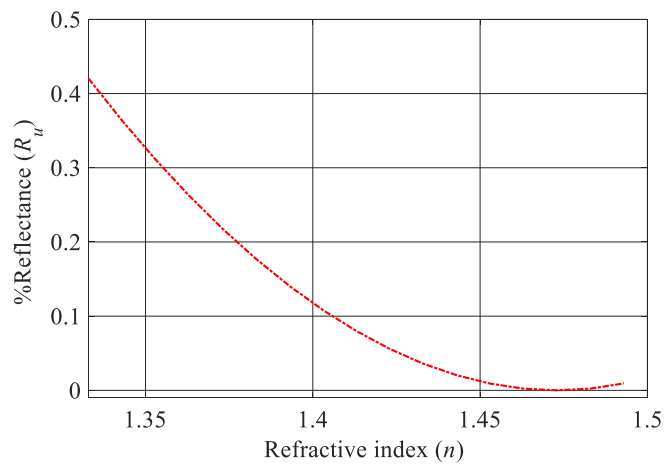
where  $R_s$ ,  $R_p$ , and  $R_u$  are reflectance from  $s$ -polarized light,  $p$ -polarized light, and unpolarized light respectively.



(a)



(b)



(c)

Figure 3.9: Percent reflectance for (a)  $s$ -polarized (b)  $p$ -polarized (c) un-polarized light from solid Pyrex slide in different refractive index of KSCN solution based on Fresnel equations

Figure 3.9 displays percent reflection from a solid Pyrex slide in different refractive index (concentrations) of KSCN solutions from Fresnel equations described in (3.9), (3.10), and (3.11) at  $45^\circ$  angle of incidence. Percent reflectivity for *s*-polarized, *p*-polarized and un-polarized light is displayed in Figure 3.9 (a), (b), and (c), respectively. By varying the KSCN salt concentration, refractive index of KSCN solution is changed. It is clear from Figure 3.9 that reflectance of *s*-polarized light, *p*-polarized light, and un-polarized light decreases as refractive index is increased. At the point of perfect refractive index ( $n_{pyrex} = 1.473$ ), reflectance is zero. Figure 3.9 (a), (c) shows that further increase in refractive index of KSCN solution leads to rise in reflectivity for *s*-polarized and un-polarized light from Pyrex slide. However, reflectance from *p*-polarized light is constant when KSCN index is increased further after reaching the point of perfect refractive index matching, as depicted in Figure 3.9 (b). The maximum reflectivity for *s*-polarized light from Pyrex slide is 0.83 % at KSCN refractive index of 1.3333 (0% KSCN, pure water) and goes to zero at refractive index of 1.4730 same as refractive index of Pyrex slide. Reflectivity from *p*-polarized light is negligible compared to the component of *s*-polarized as shown Figure 3.9(b). For example, maximum reflectivity is 0.007 % at refractive index of 1.3333. Figure 3.9 also shows a non-linear variation of reflectivity with change in refractive index of KSCN solution for all three types of polarized light. Reflectance from un-polarized light is based on average reflectivity calculated from *s* and *p*-polarized light as shown in Figure 3.9.

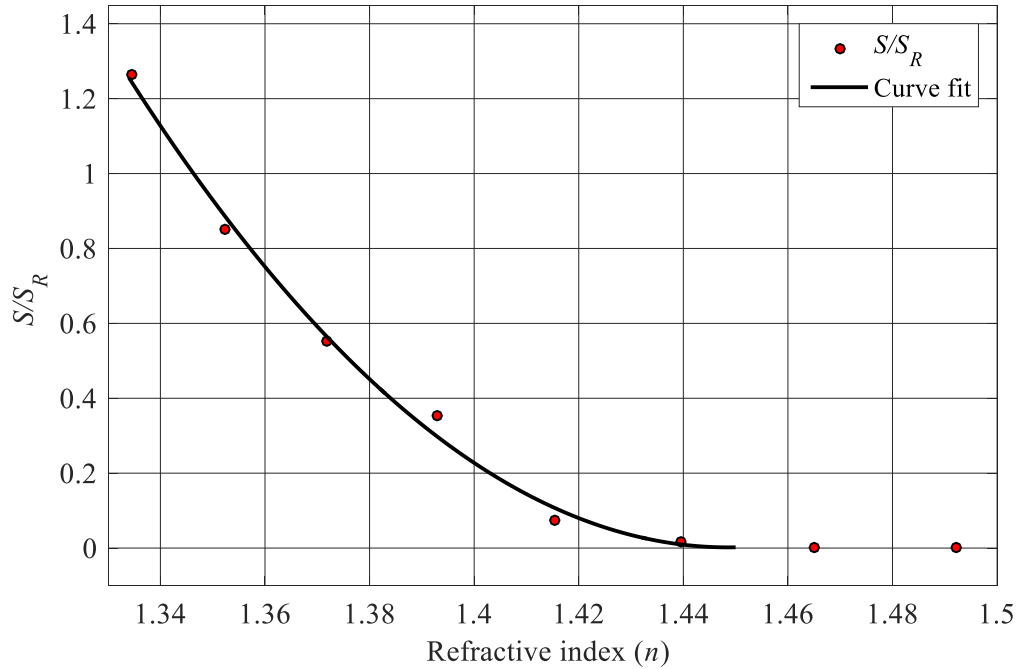


Figure 3.10: Signal to reference intensity ratio versus KSCN refractive index at 23° C

As discussed earlier, the signal to reference intensity ratio was determined for a wide range of concentration (0 - 70 %). Refractive index of KSCN was calculated from the empirical model described in Equation (3.3) for 0-70 % KSCN concentration at  $T=23^{\circ}\text{C}$ . The variation in  $S/S_R$  ratio over the wide range of refractive index is demonstrated in Figure 3.10 at a temperature 23 °C. Results suggest that when the refractive index increases, there is a significant drop in refraction and reflection from the Pyrex slide. It is observed that the  $S/S_R$  ratio declines sharply in refractive index range 1.33-1.44. Finally, signal intensity goes towards zero for further increase in refractive index. It is due to fact that intensity in this range is smaller than the camera and system noise itself.

The experimental results of  $S/S_R$  ratio obtained at a fixed temperature are fitted with a second order polynomial fit of refractive index. Signal to reference ratio is approximately zero in the refractive index range (1.44-1.49) which corresponds to concentration range 50 - 70%. This refractive index range is not considered in the curve fit. The data fit well with  $R^2 = 0.995$  and the fit give the following empirical relation:

$$\frac{S}{S_R} = 95.415n^2 - 276.44n + 200.23 \quad (3.12)$$

Non-linear and second order polynomial variation in  $S/S_R$  shows similar behavior seen in reflectance curve from all three types of polarized light as described by the Fresnel equations. Present reflectance measurements do not provide exact quantitative data of reflectance as shown in Figure 3.9 due to following:

- The present study measures  $S/S_R$  ratio whereas Fresnel equation predicts reflection from a single interface between two different refractive indices. There are multiple glass slides in present configuration that leads to multiple reflection and refraction from different interfaces;
- Current measurements do not take into account the polarization state of the light. It could be  $s$  or  $p$  or a mixture of  $s$  and  $p$  polarization;
- Signal to reference intensity ratio is  $\sim$  zero in the range of 50 - 70 % KSCN concentration due to camera configuration, the low signal measured on the camera and system noise itself.

### **3.2.3 Results on index matching for solid-liquid interfaces**

This section demonstrates the effectiveness of refractive index matching with a KSCN solution and borosilicate glass beads. Borosilicate beads were to be used as the disperse phase in large scale vertical pipe loop for refractive index matching suspensions, so it was necessary to verify that KSCN provided suitable index matching. Firstly, calibration target images are shown when KSCN concentration is changed in the packed bed beads of a transparent rectangular beaker of beads. Secondly, the concentration sensitivity for NaI and KSCN salt solutions is investigated for a narrow concentration range  $c = 54 - 66\%$  as it overlaps with the refractive index of borosilicate glass. Lastly, temperature gradient analysis is reported for refractive index matched fluid for wide range of temperature.

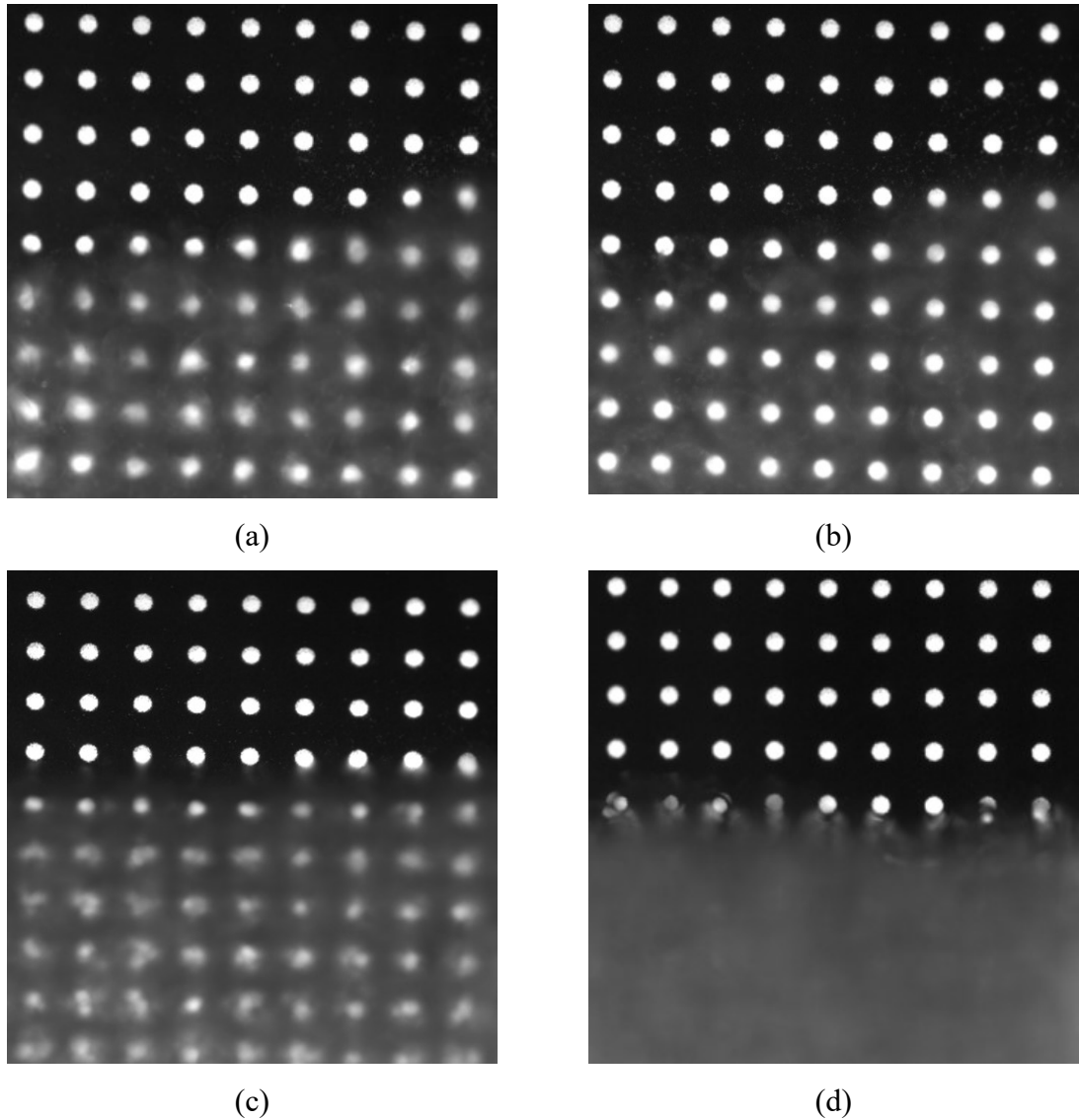


Figure 3.11: Calibration target in packed bed beads for KSCN concentration (a) 60.8% (b) 62.4 (c) 64.3 (d) 68.2 w/w

Figure 3.11 shows calibration target images with visible calibration dots in the packed bed for  $c = 60.8, 62.4, 64.3,$  and  $68.2\%$  respectively. There is an observed distortion in the images of the target dots for  $c = 60.8\%$  as shown in Figure 3.11(a). When concentration is further increased, target dots begin to show more clearly. This is due to the fact that KSCN concentration draws the refractive index of the liquid and solid together allowing undistorted images of the target dots to appear. It is suggested in the

literature that solid objects should be invisible and that the background target behind the objects should be undistorted for the perfect refractive index matching [31]. At  $c = 62.4\%$  dots are most clearly visible. It means that little light is refracted by the beads and this is the point of perfect index matching. However, further increasing the concentration creates a mismatch in refractive index that is observed by distortion in the bottom half image of the target dots as shown for  $c = 64.3\%$  in Figure 3.11(c). With a further increase in KSCN concentration, the bottom half of the target is completely invisible as illustrated in Figure 3.11(d) for  $68.2\%$  concentration. Light is dispersed and scattered due to the presence of solid beads.

It is explained in section 3.2.1 that the temperature sensitivity for both NaI and KSCN solutions is quite similar. Additionally, the concentration sensitivity for NaI solution is three times higher than KSCN solution. Concentration range  $c = 54 - 66\%$  was chosen for sensitivity analysis for both the fluids, as it overlaps with the refractive index of borosilicate glass. Borosilicate beads have a documented value of  $n = 1.473$  [57].

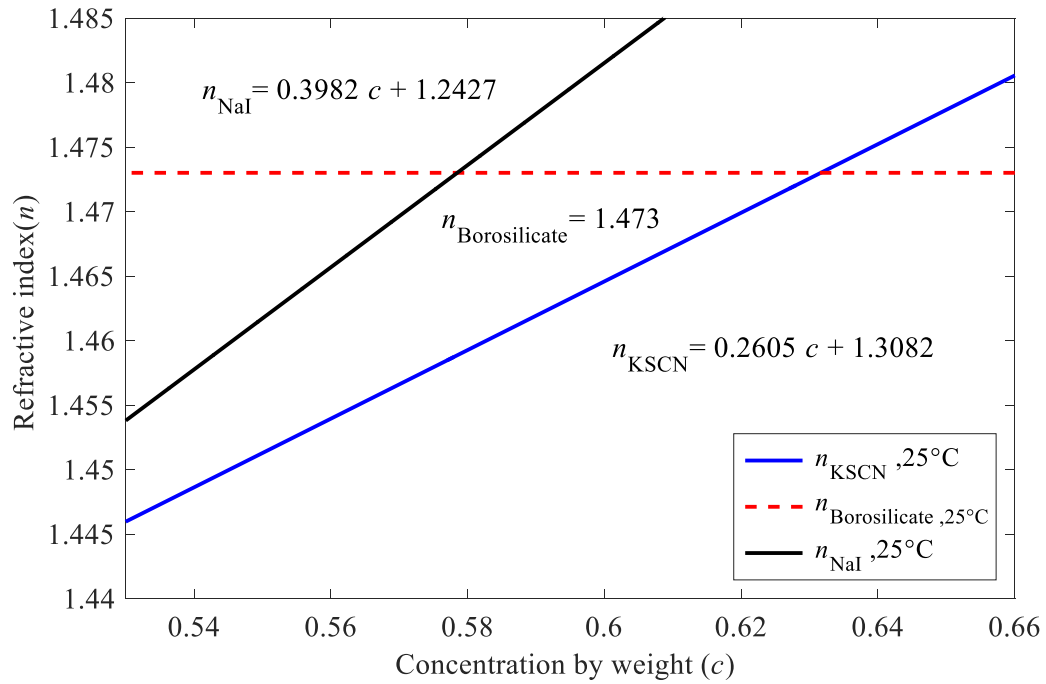


Figure 3.12: Gradient of KSCN and NaI solution for concentration sensitivity

Figure 3.12 shows the variation in refractive index of KSCN and NaI solution for 54 - 66 % concentration range. The refractive index results are fitted in a linear, least-squares fit for aqueous NaI and KSCN which gives:

$$n_{\text{NaI}} = 0.3982 c + 1.2427 \quad \rightarrow \quad \frac{dn_{\text{NaI}}}{dc} = 0.3982 \quad (3.13)$$

$$n_{\text{KSCN}} = 0.2605 c + 1.3082 \quad \rightarrow \quad \frac{dn_{\text{KSCN}}}{dc} = 0.2605 \quad (3.14)$$

The experimental index data of KSCN and NaI solution for 54 - 66 % concentration range shown in Figure 3.12 fits well with the empirical correlation shown in Equations (3.13) and (3.14) having  $R^2 = 0.9994$  and  $0.9992$  for KSCN and NaI, respectively. The concentration gradient for NaI and KSCN index is 0.3982 and 0.2605 respectively as mentioned in Equations (3.13) and (3.14). In other words, the gradient for

the NaI solution is 1.53 times greater than concentration gradient for the KSCN solution. This indicates that the refractive index of KSCN is much less sensitive with concentration changes than NaI as an index matched fluid for refractive index matching (RIM). It further indicates that it will be easier to establish and maintain index matching within an experiment at vertical pipe loop operations.

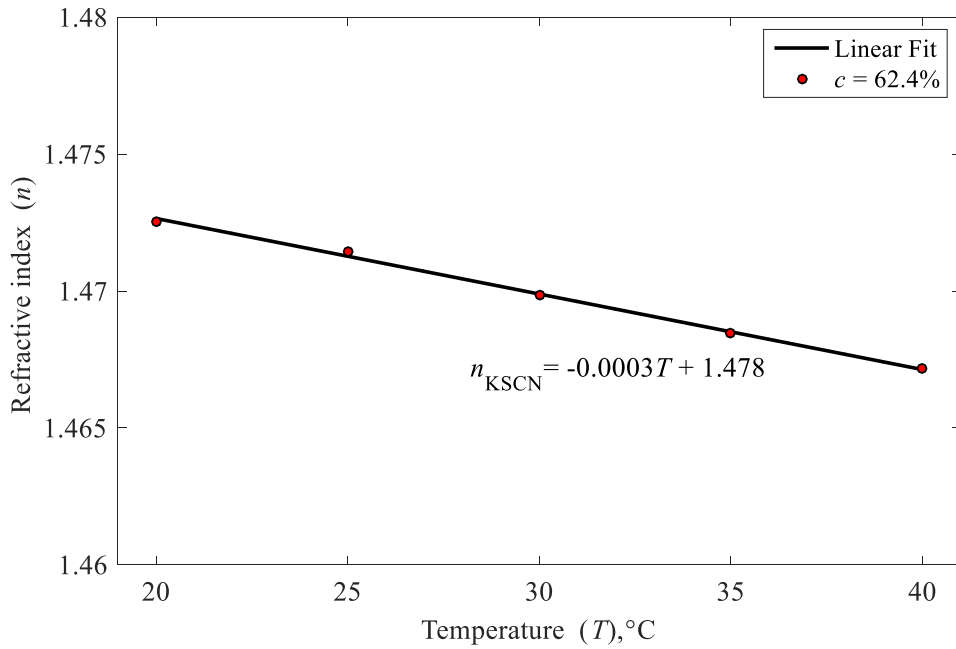


Figure 3.13: Refractive index matched KSCN solution for temperature sensitivity

Figure 3.13 shows variation in refractive index of KSCN at different temperatures for matched refractive matched point ( $c = 62.4\%$ ) with linear fitted model. Results are plotted for refractive index with the wide range of temperature 20 - 40 °C. It depicts that temperature gradient for the index is 0.0003 with temperature variation. Temperature does not play a significant role in refractive index matching with Borosilicate beads for vertical loop experiments since its gradient is small.

### 3.3 Properties of index matched fluid

Refractive index matched fluid properties such as density and viscosity are important to measure for fluid analogy and Reynolds number calculation to perform turbulence slurry flow experiments. A rheometer (AR-G2, TA Instruments) was used to measure dynamic viscosity of the RIM fluid. The AR-G2 rheometer works with three different type of geometry: concentric cylinder, cone and plate, and parallel plates for the viscosity measurements. In present measurements, the viscosity of the KSCN solution was measured using concentric cylinder geometry. The rheometer was connected to temperature control unit to maintain a constant temperature of 25 °C during the measurement.

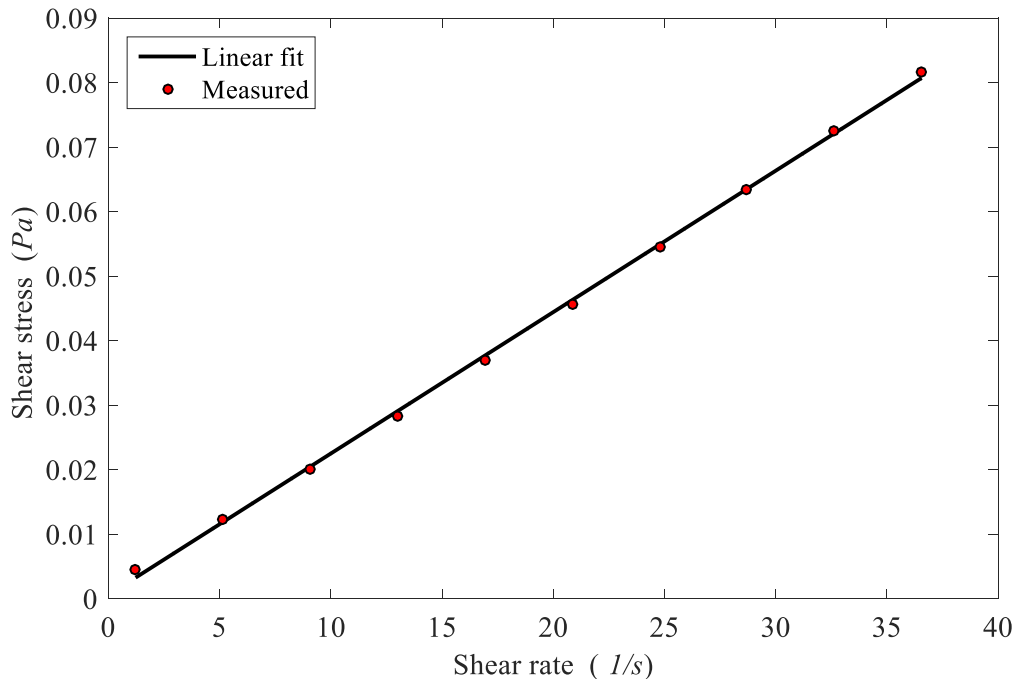


Figure 3.14: Variation in shear stress with shear rate for index matched fluid

Shear stress is plotted against shear rate for index matched fluid as shown in Figure 3.14. It can be noted that shear stress varies linearly with shear rate; means that

index matched solution is a Newtonian fluid. Results of shear stress and shear rate are fitted in a linear model. Shear stress and shear rate correlation is given by following to estimate slope:

$$\sigma = 0.0022 \dot{\gamma} \quad (3.15)$$

where  $\sigma$  is shear stress and  $\dot{\gamma}$  is shear rate. The slope or gradient gives the dynamic viscosity of the fluid. It is clear from Equation (3.15) that 62.4 % w/w KSCN solution has a dynamic viscosity ( $\mu$ ) = 2.2 mPa-s.

The density of 62.4 % KSCN solution was measured using a 10 ml capacity pycnometer (KIMAX<sup>TM</sup>, FisherScientific) at 25 °C. The density was found to be 1380 kg/m<sup>3</sup>. Density and viscosity measurements are tabulated in Table 3.2. Refractive index matched solution is a Newtonian fluid and has a kinematic viscosity 1.79 times greater than DI water. In conclusion, the properties of RIM solution suggest that KSCN solution can be used as reasonable fluid analog for the study of turbulence in slurry flows.

Table 3.2: Properties of index matched KSCN solution at 25 °C

Density ( $\rho$ )	1380 kg/m <sup>3</sup>
Dynamic viscosity ( $\mu$ )	2.2 mPa-s

### ***3.4 Summary and conclusions***

The refractive indices of aqueous KSCN solutions were measured for wide range of concentration  $c = 0 - 70.5$  % and temperature  $T = 20 - 40$  °C using a refractometer.

The refractive indices of the KSCN solutions increase with concentration in a nonlinear fashion for all solution temperatures. Furthermore, refractive index does not decline considerably with the rise in solution temperature for the tested concentration and temperature ranges here. Experimental measurements of refractive index ( $n_{\text{KSCN}}$ ) are fitted onto a quadratic function of concentration and a linear function of temperature to develop an empirical model. It is also observed that the concentration gradient of KSCN solution is three times less than the commonly used index-matched NaI solution.

In reflectance measurements, signal and reference intensity are measured for the full KSCN concentration range (0 - 70 %). The signal intensity presents the amount of light scattering from the solid object hanging in the rectangular beaker of KSCN solution. It is noticed that the signal intensity drops significantly with the rise in KSCN refractive index. Results of the signal to reference intensity ( $S/S_R$ ) data with refractive index are fitted onto a non-linear second order polynomial empirical expression relating reflectance from a Pyrex plate due to variation in KSCN concentration based on Fresnel equations.

Calibration target dot images were captured for different KSCN concentration in a beaker having half-filled KSCN solution and remaining half filled packed bed beads. The results propose that dots are clearly visible in packed bed of beads at 62.4 % KSCN concentration. Additionally, concentration and temperature sensitivity are reported for index matched KSCN solution with Borosilicate glass beads. Properties of index matched fluid are measured. Index matched fluid is a Newtonian fluid and its kinematic viscosity is 1.79 times greater than de-ionized water.

## CHAPTER 4: LARGE SCALE VERTICAL FLOW LOOP FOR REFRACTIVE INDEX MATCHING SUSPENSIONS

This chapter describes a uniquely designed pilot-scale vertical pipe loop facility for refractive index matched measurements in turbulent solid-liquid flows. Feed materials used for slurry preparation in the pipe loop are also discussed. The commissioning of the 50 mm vertical flow loop, which involved flow rate and pressure loss measurements, is also explained in detail. Standard/safe operating procedures for operating the loop and obtaining particle image velocimetry measurements in the presence of a concentrated toxic solution are prepared and reported. Finally, a rotary lobe slurry pump performance and its compatibility in the vertical loop are described in detail.

### ***4.1 Introduction***

Experimental pipe flow data are generally achieved in slurry flows using two broad experimental methods: *once through* flow systems and *recirculating* flow loops [58]. In *once through* flow systems, slurry is supplied continuously during the course of experiments. In *recirculating* flow loops, slurry is recycled and returned directly to the inlet of pump through a feeding tank [58]. *Recirculation* flow loops are widely used and located at a pilot-plant facility due to its advantage over *once through* flow systems [58]. Depending on the application, recirculating flow loops can be horizontal, vertical or inclined. In present study, local properties of slurry mixtures are studied in vertical pipe flow loop. A large scale flow loop for RIM suspensions is built to see the effect of slurry particles on fluid turbulence. Designing and operating the vertical flow loop for handling

corrosive and abrasive slurry is a challenging task that has not yet been done before in our laboratories. The present vertical flow loop is different in terms of design and operation in comparison to the vertical loop used by previous researchers for slurry applications. Toxic and corrosive slurry makes turbulence measurements in concentrated solid-liquid flow quite challenging. Table 4.1 describes the main design and operational modifications required in the vertical loop for refractive index matched suspensions.

Table 4.1: Key changes in present and past made vertical flow loop

<b>Properties</b>	<b>Past vertical loops</b>	<b>Present vertical loop</b>
Carrier phase	Nontoxic and non-corrosive	Toxic and highly corrosive
Pumps	Centrifugal	Corrosive-resistant rotary lobe
Pipe material	Stainless steel/steel	Stainless steel SS-316 L
Hoses	Standard hoses	High pressure, chemical resistant
Pressure dampener	Not required	Installed
Mechanical seal	Gland packing	Double mechanical seal
De-aeration	Entire flow loop completely	Left and right side of loop separately
Spent slurry	Flush by drain line	Retrieved into a storage tank for future use
Fluid preparation	Not required	Required properly designed mixer to prepare toxic carrier phase
Operational procedure	Simple to operate	Challenging due to toxic fluid
Safety	In general safe to operate	Complexity during preparing, loading and unloading the slurry
Temperature control	Essential to control	Significantly more important
Cost	Cheaper to build	Relatively expensive due to design, materials and operational procedure

It is clear from Table 4.1 that the loop is different from design and operational points of view than the previous vertical loop. For example, the pump, hoses and other material were corrosive resistant to handle the slurry. Standard operational procedures were also different than past operational procedures as it was essential to charge the toxic slurry in safe manner.

#### ***4.2 Experimental apparatus and instrumentation for vertical loop***

An isometric view of the 50 mm vertical loop facility for RIM suspensions is shown in Figure 4.1. Aqueous KSCN solution as continuous phase and borosilicate glass beads as dispersed phase were used for RIM suspensions, respectively. A mixer was designed to prepare a uniform, concentrated KSCN solution in a 113 L plastic mixing tank (1). An electric motor (RW20 digital, IKA) was mounted to the mixing tank with a 3-blade axial flow impeller (A315 Lightning, SPX flow). KSCN salt was added using a funnel attached to the top of the plastic lid. A 0.5 HP peristaltic pump (B/T 91 Masterflex, Cole-Parmer) was selected to transfer solution from the mixing tank to the feed tank (2) as shown in Figure 4.1.

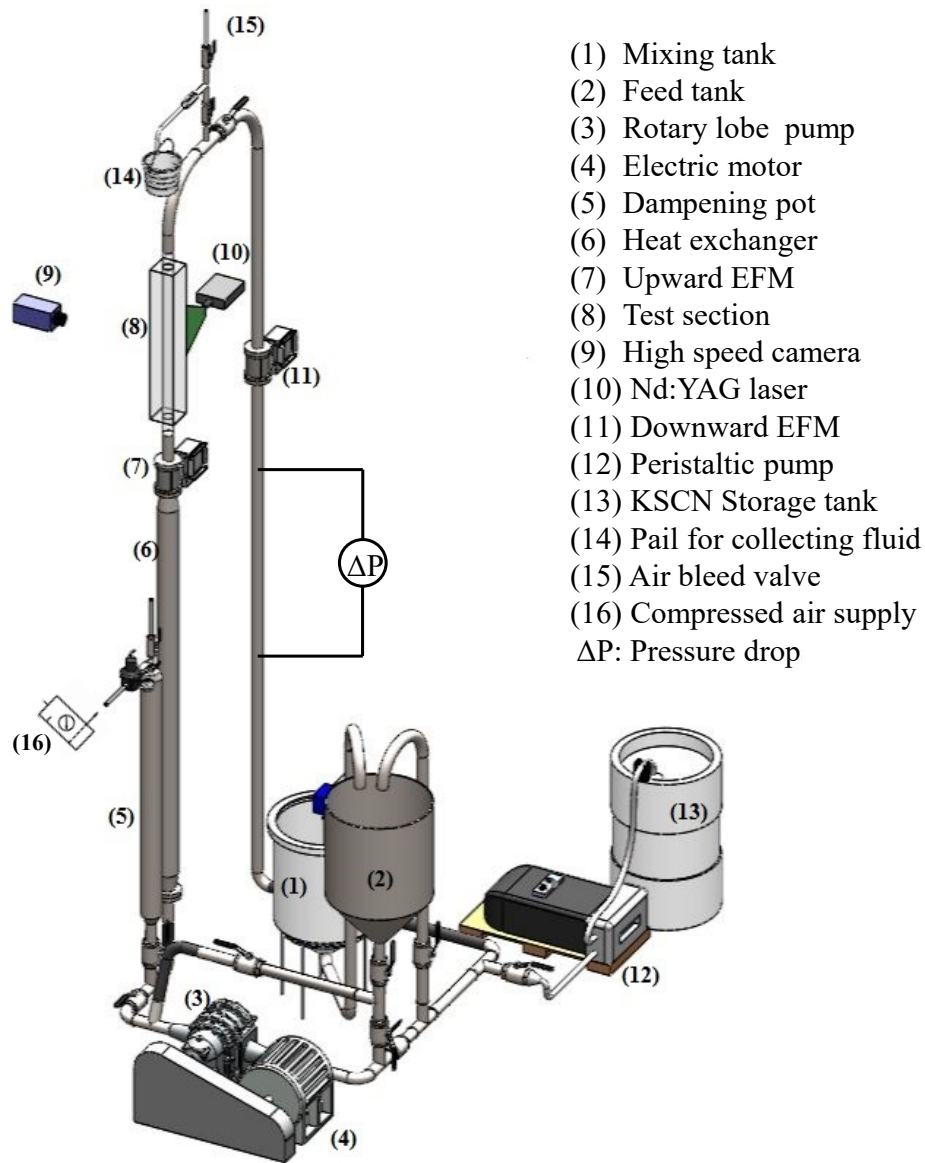


Figure 4.1: Isometric view of 50 mm vertical loop facility for RIM suspensions

The experimental facility used in this study consists of a 2'' nominal diameter and 6.5 m height vertical pipe flow loop. The flow loop was constructed using Schedule - 40 stainless steel (SS-316 L) pipe. Several stainless steel (SS-316 L) ball valves were installed to charge and discharge the toxic slurry in the loop. Chemical/corrosive resistant

positive displacement rotary lobe pump (CM50 rotary pump, Lobe Pro) was chosen to pump the slurry in the vertical pipe loop. The pump had a rated capacity of 0-300 gallons per minute (GPM) and a working pressure of 125 psi. The pump had a size of 4''×4'' and was made of type 316 stainless steel to handle corrosive slurry. The pump was specified to handle up to 3 mm size solid hard particles. The helix-profile lobe was made of fluoro elastomer (FKM) and had 4 lobe wings. The core of the lobe was made of steel. Figure 4.1 displays the rotary pump (3) and electrical motor (4) connection through a belt pulley mechanism. The pump was powered by a 20 HP electric motor (Inverter shield, Hyundai motors) to circulate the slurry in the loop. The mixture flow rate was adjusted by changing the pump speed using a variable frequency drive (Altivar 61, Schneider electric). A dampening pot (5) was installed into the discharge side of the pump. The pressure dampener had a 4'' diameter and was 1.5 m vertically long. It absorbed pulses generated by the rotary pump. Additionally, it was used to pressurize the loop to avoid pump cavitation. The dampener was connected to a 90 psi compressed air supply line (16). This pressure was controlled by a pressure regulator.

A non-intrusive electromagnetic flow meter (EFM) (7, 11), a commercial device (9200A-IMT25, Foxboro) was located in each of the upstream and downstream sections of the loop to measure the flow rate of slurry. A double pipe heat exchanger (6) was installed in the upward section of the loop to control the temperature of carrier fluid. The heat exchanger was 2.0 m long and had an annulus with 3'' diameter. The temperature was controlled by circulating domestic cold water in the annulus of the double pipe heat exchanger. An actuator (120-SR, Belimo) was installed in the outlet of the heat exchanger to maintain the required temperature. The heat exchanger absorbed the heat

generated by the pump and friction losses in pipes. A temperature sensor installed downstream of the heat exchanger (RTD assembly, Aircom Instrumentation Ltd.) measured the temperature of the slurry mixture.

PIV measurements were performed at transparent test section (8), made of Plexiglass. The inner diameter of the test section was  $D = 50.6$  mm and 2 m long. A PIV camera (9) and Nd: YAG laser (10), as shown in Figure 4.1 was used for optical measurements. The imaging and optical system consisted of a camera (Imager Intense PIV camera, LaVision GmbH) and a laser (Solo III-15 PIV, New Wave Research). Experiments were conducted in the closed vertical loop by using an isolation valve to the feeding tank at constant temperature of 25 °C. Before PIV measurements, entrained air was completely purged by an air bleed valve (15). The small amount of solution coming out during purging was collected in a pail (14) as shown in Figure 4.1.

During commissioning of the loop, differential pressure transducer (DP-15, Validyne Engineering) was used to measure pressure loss in the downflow side of the loop. Pressure taps were located 1.3 m apart in the downward side of the loop as displayed in Figure 4.1. A demodulator (CD15, Validyne Engineering) was connected with pressure transducer to provide a DC output signal for steady state measurements. The magnetic flow meters, differential pressure transducers, and temperature sensor delivered analog signals. The analog signals were converted into digital signals by a data acquisition unit (NI cDAQ-9174, National Instruments). A custom program for data acquisition was written in a commercial code (LabVIEW, National Instruments) and was used to monitor and record these outputs in real time. Calibration data of the magnetic

flow meters, differential pressure transducer, and temperature sensor was incorporated into the software program to record the data in physical units as well.

KSCN solution was discharged back to plastic storage tank (13) after completion of PIV measurements. The solution was transferred into the storage tank using a peristaltic pump (12). The loop was completely flushed and cleaned with water between uses. It was important to dry out loop completely for future experiments, especially left over water in the horizontal section of loop. Finally, a portable air blower (Qmark, Power Cat) was connected to discharge side of pump to dry out the loop for the next set of experiments.

### ***4.3 Materials***

RIM fluid, 62.4% KSCN solution, was prepared using de-ionized water and potassium thiocyanate salts. Freshly de-ionized water was collected from a water purification system (Elix Advantage, Millipore SAS). The material safety data sheet (MSDS) [59] of the salt was reviewed to understand the important properties and safety remarks. Seeding particles, 2  $\mu\text{m}$  silver-coated fused silica spheres (SG02S40, Potters Industries Inc.) were used to seed the flow during PIV measurements [60]. Two types of slurry beads were used during experiments: 3 mm borosilicate glass slurry beads (Z143928, Sigma-Aldrich) [57] and 3 and 0.25 mm glass beads (Manus impact beads, Potters Industries Inc.) [61]. Borosilicate and glass beads had density of 2230  $\text{kg/m}^3$  and 2500  $\text{kg/m}^3$ , respectively.

## ***4.4 Experimental procedure***

This section discusses the standard operating practice to run toxic, corrosive and abrasive slurry in the vertical flow loop. The procedures to prepare the KSCN solution, to feed the solution into the feed tank, to charge and unload the slurry are explained in detail.

### **4.4.1 Preparation of KSCN solution**

The vertical flow loop, feed tank, and dampening pot volumes were measured experimentally before starting the solution preparation. It was important to know the required the KSCN solution volume for the experiments. Based on the loop volume measurements, a total 75 L of solution was prepared. Aqueous KSCN (62.4 % w/w) needed 39 kg of DI water and 65 kg KSCN salts. Due to the toxic nature of solution, all personal protective equipment like face shield, gloves, respirator, and safety glasses were used to prepare the KSCN solutions. Table 4.2 outlines the safe and standard operating work practices to prepare the solution.

Table 4.2: Safe work procedure to prepare KSCN solution	
Steps	Procedure for KSCN preparation
1	Add 39 L of required DI water into the 113 L mixing tank
2	Turn on the electric motor and the start mixing the water
3	Weigh each box of KSCN salt
4	Add the salts into the funnel attached to the mixing tank slowly
5	Weigh the empty box and record the data in a spreadsheet
6	Add the salt slowly as KSCN dissolution is an endothermic reaction
7	Keep adding salts until the required amount of KSCN salt is added to the mixing tank
8	Measure the refractive index, viscosity and density of the fluid
9	Seal the mixing tank tightly for future use

In step 3, each 2.5 kg container of KSCN salts included large chunks of KSCN salts. These chunks were formed due to humidity that makes KSCN salts powder to stick on each other and creates the lumps. These chunks were broken down into fine particles by crushing them so that salts could dissolve into the DI water easily and help during uniform solution preparation. In step 8, fluid properties were measured once the required concentration of 62.4% solution is achieved. In step 9, mixing tank was sealed to avoid any water vaporization.

#### 4.4.2 Feeding the solution from mixing tank into the feed tank

During this step, the slurry pump is set to the shutdown position. All valves are closed except V13, which is always open as labelled in Figure 4.2. The standard operating procedure is summarized in Table 4.3.

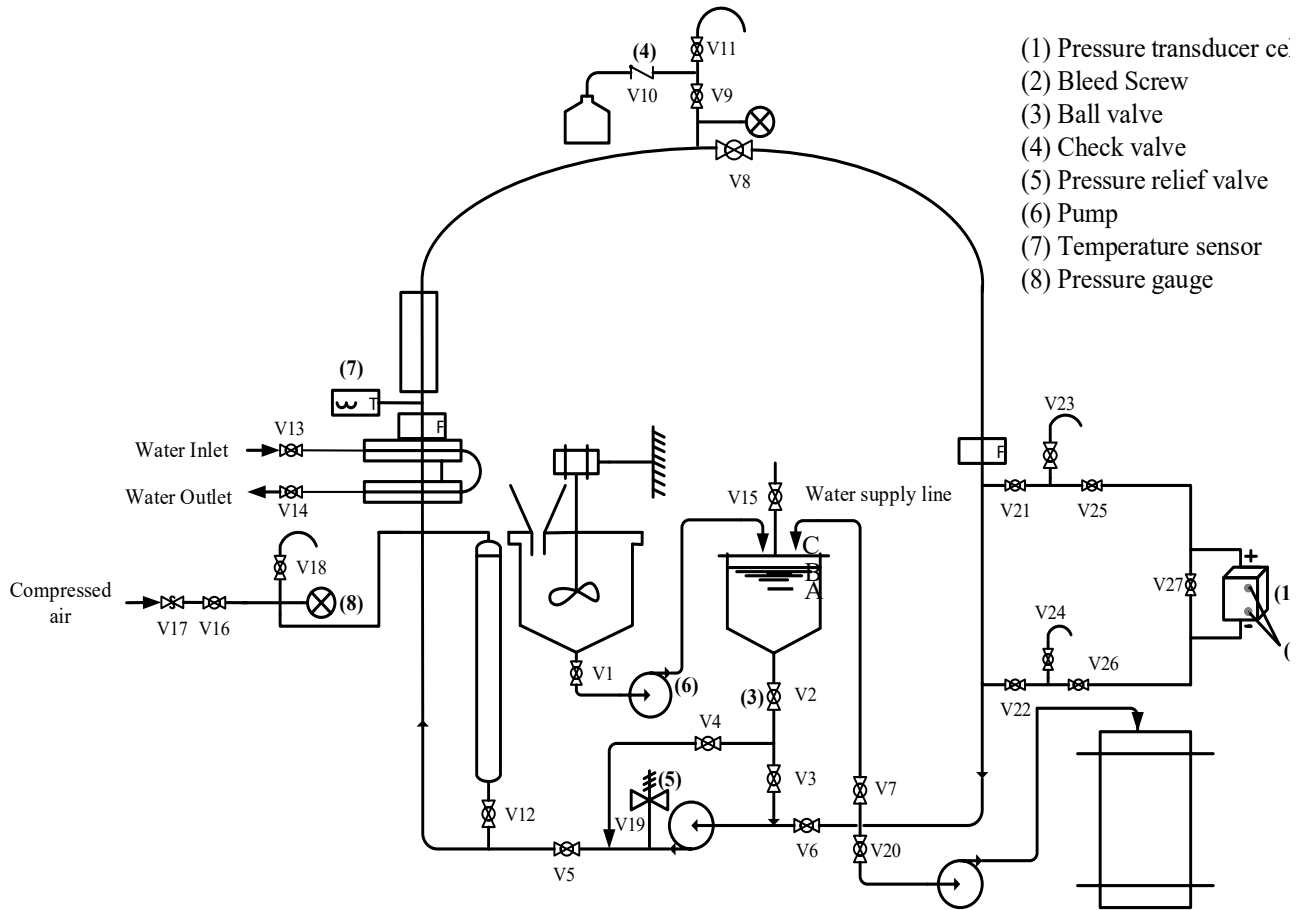


Figure 4.2: Layout of experimental vertical loop facility

Table 4.3: Procedure of feeding the solution from mixing tank into the feed tank	
Steps	Procedure of feeding the solution
1	Add 3-4 grams the seeding/tracer particles into the mixing tank and mix them with solution
2	open valve V1 and turn on the peristaltic pump
3	When the solution in the feeding tank is at level 'C' as shown in Figure 4.2, turn off the peristaltic pump
4	Close valve V1 once the pump is turned off

In step 1, mix the seeding particles until the seeding particles are well mixed with the solution. During step 3, make sure that peristaltic pump is turned off as positive displacement pump can't run under closed valve operation.

#### 4.4.3 Equalizing the level of feed tank and dampening pot

During this step, the slurry pump is under shutdown condition. V18 must be open. V3, V6, and V16 must be closed. The other valves are closed as well. Standard operating practice is shown in Table 4.4.

Table 4.4: Procedure of equalizing the level of feed tank and dampening pot	
Steps	Procedure of equalizing the level of feed tank and dampening pot
1	Open V2, V4, V5, and V12, respectively
2	The level in the feed tank and dampening pot will be equalized
3	Close V4, V12, and V18, respectively

#### 4.4.4 Charging solution into the flow loop

The left and right legs of the loop are charged separately as the pump was able to run in both forward and reverse directions. During the charging of left leg, valves V4, V6, V7, V8, V11, V12, V16, V18, and V20 are closed. The standard procedure is summarized in Table 4.5.

During step 2, all the entrained air in the left side of the leg will start coming out. Once solution starts to come out from V10 into the pail, it means all air has been removed from the left leg of the loop. In step 3, check valve (V10) shown in Figure 4.2 would not allow any back flow of solution into the feeding tank. To be safe, V5 must be closed as well immediately after the pump is shut down. During step 5, all the entrained air in the right leg will start coming out. Once solution starts to come out from V10 into

the pail, it means all air has been removed from the right leg of the loop. During step 8, loop was pressurized again to remove any leftover air for safe side due to wrong charging. V12 and V16 must be opened while keeping V18 closed in step 8. Pressure was regulated to 30 psi for pressurizing the loop with the regulating valve V12.

Table 4.5: Procedure of charging solution into the flow loop	
Steps	Procedure of charging the solution
1	Open V3, V5, V9 and V10, respectively while leaving V2 open.
2	Start the slurry pump and run it slowly in the forward direction at 110 RPM.
3	Before closing valve V5, shut down the pump.
4	The left side of leg is now charged. To charge the right leg, valves V4, V6, and V8 are opened while V3, V7, V20, and V5 are closed.
5	Start the pump in reverse and run the pump slowly at 110 RPM.
6	Again to be safe, V6 must be closed immediately after the pump is shut down. The right side leg is now charged as well.
7	Open V5, V6, and V8 while valves V2, V3, V7, V18, and V20 are closed.
8	Pressurize the loop by compressed air while the pump is still shut down
9	When solution starts come out from V10 into pail, close V9 and V10.
10	Depressurize the loop again by closing V16 and opening V18 respectively.
11	Turn on the heat exchanger by opening the valve V14

The loop is now charged with KSCN solution and all the air has been removed from the system. The level in the feed tank will drop down to level “A” as shown in Figure 4.2. Before running the slurry pump, one make must sure that V5, V6 and V8 are open to add slurry particles. Valves V2, V3, V7, V9, V10, V18 and V20 are closed. The

pump is then set to provide a fluid velocity of 4 - 5 m/s. During step 11, the heat exchanger was set to 25° C.

#### 4.4.5 Loading slurry particles

The loop was run at a fluid velocity of 4-5 m/s during the loading of particles. It is advisable that coarse slurry particles such as 2 or 3 mm should be added at higher speed in slurry flow application to avoid settlement of the particles. Table 4.6 shows standard operating procedure for loading slurry particles.

Table 4.6: Standard operating procedure for loading slurry particles	
Steps	Procedure of loading slurry particles
1	Open V2 and V3. V4 and V7 must be closed
2	Add the slurry particles into the system manually and slowly to avoid any entrainment of air
3	Once all slurry particles are added, close both V2 and V3
4	Slow down the pump speed and run the loop just above deposition velocity (1.5 m/s)

After loading the slurry particles, the level in the feeding tank will go up from 'A' to 'B' which is shown in Figure 4.2.

#### 4.4.6 Pressurization of the loop

The loop was pressurized to avoid pump cavitation at higher flow rates and vacuum at top location of loop at lower flow rates. During this step, V12 and V16 must be opened while keeping V18 closed. Regulate the pressure required to pressurize the loop with the regulating valve V12; this should be set to 30 psi. Table 4.7 discusses standard operating procedure to pressurize the loop

Table 4.7: Procedure for pressurization the loop	
Steps	Procedure to pressurize the loop
1	Fix the regulating valve setting when vacuum gauge reading, attached to top of the loop, is above zero atmospheric. The loop is now pressurized
2	Fix the speed of the pump for desire flow rate in loop for PIV measurements

For safety reasons, a pressure relief valve was installed in the downstream of the pump if due to any reason excessive pressure is built into the loop so it could completely blockage the discharge pipe. Speedkeen socks and spill kit were used in case of any spill or leakage while operating the loop.

#### 4.4.7 PIV measurement

During PIV measurement, the view box should be filled with water. PIV test section was covered by black curtains to avoid any laser hazard. Class 4 laser safety glasses were used during PIV operation. Table 4.8 shows PIV measurements procedure.

Table 4.8: Procedure for PIV measurements	
Steps	Procedure of PIV measurements
1	Turn on the PIV camera and laser. Set the laser power and time interval between images
2	Take sufficient images for PIV analysis
3	Once measurements are completed, shut off laser and camera

#### 4.4.8 Depressurization of the loop

Loop was depressurized after completion of PIV measurements. During this procedure, loop was run at just above deposition velocity. Standard operating procedure of depressurization of the loop is illustrated in Table 4.9.

Table 4.9: Standard operating procedure to depressurize the loop	
Steps	Procedure of depressurization of the loop
1	Decrease the pump speed and run the loop just above deposition velocity.
2	Close V16 and open V18 to depressurize the system.
3	Close V18 when system is depressurized

#### 4.4.9 Unloading the slurry particles

A screen was put on the top of the feed tank to unload the particles. During this process, open V6 for a few seconds and close it again since there might be some particles stuck at near to valve V6. Procedure to unload slurry particles is explained in Table 4.10.

Table 4.10: Procedure of unloading the slurry particles	
Steps	Procedure for unloading the slurry particles
1	Open valve V2 and V3. Open V7 then close valve V6 in order to run loop in open loop.
2	Particles will start to settle into the screen, and the solution will still recirculate into the loop.
3	Once all particles are settled into the screen, open valve V6 then close V7 in the order
4	Shut down the pump

#### 4.4.10 Unload the solution into storage tank

During this process, the slurry pump is under shut down position. Unloading of the KSCN solution into storage tank was relatively easy as the pump does not work as a closed valve under shut down condition.

Table 4.11: Procedure to unload the solution into storage tank	
Steps	Solution unload procedure back into storage tank
1	Open V4, V9, V7, V11 and V20 respectively. V2, V3, V5, V6, V8, V12 and V18 are already open
2	Most solution will drain into the storage tank. Additionally, a peristaltic pump was used to recover any leftover solution from the horizontal section of loop

The loop cleaning was required since loop surface were exposed with corrosive KSCN solution. Loop clean up procedure with fresh water is discussed in Appendix A1. A total of 27 valves were used to operate this vertical slurry pipe loop for RIM suspensions. For additional precaution, a check list of all the valves' positions at different steps of the operation was prepared and reported in Appendix A2. Additionally, the pressure loss measurement operational procedure is discussed in Appendix A3.

## ***4.5 Commissioning of vertical pipe flow loop***

The large-scale vertical flow loop for refractive index matching suspensions was designed and operated differently than other loops that researchers have used in the past. It was important to commission this loop for future use. Proper standard operating procedures (SOP), as described in Section 4.4, were followed to purge all the entrained air out from loop and charge water. During commissioning, pump cavitation problems occurring at high flow rates were solved by pressurizing the loop. All leaks from joints, coupling and fittings in the pipe loop were fixed. Additionally, the loop volume was measured to identify required volumes of KSCN solution (carrier phase) and slurry particles (disperse phase) needed for turbulence measurements. Meanwhile, pressure loss was measured in the downside of the vertical loop for water as part of final commissioning steps. Measured pressure loss across the fixed length of pipe section was compared with the calculated one. The magnetic flow meters were also tested for different slurry concentrations and particle sizes.

### **4.5.1 Pressure loss measurement**

Friction losses are most important features in pipe flow and pipeline design to understand the hydrodynamics of the system. During commissioning, the pressure loss was measured across 1.3 m pipe length having inner diameter 53.43 mm. A pressure transducer (DP15, Validyne Engineering) was used in the downflow side of the loop to determine pressure difference. The pressure transducer cell was connected to a sine wave carrier modulator to provide a DC output signal for steady state measurements. The differential pressure transducer was calibrated using a dead weight tester at the Chemical

and Materials Engineering workshop at the University of Alberta. Calibration data was used in the data acquisition software program to record pressure data in units of pressure. Before the measurements, standard operating procedure was used to purge and bleed the system completely. At each flow rate, a differential pressure value was recorded at a sampling rate of one second for six minutes. The average flow rate and pressure data were analyzed to understand pressure loss variation with bulk velocity. Differential pressure was measured for bulk velocities ranging between 0.5 - 4.5 m/s.

The bulk (or mean) velocity of the flow is given by:

$$V = \frac{Q_{\text{avg}}}{A} \quad (4.1)$$

where  $V$  is bulk velocity of flow,  $Q_{\text{avg}}$  is average flow rate over a certain period of time, and  $A$  is pipe cross sectional area.

The calculated pressure drop over a pipe section of length  $L$  is specified by:

$$\Delta P = f \frac{l}{D} \frac{\rho V^2}{2} \quad (4.2)$$

where  $f$  is the Fanning friction factor,  $l$  is the length of pipe,  $D$  is the pipe inner diameter, and  $\rho$  is the density of fluid.

Swamee and Jain [62] developed an expression for the Fanning friction factor to solve it directly without any iteration for turbulent flow, which is valid in the Reynolds number range of 5000 to  $3 \times 10^8$  and is given by:

$$f = 0.0625 \left[ \log_{10} \left( \frac{\varepsilon/D}{3.7} + \frac{5.74}{Re^{0.9}} \right) \right]^{-2} \quad (4.3)$$

where  $\varepsilon$  is hydrodynamic roughness of the pipe,  $D$  is pipe inner diameter, and  $Re$  is flow Reynolds number determined from Equation (2.5). For this particular pipe section,

hydrodynamic roughness was estimated as 0.002 mm since physical roughness of pipe was not measured during the measurements. Typical physical pipe roughness of 2 inch schedule-40 stainless steel is 0.0045 mm.

Pressure drops were calculated using Equations (4.2) and (4.3) and plotted against bulk flow velocity. Additionally, measured pressure losses were plotted.

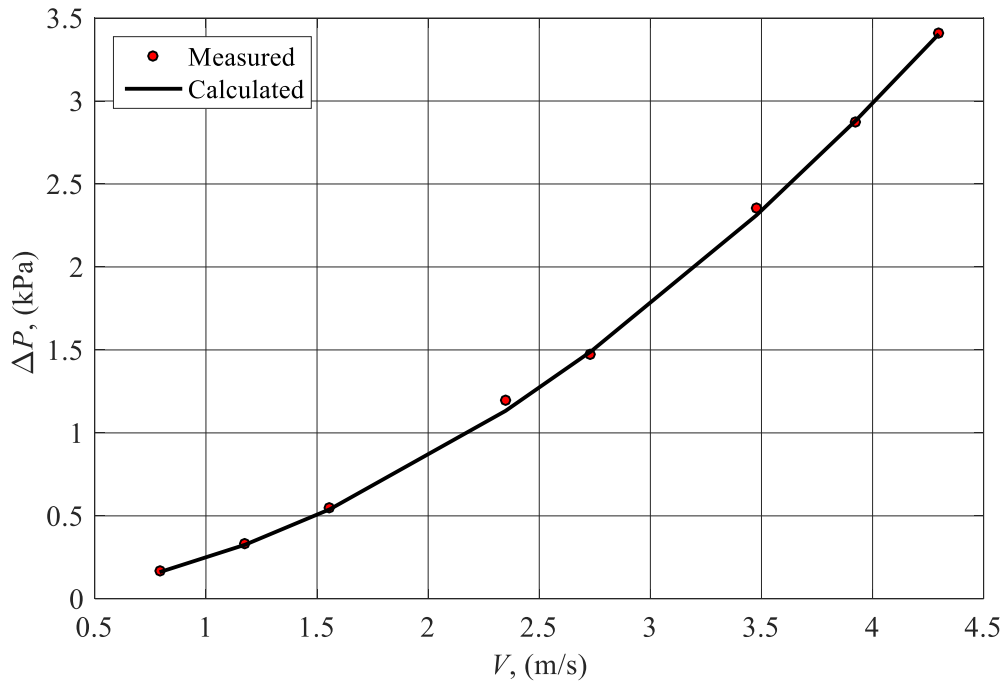


Figure 4.3: Variation in measured and calculated pressure loss with bulk velocity for water

Figure 4.3 shows the variation in measured and calculated pressure losses with the bulk velocity in the downside of the vertical loop. It is clear from Figure 4.3 that the measured and calculated pressure drop data are very similar for a wide range of flow rates.

#### 4.5.2 Slurry flow rate measurement

Both in industry and academia, electromagnetic flow meters have been used for single-phase instrumentations, such as mean velocities of liquid phase. As these flow meters do not cause any additional pressure drop and have quick response to flow, they are also suitable for slurry flows [63]. Apart from this, electromagnetic flow meter measurements are immune to fluid and flow properties such as pressure, fluid density, viscosity, temperature, and some extent to conductivity [58, 64, 65].

Magnetic flow meters work on the principle of Faraday's law of electromagnetic induction. A uniform magnetic field is created across the pipe by a pair of electrodes [58]. Electrically conducting fluid flowing through the magnetic field induces a voltage difference. The voltage signal received by electrodes is conditioned by a transmitter and converted into flow rate. The magnetic flow meter used in present study consisted of a flow tube paired with flow transmitter, which excited the flow tube using a pulsed DC technique. The transmitter converts the signal voltage to a digital output current. The digital output current is converted into physical units by updating the calibration data into data acquisition software program to record the flow rate in liters/min.

Electromagnetic flow meters were installed in the upstream and downstream vertical pipework for slurry flows in present study as suggested by past publications [66]. In order to investigate and test the flow meters, flow rates were measured for single phase (water) flows and then two phase (water + glass beads) mixtures having different concentrations and particle sizes. Measured instantaneous flow rates were sampled at 1 Hz. The flow rate was recorded for sufficient time so that water could pass at least 50

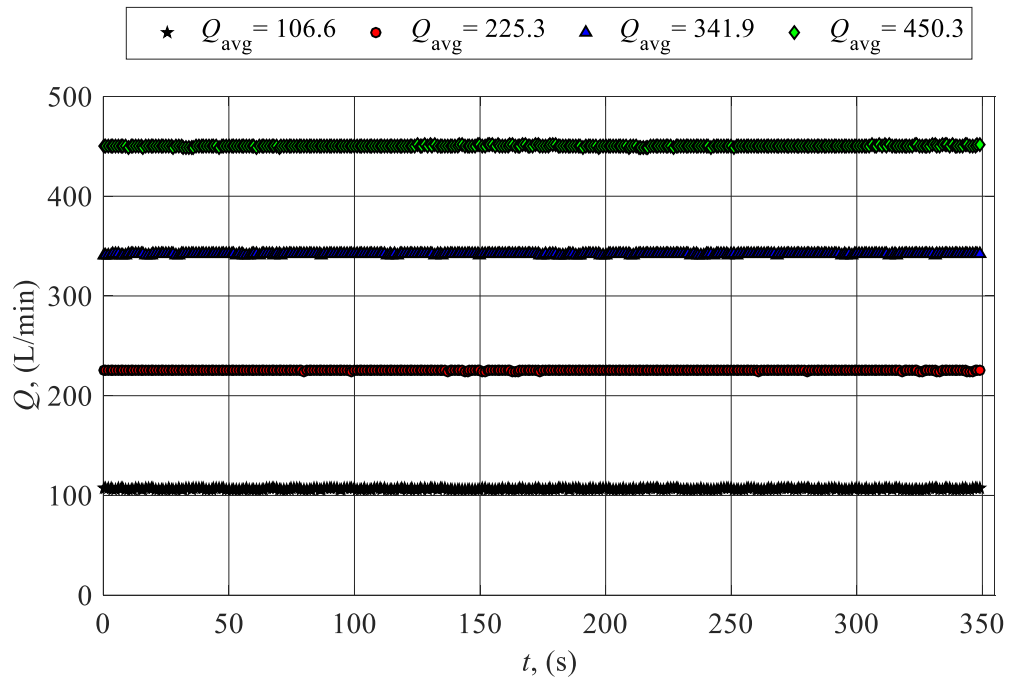
times through both the flow meters during measurements. Average or mean flow rate  $Q_{\text{avg}}$  was calculated by taking the mean over the measured time period:

$$Q_{\text{avg}} = \frac{\sum_{m=0}^{m=m_t} Q(m)}{m_t} \quad (4.4)$$

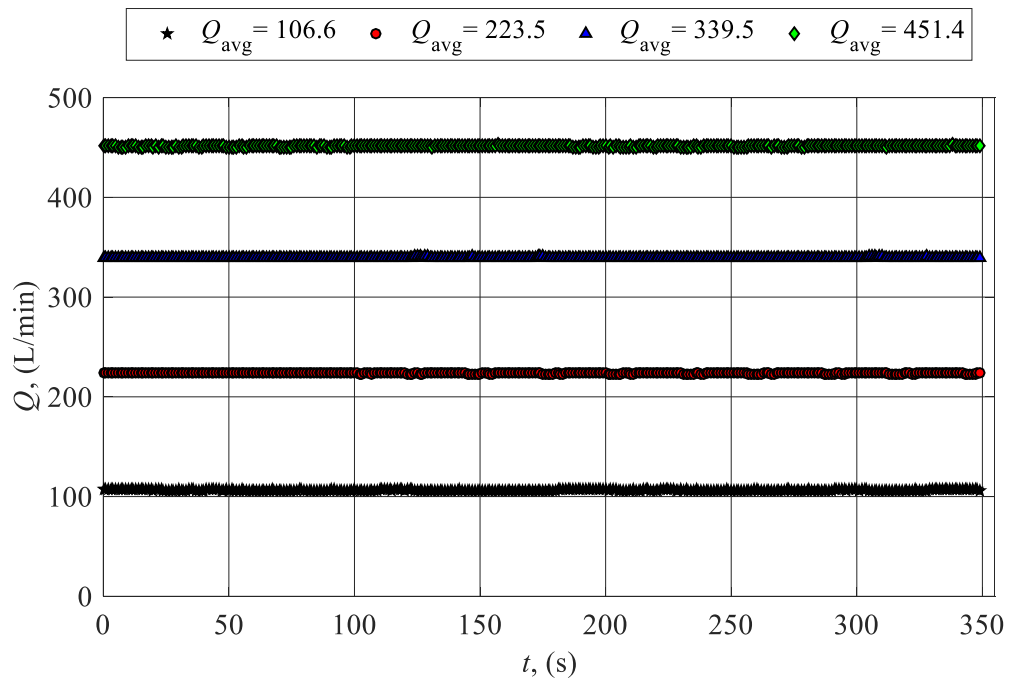
where  $m$  is sample number and  $Q$  is the instantaneous flow rate at particular time  $t$ . Flow rate was measured at equal time intervals where  $m_t$  is total number of samples.

To analyze performance of the flow meters, the flow rate was varied between 0 – 500 L/min by setting a particular pump speed. The volumetric concentration of the disperse phase ( $\phi_v$ ) was also changed from 0.5 % to 15 % to test the flow meters in two-phase flow. Additionally, two different sizes of glass beads ( $d = 0.25$  and  $3.0$  mm) were chosen.

Figure 4.4(a) illustrates flow rate measurements for water at average flow rates  $Q_{\text{avg}} = 106.6, 225.3, 341.9,$  and  $450.3$  L/min over a certain period of time for the upstream flow meter. Figure 4.4(b) shows flow rate measurements for single phase water at average flow rates  $Q_{\text{avg}} = 106.6, 223.5, 339.5,$  and  $451.4$  L/min over a certain period of time for the downstream flow meter. It can be noted from Figure 4.4 that both flow meters provide steady flow rate data.



(a)



(b)

Figure 4.4: Variation in flow rates of water for (a) upstream and (b) downstream flow meter for certain time period

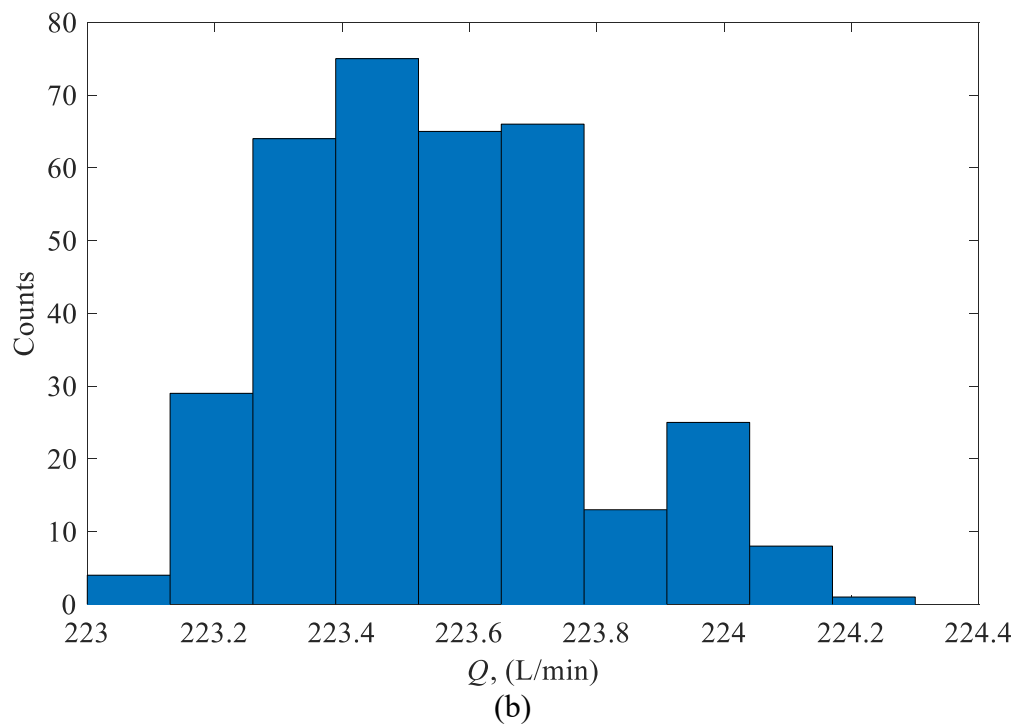
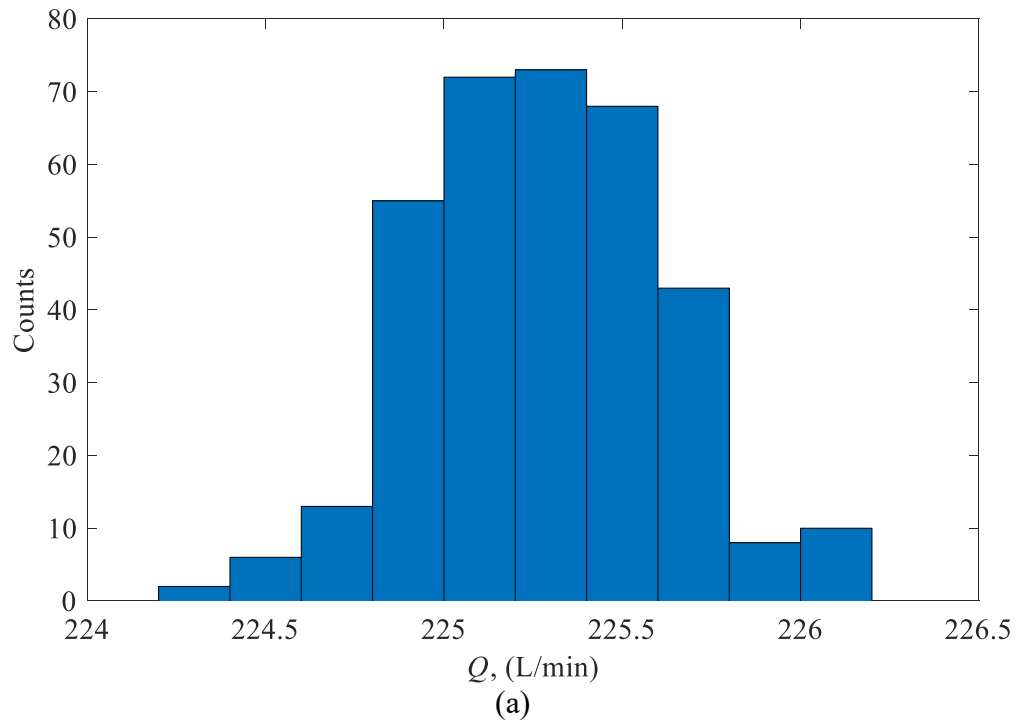


Figure 4.5: Distribution of flow rate for (a) upstream flow meter ( $Q_{\text{avg}}=225.3$ ) (b) downstream flow meter ( $Q_{\text{avg}}=223.5$ )

Figure 4.5(a) and (b) show probability distribution of flow rate measured with upstream and downstream flow meter, respectively. Figure 4.5(a) shows flow rate distribution for  $Q_{avg} = 225.3$  L/min with an uncertainty of 0.16 % whereas Figure 4.5(b) demonstrates flow rate distribution for  $Q_{avg} = 223.5$  L/min with an uncertainty of 0.11 %.

Figure 4.4 and Figure 4.5 give an assurance that both flow meters perform well for single phase flow. Additionally, pressure loss measurements matched with calculated values for the single phase water experiments. It can be concluded that flow meters can be used for measuring flow rate of KSCN solution in single phase PIV experiments.

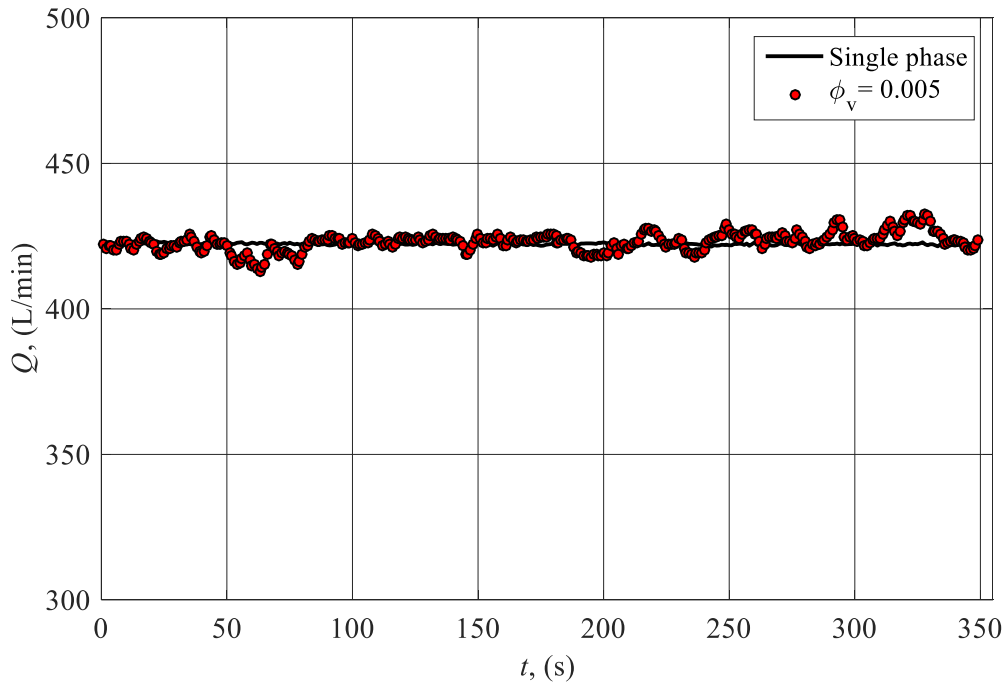


Figure 4.6: Variation of flow rate with time for water and 3 mm beads in very dilute slurry using upstream flow meter

The flow rate data for water (single phase) is compared with dilute slurry having 3 mm size glass beads in Figure 4.6. It can be seen that there is almost no variations in flow rate for single phase water but low fluctuations for dilute slurry over the measured

time for single phase average flow rate of 425 L/min. Pump speed was fixed to compare single phase and dilute slurry flow rate data. Such small variations in flow rates are not very important for slurry application. The data suggest that the flow meters work well with dilute slurry flow.

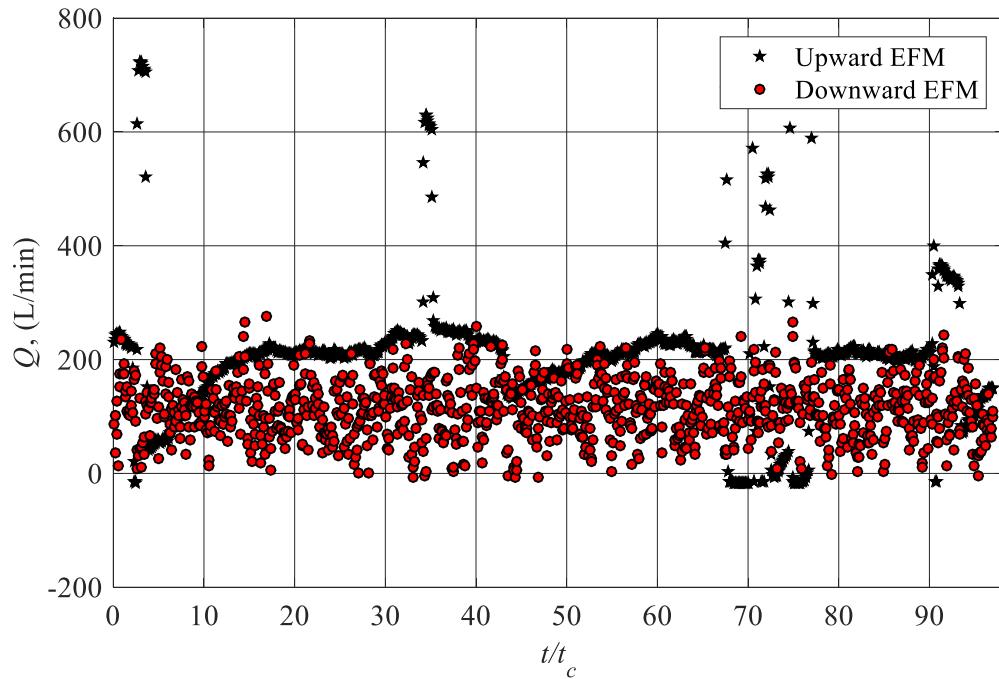
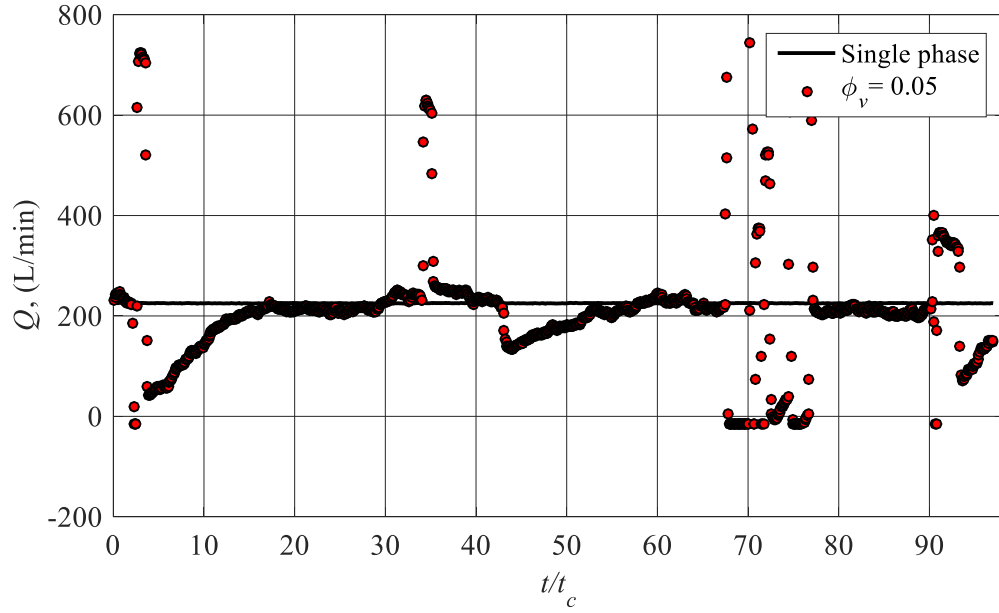
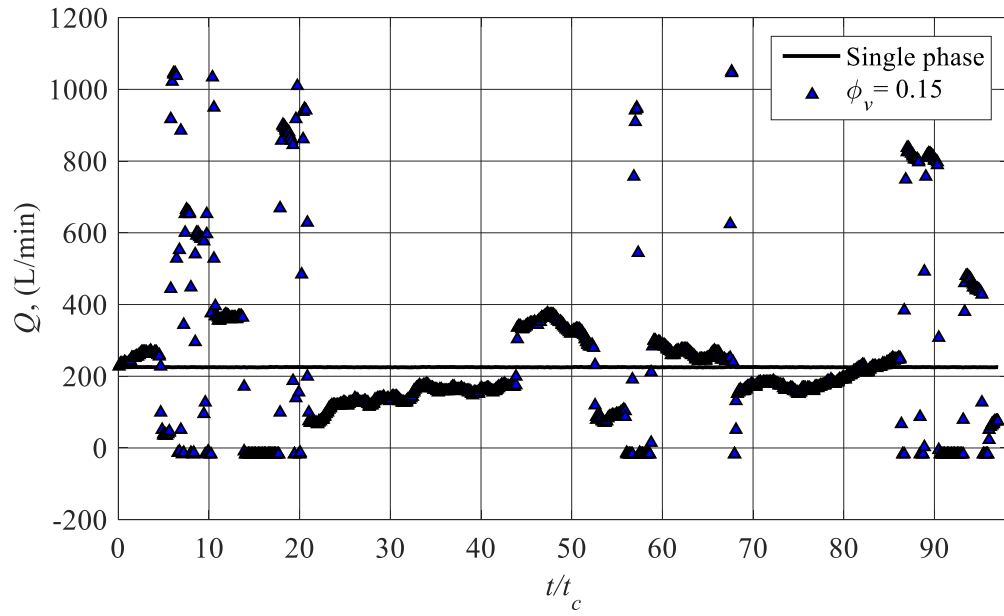


Figure 4.7: Variation in flow rate for upstream and downstream flow meters  $\phi_v = 5\%$  and 3 mm beads slurry over certain loop cycles

Both the upstream and downstream flow meters and their transmitters had the same internal settings. Figure 4.7 shows flow rate variations for the 3 mm beads and 5% concentrated slurry for both flow meters at a pump speed of 300 RPM. Flow rates are plotted against the number of loop cycles ( $t/t_c$ ) in which particular slurry will pass through the flow meters. Cycle time ( $t_c$ ) is defined as ratio of the loop volume to the average volume flow rate for single phase (water). It is surprising to notice from Figure 4.7 that both flow meters behaved completely different while they show identical measurements in single phase flow for water, as shown by Figure 4.4. It is evident that both flow meters have fluctuations from their average value and flow rate data is not steady.



(a)



(b)

Figure 4.8: Flow rate comparison for 3 mm size slurry concentrations (a)  $\phi_v = 0.05$  (b)  $\phi_v = 0.15$

Flow rate data for two different concentrated slurry one having 5 % and other having 15 % concentration are illustrated in Figure 4.8(a) and (b) over a longer time period in terms of loop cycle ( $t/t_c$ ) respectively. Large and random fluctuations are noticed for the concentrated slurry flow. Results are better for the 5 % slurry in comparison to the 15 % slurry.

The slip velocity effect on flow meter measurements was also analyzed. In general, it is accepted that electromagnetic flow meters are based on the assumption that both phases, liquid and solid, move with the same velocity and indeed the average velocity of the mixture is measured [58]. However it is not true in case of vertical flow where there is always slip between the solid and liquid phases. It is commonly accepted that the terminal settling velocity of a spherical shaped bead descending in a Newtonian fluid medium can be taken as a closed approximation of the slip between dispersed and continuous phases [67].

To see the slip velocity effect on flow rate measurements, terminal velocity was calculated for  $d = 0.25$  and 3 mm size particles. The terminal settling velocity was calculated based on direct solution using the Archimedes number. The Archimedes number ( $Ar$ ) based on drag coefficient ( $C_d$ ) is given by following correlation [68]:

$$Ar = C_d Re_p^2 = \frac{4 d^3 g \rho (\rho_s - \rho)}{3 \mu^2} \quad (4.5)$$

where  $d$  is particle diameter,  $g$  is gravitational acceleration,  $\mu$  is dynamic viscosity of the carrier phase, and  $\rho$  and  $\rho_s$  are the carrier and disperse phase densities, respectively.

The particle Reynolds number is calculated from Archimedes number using the following:

$$Ar = 24Re_p + 3.6Re_p^{1.687} \quad 4.8 < Ar < 4 \times 10^5 \quad (4.6)$$

$$Ar = 0.44Re_p^2 \quad Ar \geq 4 \times 10^5 \quad (4.7)$$

The terminal settling velocity ( $V_\infty$ ) is calculated based on the particle Reynolds number by following:

$$V_\infty = \frac{Re_p \mu}{\rho d} \quad (4.8)$$

where  $d$  is particle diameter.

The calculated terminal velocities were 0.03 and 0.36 m/s for particles of  $d = 0.25$  and 3 mm, respectively, based on equations (4.5), (4.6), (4.7), and (4.8). Slip velocity of the 0.25 mm particles is much lower than the 3 mm size particles. Based on slip velocity, it is concluded that flow meter should work better for smaller size particles as they have a smaller slip velocity. To investigate the slip velocity effect, flow rate measurements were conducted for different size slurry.

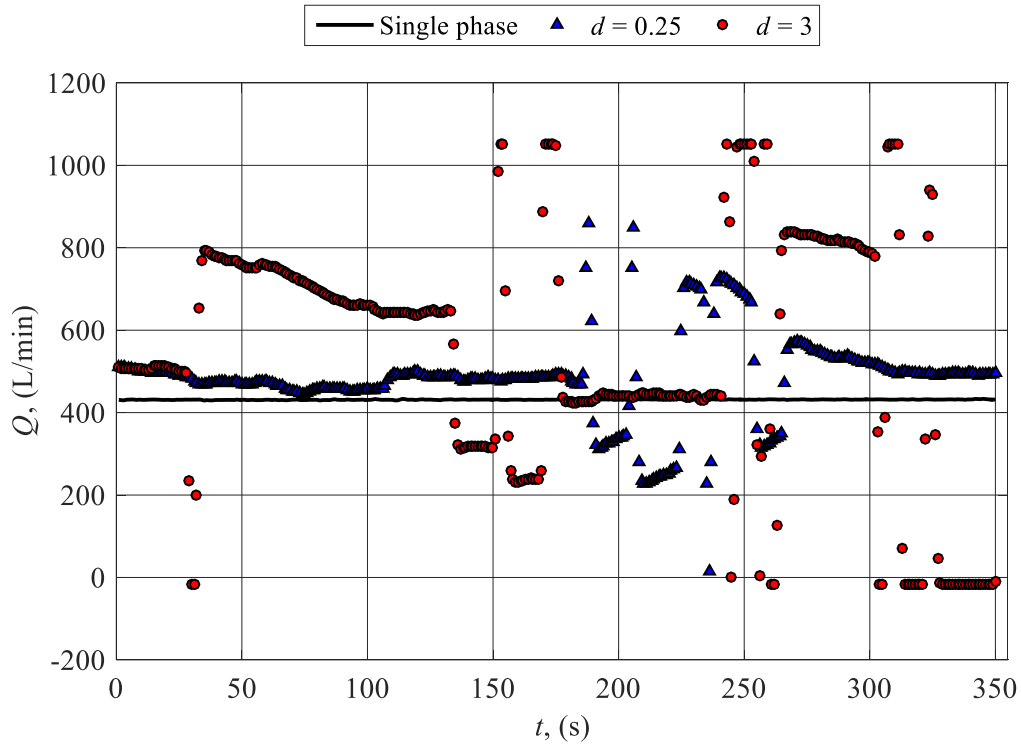


Figure 4.9: Flow rate variation with time for two different size of slurry in upstream flow meter

Figure 4.9 shows flow rate measurements over time for  $d = 0.25$  and 3 mm size concentrated slurry. There are not any significant changes in scattering and fluctuations due to change in particle size. However, flow rate data for 0.25 mm particles relatively has less scattering over the average value than 3 mm size beads.

It is concluded that the flow meter does not work well with the more concentrated slurry. This could be due to the following possible reasons:

- Flow meter is not compatible due to the abrasive nature of the slurry as outlined in a personal communication with Foxboro company (Bruce Simmons, Schneider Electric, Aug 2015)
- The pump is creating large pulsation due to the slurry beads during operation

- Magnetic flow meters work on the principle of electromagnetic induction so it might not work with concentrated slurry having electrically nonconductive solid beads.

## ***4.6 Pump performance and its compatibility***

This section discusses reason behind the selection of a rotary pump for the vertical loop and its performance deterioration after running a set of experiments with RIM slurry. Finally, the pump's incompatibility with the large scale vertical flow loop for RIM suspensions is demonstrated in detail.

### **4.6.1 Pump selection for RIM loop**

Slurry pumps are an important component of flow loop design. A variety of pump types are used in slurry flow applications [58]. They are mainly categorized into two categories: centrifugal and positive displacement. Centrifugal pumps are extensively used in slurry flow as they are mechanically compact and relatively more economical than displacement pumps [58]. Positive displacement pumps can handle highly concentrated slurry and provide a quasi-constant flow rate at different pumping pressures [58].

Rotary pumps, specific type of displacement pump, are widely used for slurry transfer in process plant applications [58]. Specifically, for the rotary lobe pump used in the vertical pipe loop, slurry enters into inlet of pump and is drawn into the gaps formed between the rotors and the rotor casing. A pocket of fluid moves with the rotor of pump in both the clockwise and counter-clockwise direction. Rotary lobe pumps generally develop pulsation of lower intensity compared to other positive displacement pumps as they do not have any inlet and outlet valves [58]. The rotary slurry pump selected for this study was supposedly able to handle 3 mm particles in corrosive and concentrated slurry. Details of the pump and its specifications have already been discussed in Section 4.2.

Due to all above mentioned reasons, the rotary lobe pump was selected for the RIM vertical loop.

#### 4.6.2 Discussion on pump performance

For this slurry pump, the pump performance curve was provided by the manufacturer. Furthermore, the pump specification sheet [69] discusses power requirements at different pump speeds. After the commissioning of the RIM rig, the loop was again charged with single phase water. A variable frequency drive was used to change the pump speed. The measured loop operating flow rate was recorded for each pump speed.

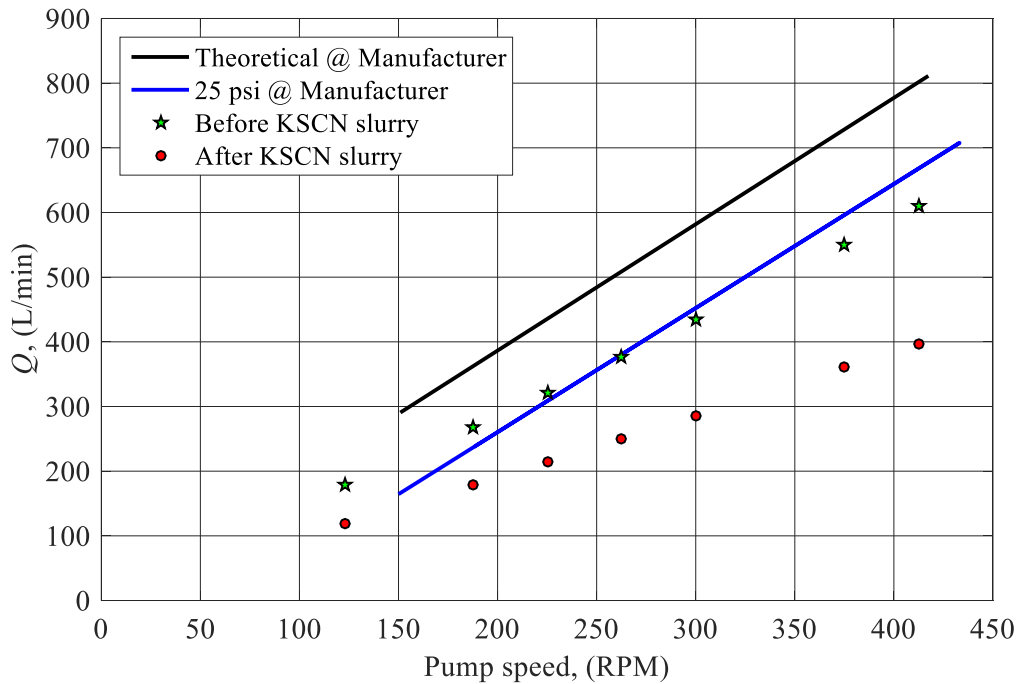


Figure 4.10 : Pump performance for water before and after running a set of experiments with 3 mm size RIM slurry

Figure 4.10 shows the pump performance provided by the manufacturer for a zero and 25 psi pressure differential between the pump inlet and outlet. It depicts that the flow rate changes with pump speed in linear manner. Pressure line of 25 psi is found to be below the theoretical curve or differential pressure line of 0 psi since theoretical curve is based on assumption of zero slip. Slip is defined as difference between theoretical discharge and actual discharge. For a particular fluid, slip is proportional to the pressure differential from discharge to suction. The actual flow rate is lower than the theoretical flow rate as shown in Figure 4.10 because of the slip phenomena.

Figure 4.10 shows a performance curve measured for water before adding KSCN slurry into the loop that shows that the loop was not operated at a constant differential pump pressure. At higher flow rates, the differential was greater than 25 psi because of higher friction losses. The measured and manufacturer performance curves were quite close to each other. Finally, the loop was run with RIM slurry having 3 mm size beads for PIV measurements. After the PIV measurements, the performance of the pump with water was measured again and is displayed in Figure 4.10. The pump performance drastically deteriorated after running the loop for set of PIV experiments with RIM solution. It was quite surprising to note that the flow rate reduced by 34 % from its previous value for the same pump speed. Additionally, excessive pump vibrations were noticed in pump.

#### **4.6.3 Pump incompatibility for vertical loop**

RIM slurry consisting of aqueous KSCN solution and 3 mm size borosilicate beads was charged into the loop for PIV measurements. During the PIV measurements,

the pump performance deteriorated by 34 % as mentioned earlier. Used beads were collected into the screen and cleaned after completion of experiments.

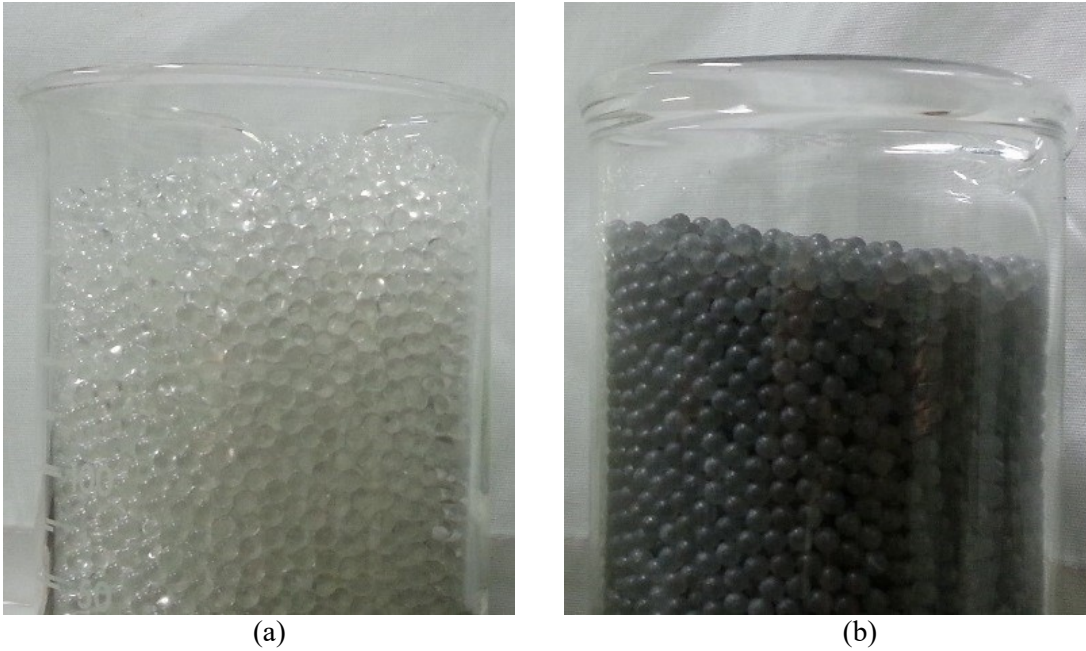


Figure 4.11: (a) New and (b) Scratched/damaged 3 mm size Borosilicate beads

Figure 4.11 illustrates samples collected from the new and used 3 mm Borosilicate beads. It is clear that the used beads had scratch marks on them. New beads are transparent while damaged beads lose their transparency as displayed in Figure 4.11. However, there was no breakage of slurry particles. The reason could be that the lobe was rubbing against 3 mm particles and somehow scratched them.



(a) (b) (c)  
Figure 4.12: Upstream transparent section of loop (a) before adding particles (b) after adding particles into loop (c) fine and coarse residue of lobe from rotary pump

During the time when the pump performance deteriorated, one more interesting phenomenon occurred. Figure 4.12(a) and (b) display upstream transparent section of the loop before and after adding RIM slurry. It was quite surprising that the slurry got completely black after it ran for 15-20 minutes in the loop. Figure 4.12(c) shows a close up photograph of the solution containing coarse particles and residue coming from the lobe pump. It is believed that this residue coming from lobe made the slurry completely black.

Within a couple of hours of loop operation, the solution became black and the particles were scratched. To understand whether PIV and RIM will work in the large scale vertical loop under these conditions, small scale test tube experiments were conducted.

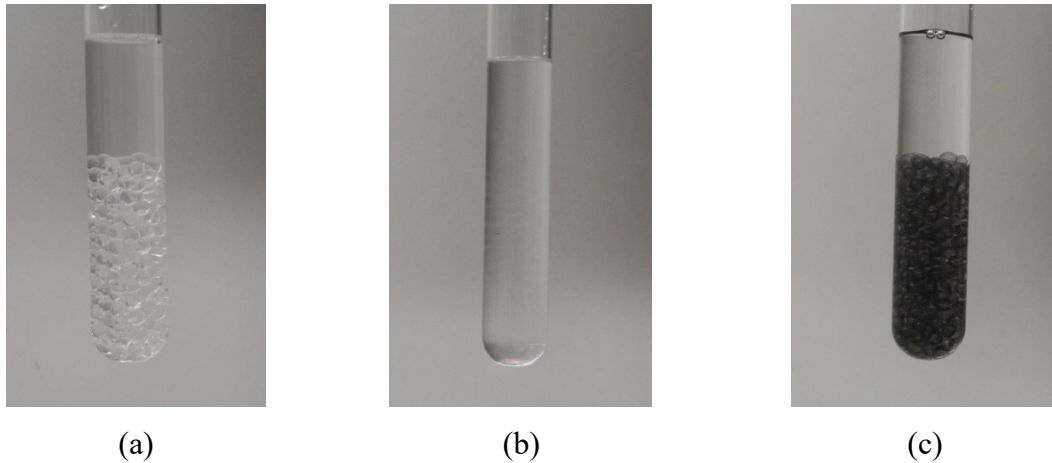


Figure 4.13: New Borosilicate beads in (a) DI Water (b) RIM solution and (c) damaged beads in RIM solution

Figure 4.13(a) and (b) compare DI water with KSCN solution having Borosilicate beads into it. It was observed that the KSCN solution has good index matching with the beads, which is clear since the beads are invisible in the KSCN solution. However, slurry particles are completely visible in DI water due to a large difference between their refractive indices. The difference between new and used beads in the RIM solution in test tube is expressed by Figure 4.13(b) and (c). The new beads are completely invisible in the RIM solution whereas the scratched beads are visible. RIM does not work as the particles are damaged by the pump, and they are no longer transparent in the KSCN solution.

#### ***4.7 Summary and conclusion***

In summary, the following conclusions are made from the large scale vertical loop:

- A large scale vertical flow loop was designed and built uniquely due to the corrosive nature of the slurry
- A standard operating procedure was prepared to handle the abrasive and toxic slurry
- The pressure drop across a fixed length of pipe was measured in the flow loop for a single-phase water flow. It was compared with the calculated pressure loss for water. The results match very well with the calculated values
- During commissioning, the flow rates were measured for single-phase water and two-phase slurry over a certain period of time. Different bead concentrations and bead sizes were used to analyze the flow rate measurements by flow meters. It was concluded that the flow meters work well for single phase. However, they are not compatible with the concentrated slurry
- Pump performance was measured for water before and after running a set of experiments with the RIM slurry. The pump no longer had the same performance for single-phase water flow. The pump performance deteriorated by 34 % for the same pump speed
- Slurry particles were damaged by the lobe of the pump because of abrasive nature of the slurry

- Slurry became completely black after running the loop for several minutes in the vertical loop. It is believed that the black residue came from the pump lobe and made solution totally black
- Finally, new and used beads were added into the aqueous KSCN solution in the test tube. New beads were invisible in RIM solution whereas the damaged beads were visible. In conclusion, PIV and RIM did not work due to the damaged particles and black residue created by pump

## CHAPTER 5: PARTICLE IMAGE VELOCIMETRY IN SOLID-LIQUID FLOWS

This chapter is divided into four different sections. First, the PIV-set up and its configurations are explained in detail. Second, PIV results are presented for single phase flow as part of the commissioning and validation of the PIV system used with the vertical slurry pipe loop. This includes discussions on whether the flow is fully developed and on statistical criteria for the convergence of turbulence measurements. Additionally, the mean and fluctuating velocity profiles for single phase flows are discussed and compared with past publications. Third, raw PIV images are analyzed with and without the application of the refractive-index matching technique. Finally, the flow around a slurry bead relative to bead's own velocity at different radial locations is discussed for concentrated slurry flow.

### *5.1 PIV set-up*

A commercial PIV system (LaVision GmbH) measured axial and radial velocity components on a two-dimensional plane in solid-liquid vertical pipe flow. The typical planar PIV measurement set-up is shown in Figure 5.1. Measurements were carried out in a transparent section at a location  $90D$  above the bottom bend position of the loop in an attempt to ensure a fully developed flow for turbulence measurements. Additionally, the test section was  $18D$  away from long radius upper bend. During PIV measurements, image distortion effect due to circular test section was eliminated using a square view box. The liquid phase was seeded by  $2\ \mu\text{m}$  silver-coated fused silica spheres (SG02S40, Potters Industries Inc.). A 50 mJ double-pulse Nd:YAG laser (Solo III-15z, New Wave)

was used to illuminate the flow, operating at a wavelength of 532 nm. Laser optics converted the laser beam into the thin laser light sheet that illuminated the seeding particles in the area of interest. The laser optics used a combination of cylindrical lenses and a spherical lens. The time delay between laser pulses was adjusted in the range 50 - 120  $\mu\text{s}$  depending on the fluid velocity. All timing signals were controlled and synchronized using a central pulse generator.

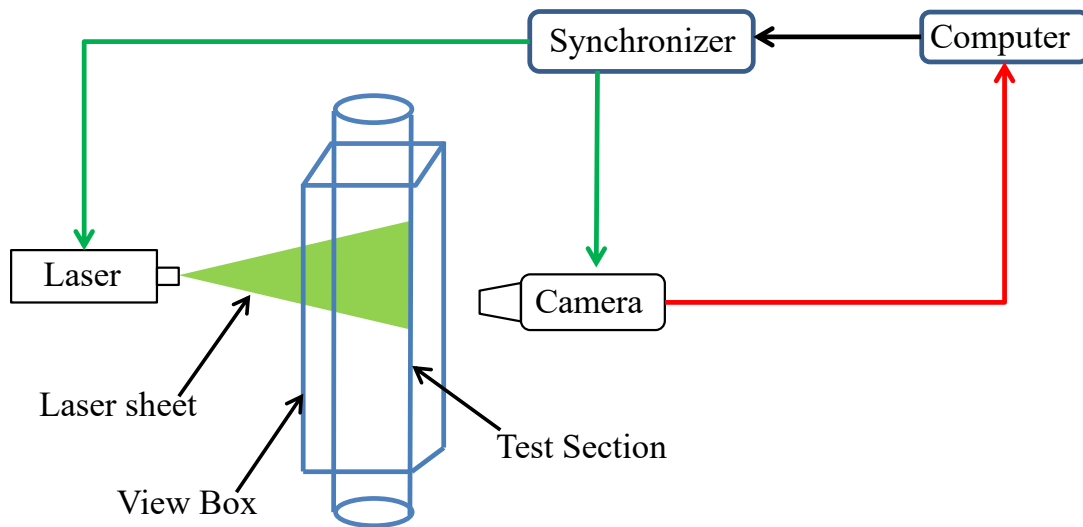


Figure 5.1: Optical PIV measurement system

The light scattered by these particles was recorded on a  $1376 \times 1040$  pixel CCD camera with 12-bit resolution (Imager Intense, LaVision GmbH) having a physical pixel size of  $6.45 \times 6.45 \mu\text{m}$ . The PIV Camera was situated perpendicular to the laser sheet. A 50 mm lens (AF NIKKOR, Nikon) with an aperture setting of  $f/8$  was mounted on PIV camera. The magnification was set in such a way that the spatial resolution was  $0.0384 \text{ mm/pixels}$ . PIV calibration was performed during PIV measurement to convert pixel space to real space and take account of any distortion in the image. For PIV calibration, calibration target having  $5.5 \times 5.5 \text{ cm}^2$  grid patterns with equidistant dot marks

having 0.25 mm diameter and 0.5 mm spacing between was utilized on a flat calibration plate in the light sheet plane for camera calibration. Commercial image processing software (DaVis 8.2, LaVision GmbH) was used for the calibration based on pinhole calibration model [70].

PIV image pairs were captured by running the camera in the double exposure frame-triggering mode with a maximum acquisition frequency of 10 Hz. 5000 statistically independent double-frame PIV images were recorded at 1.7 Hz and processed using commercial software (DaVis 8.2, LaVision GmbH). During PIV pre-processing, raw PIV images were processed to remove any noise to clearly distinguish tracing particles. In PIV post processing, PIV images were processed through a cross-correlation PIV algorithm with two different interrogation window sizes, 75 % window overlap, and two passes. The window sizes were 64×64 pixels and 32×32 pixels in first and second pass, respectively, based on correlation map analysis. The instantaneous velocity field was obtained by processing and collecting 5000 double-frame PIV images in commercial software (DaVis 8.2, LaVision GmbH). Finally, mean and fluctuating axial and radial velocities were calculated by averaging over 5000 instantaneous velocity vector field in commercial software Matlab-2015 (MATLAB-R2015, The Mathworks Inc.).

## ***5.2 PIV in single phase flow***

### **5.2.1 Checking for fully developed flow**

A simple way to check fully developed flow is by measuring the average axial velocity profile at different streamwise locations. Velocity profiles should coincide with

each other for fully developed flow. Measurements were carried out at two different upstream streamwise locations  $85D$  and  $90D$  above the bottom bend position of the loop to determine fully developed flow.

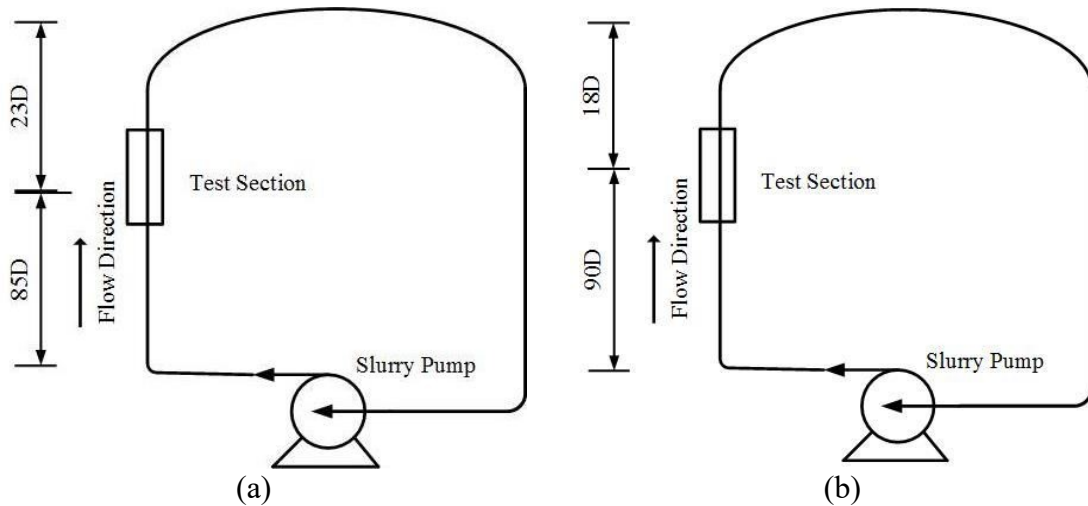
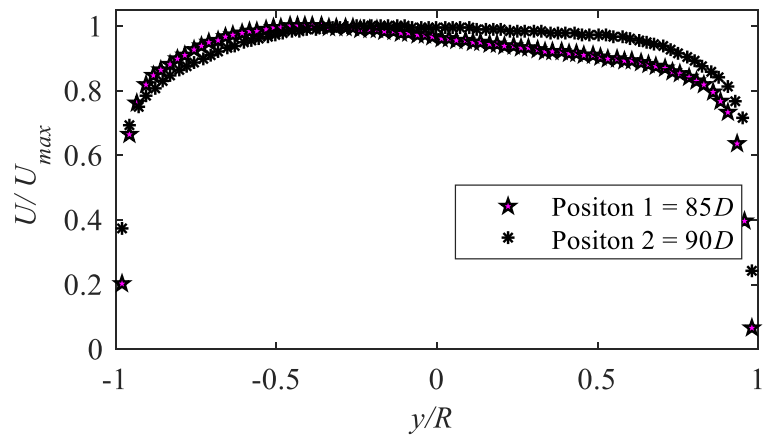
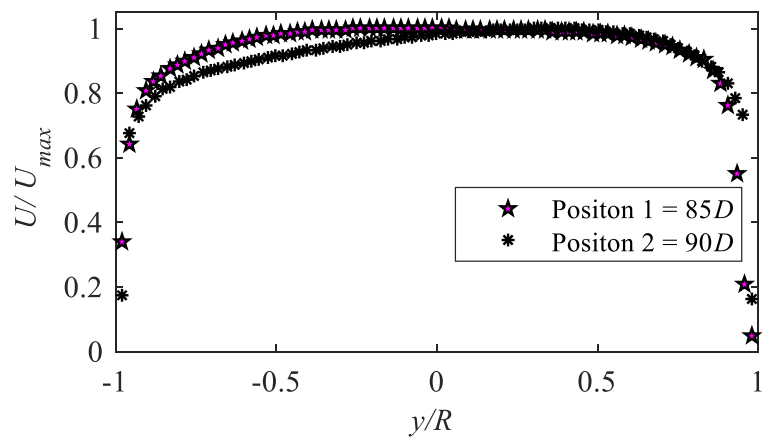


Figure 5.2: PIV measurement streamwise location (a) Position 1:  $85D$  (b) Position 2:  $90D$  above the bottom bend position of the loop

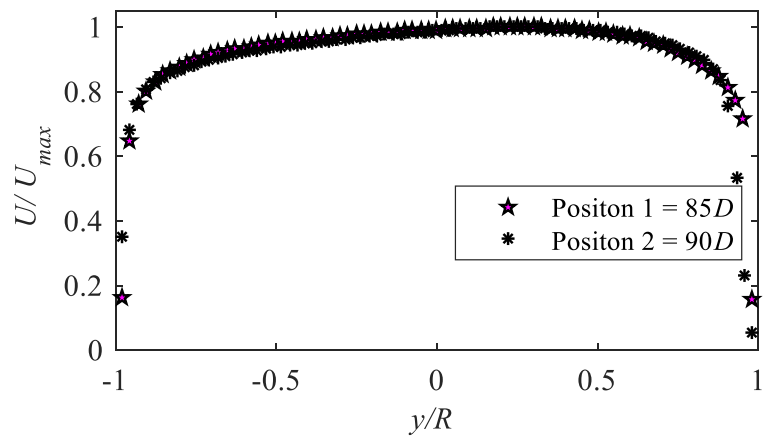
Figure 5.2 shows PIV measurement streamwise location (a) Position 1:  $85D$  (b) Position 2:  $90D$  above the bottom bend position in vertical slurry pipe loop. In other words, position 1 and position 2 are located at  $23D$  and  $18D$  distance away from long radius upper bend in the loop, respectively.



(a)



(b)



(c)

Figure 5.3: Normalized mean velocity profile in streamwise direction at Reynolds number (a) 118 000, (b) 164 000, and (c) 236 000 for two measurement locations

Figure 5.3(a), (b), and (c) shows the mean velocity profiles for Reynolds numbers 118 000, 164 000, and 236 000 at both measurement locations, normalized with maximum mean velocity. On the horizontal axis,  $y/R = 0$ , 1, and -1 denote pipe centerline, pipe right wall, and pipe left wall, respectively. It is clear from Figure 5.3(a) and (b) that the velocity profiles change between the two streamwise positions for Reynolds numbers 118 000, 164 000. However, Figure 5.3(c) suggests that the velocity profile does overlap for  $Re = 236 000$ . Nevertheless, as will be seen shortly from the flow symmetry results, this is more likely to be a coincidence than a sign of fully developed flow. Clearly, the flow profile changes with the streamwise positions, confirming undeveloped flow over this region of test section

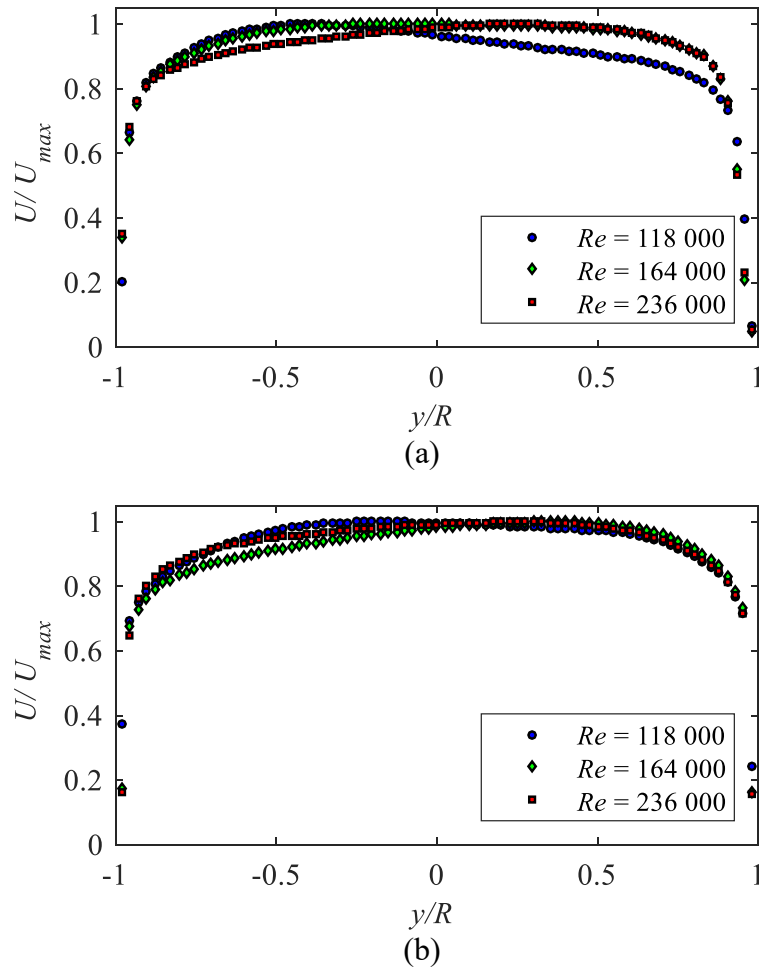


Figure 5.4: Normalized mean axial velocity profile at (a) position 1:  $85D$  (b) position 2:  $90D$  for three different Reynolds numbers

Figure 5.4(a) and (b) displays the average local axial velocity ( $U$ ) normalized with maximum axial velocity ( $U_{max}$ ) at three Reynolds numbers  $Re = 118\ 000$ ,  $164\ 000$ , and  $236\ 000$  for streamwise positions  $85D$  and  $90D$ , respectively. Undeveloped flow further causes asymmetric velocity profile. Asymmetric behavior of velocity profile is observed in Figure 5.4(a) at position 1. For example, the profiles are biased to the right for  $Re = 164\ 000$  and  $236\ 000$  whereas the profile is biased to the left for  $Re = 118\ 000$ . Left and right shifted velocity profiles are also noticed at position 2 for all three Reynolds

number as displayed in Figure 5.4(b). However, the velocity profiles for three Reynolds number coincide better at position 2 than position 1. Velocity profile is biased to right at  $Re = 236\ 000$  for both streamwise locations. However, velocity profile overlaps as a coincidence at two locations. This gives further evidence that the flow is not fully developed.

There might be several reasons behind undeveloped flow in present vertical loop. These include: sharp bottom bend or upper bend in the flow that could be generating swirl flow or secondary flow in the loop; rotary lobe slurry pump that creates unsteadiness in the flow. Unsteadiness in the flow is generated by pulses coming out from the pump.

### **5.2.2 Convergence criteria**

This section discusses convergence criteria for mean and turbulence fluctuation velocity. Convergence tells how many measurements need to be recorded so that the uncertainty in the measured mean and turbulent statistics is lower a certain value. For this reason, in the beginning, 5000 double-frame PIV images were collected.

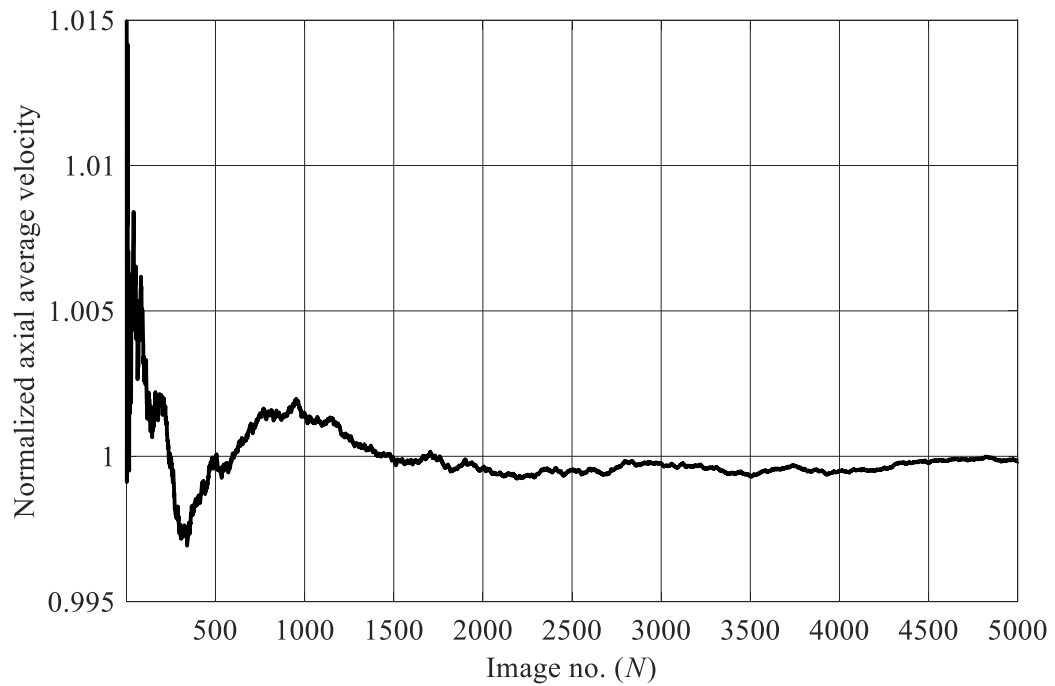


Figure 5.5: Measured mean axial velocity averaged over a finite number of PIV images

Figure 5.5 shows the convergence of the measured mean axial velocity over 5000 PIV double frame images at the centreline of the pipe flow. The mean axial velocity is normalized with long-time average velocity of the 5000 images (4.1 m/s). It is evident from Figure 5.5 that normalized average value converges as image numbers are increased and equal to long-time average velocity.

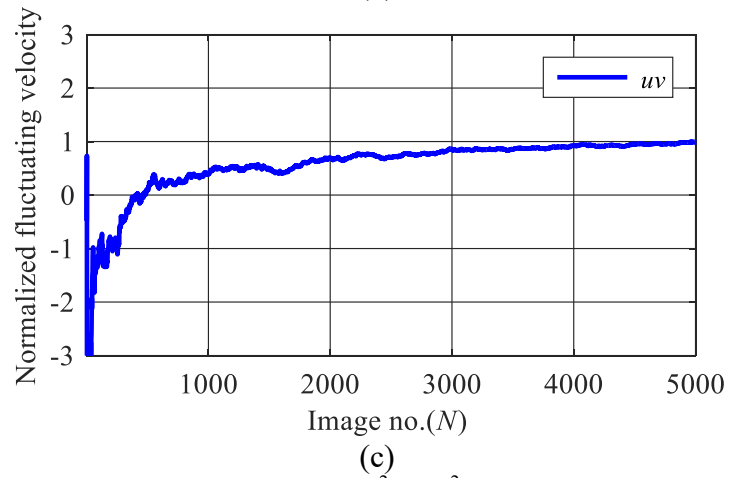
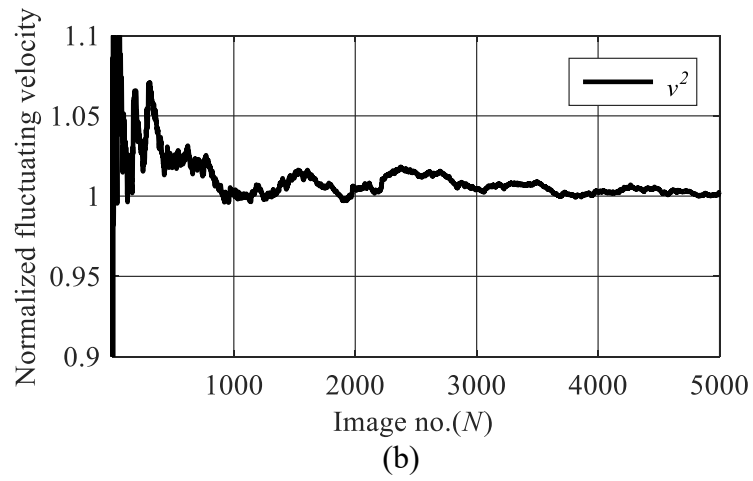
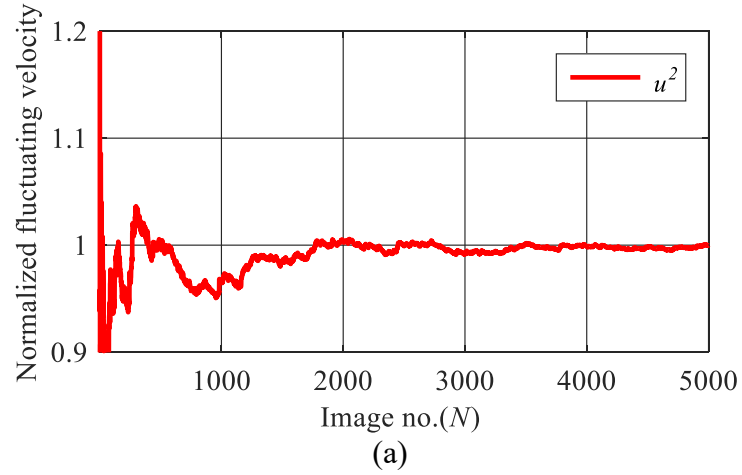


Figure 5.6: Measured fluctuating velocity (a)  $u^2$  (b)  $v^2$  (c)  $uv$  averaged over a finite number of PIV images

Figure 5.6 displays convergence behavior for the measured fluctuating velocities averaged over 5000 PIV images where  $(u, v)$  represents fluctuating velocities in the axial and radial directions, respectively. Turbulent fluctuating velocities are normalized with long-time turbulent fluctuating velocity at centreline of the flow. It is observed from Figure 5.6(a), (b), and (c) that streamwise turbulent fluctuations ( $u^2$ ), radial turbulent fluctuations ( $v^2$ ), and Reynolds shear stress ( $uv$ ) converges around 4000 PIV images. All fluctuating velocities are being statistically converged and have steady value as depicted in Figure 5.6 .

### 5.2.3 Mean velocity profile

Mean axial and radial velocities were calculated by averaging over 5000 instantaneous velocity vector field. Figure 5.7 shows the variation in  $U/U_{max}$  along the radial direction. Here,  $y/R = 0$  and  $y/R = 1, -1$  denote pipe centerline and pipe wall, respectively. Results are obtained for  $V = 3.49$  m/s, which corresponds to  $Re = 198\ 000$ . The results are compared with a experiments results of a turbulent channel flow at  $Re = 189\ 000$  [71].

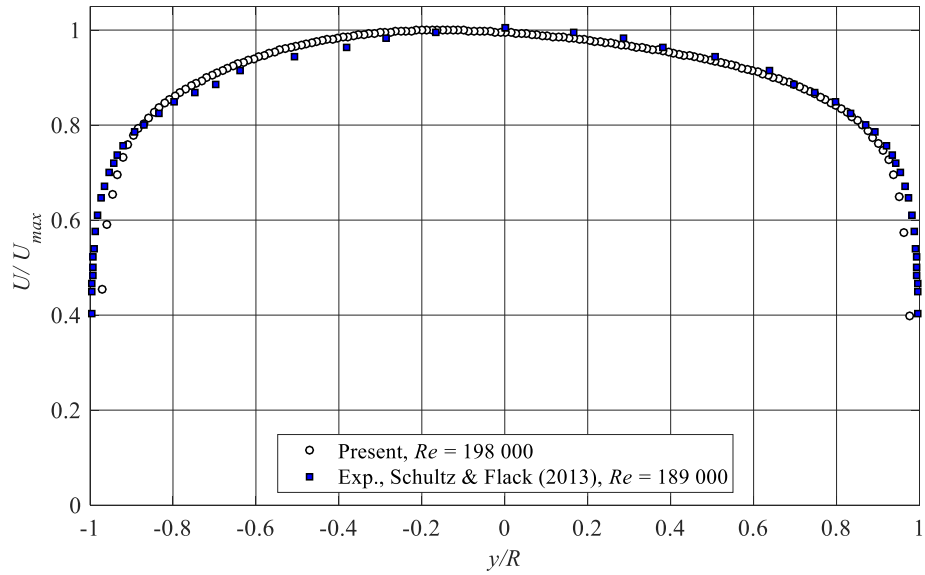


Figure 5.7: Mean streamwise velocity profiles for water at  $Re = 198\,000$

The present results are in reasonable agreement with Schultz and Flack's [71] turbulent channel flow experiments except for the asymmetry discussed earlier. Additionally, there is discrepancy in the results for near-wall measurements. Present study was not focused for near wall measurements whereas Schultz and Flack's [71] experiments dedicated towards near wall measurements.

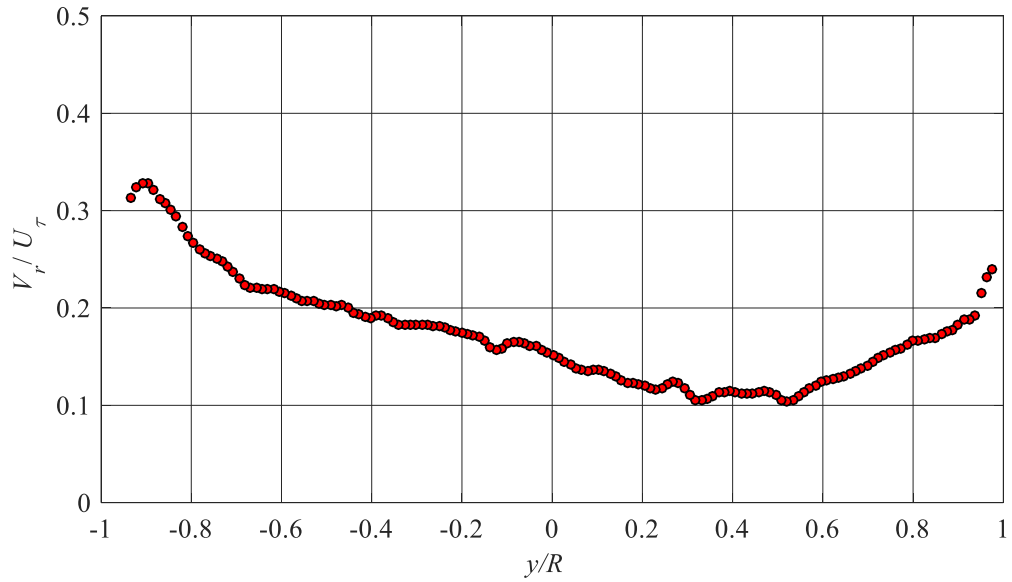


Figure 5.8: Variation in mean radial velocity in cross-streamwise direction.

Figure 5.8 displays mean velocity in cross-streamwise or radial direction for  $Re = 198\,000$ . Mean radial velocity is normalized with friction velocity ( $U_\tau$ ), which is computed by [72]:

$$U_\tau = \sqrt{\frac{\tau_w}{\rho}} \quad (5.1)$$

Friction velocity or shear velocity shows shear stress in term of velocity form to characterize shear stress at pipe wall. In Equation (5.1),  $\rho$  and  $\tau_w$  are fluid density and wall shear stress, respectively. Wall shear stress is given by:

$$\tau_w = \frac{f\rho V^2}{2} \quad (5.2)$$

where  $f$  denotes the Fanning friction factor that is computed using Equation (4.3).

Figure 5.8 illustrates that there is flow in radial direction. Radial flow is relatively low in core region but increases as move along the pipe wall. For a fully developed flow,

there should not be any radial flow. However, there is radial flow in present measurements due to undeveloped flow as discussed earlier.

#### **5.2.4 Turbulence statistics**

Reynolds normal stress in streamwise and radial direction and Reynolds shear stress velocity profiles for water at  $Re = 198\ 000$  were measured. Results are compared with Schultz and Flack [71] for turbulent channel flow.

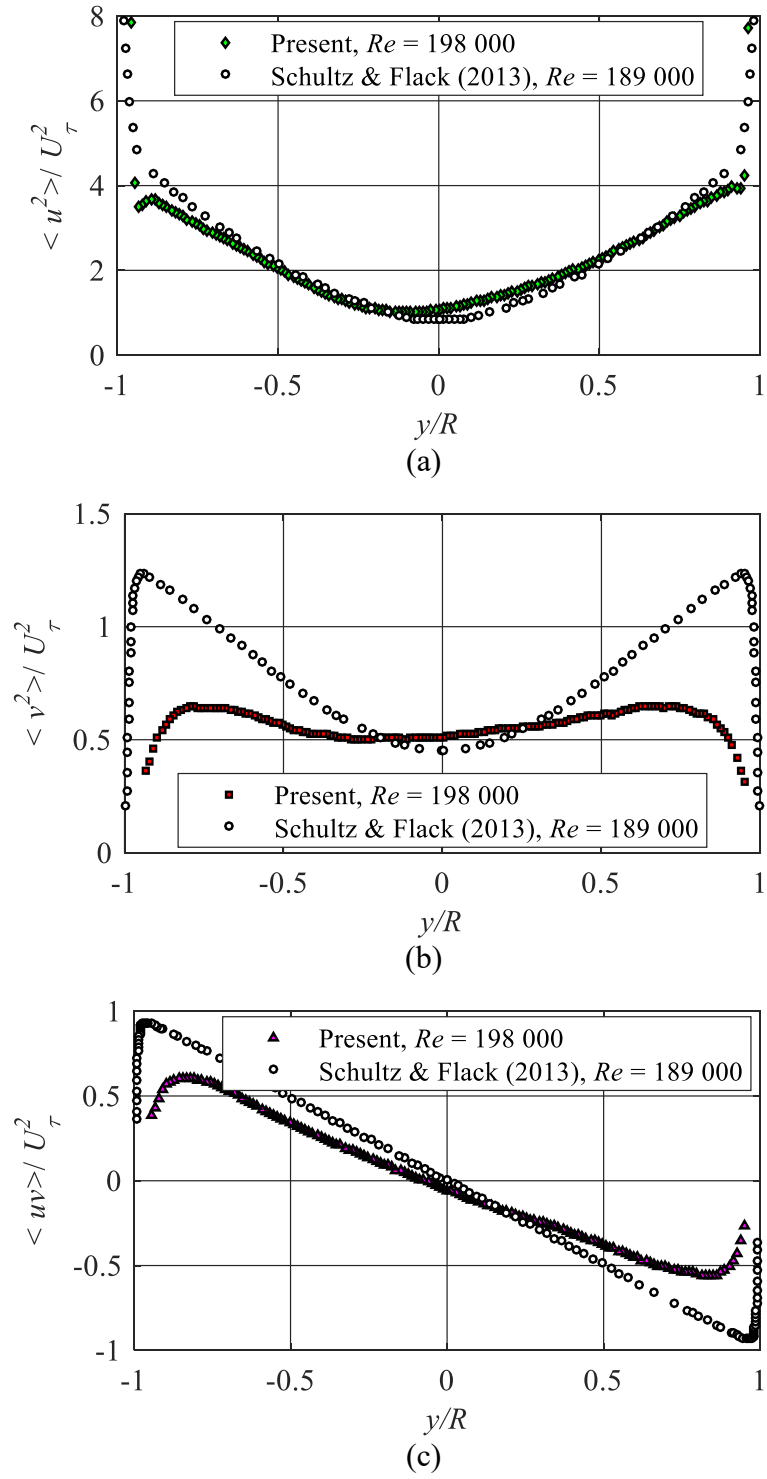


Figure 5.9 (a) Streamwise Reynolds normal stress (b) Radial Reynolds normal stress (c) Reynolds shear stress velocity profiles for single phase water

Figure 5.9 (a), (b), and (c) displays streamwise Reynolds normal stress ( $\langle u^2 \rangle$ ), radial Reynolds normal stress ( $\langle v^2 \rangle$ ), and Reynolds shear stress ( $\langle uv \rangle$ ) velocity profiles for water at  $Re = 198\,000$  in comparison with Schultz and Flack [71] for turbulent channel flow. All results are normalized by friction velocity ( $U_\tau$ ). It is evident from Figure 5.9 (a) that streamwise Reynolds normal stress profile is in good agreement with Schultz and Flack [71]. However, the minimum value of streamwise velocity fluctuation is offset slightly from the pipe centre, consistent with the flow asymmetry discussed already. The maximum streamwise Reynolds normal stress value is quite similar in present and Schultz and Flack [71] experiments. Figure 5.9 (b) shows radial Reynolds normal stress that is asymmetric and left shifted along the centreline of the flow. In present measurement, maximum value of radial Reynolds normal stress reaches a value of  $\sim 0.65$ , whereas this value is  $\sim 1.25$  in Schultz and Flack [71] measurements. Undeveloped flow might be reason of discrepancy in present measurements. Reynolds shear stress velocity profiles are shown in Figure 5.9 (c). The Reynolds shear stress line has linear behavior in the core region of flow for both the studies. In the present study,  $\langle uv \rangle$  stress is not zero at centreline of the flow since profile is slightly left shifted. However, Reynolds shear stress should be zero at centreline of the pipe. Maximum value of Reynolds shear stress is  $\sim 0.6$  in present study whereas  $\sim 0.9$  in past study. There is a discrepancy due to difference in their radial turbulent fluctuations profile that impacts in Reynolds shear stress data as well. The turbulence statistics results, especially the radial component do not match with past publication due to undeveloped flow and existence of average radial flow.

### ***5.3 PIV in solid-liquid flow***

This section examines sample PIV images obtained in the vertical flow loop with and without RIM for concentrated slurry flow. The problems associated with PIV images without RIM are described. Additionally, general features of PIV image with RIM are described. Finally, the impact of the pump failure on the PIV measurements is discussed.

#### **5.3.1 PIV without RIM**

A typical PIV image obtained in the vertical flow loop without the application of RIM is shown in Figure 5.10. The PIV image was obtained for 5 % volumetric concentrated slurry with a 12-bit PIV camera. The slurry consisted of water and glass beads as the continuous and dispersed phase, respectively. The general problems associated with PIV in slurry flow are clear from Figure 5.10. Once a bead comes into the laser sheet, it blocks the light. In the bead's shadow, the seeding particles are not illuminated. There are also several dark regions where no seeding particles are detected. The solid-liquid interfaces cause excessive light scattering and flare from the beads, leading to blooming or light glow, and image saturation denoted by the red regions in the image. Non uniform distribution of light through a phase boundary is also noticed due to refraction and reflection.

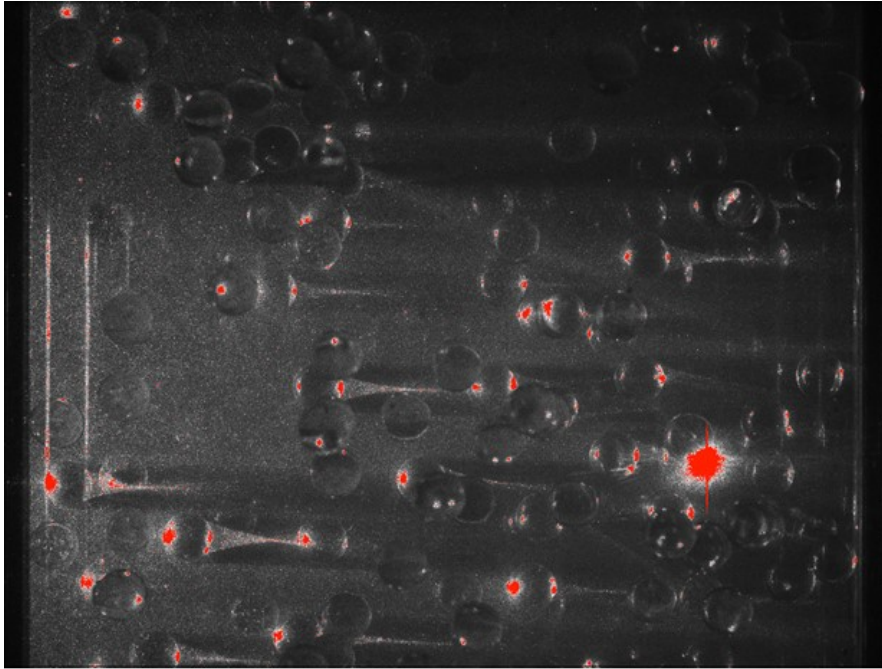


Figure 5.10: Raw PIV images for concentrated non-RIM slurry

The slurry particles between the laser sheet and the camera also block the light, hiding flow regions. Background noise is distributed unevenly in the images. All these areas, especially far from the pipe wall, in the PIV image do not provide any meaningful information about the fluid flow. Finally, a mirror effect at solid-liquid interface creates ghost images which appear to be inside the solid beads. Due to all of the above mentioned reasons, it is difficult to find significant PIV correlation for PIV computation even with the application of different filters during PIV pre-processing.

### **5.3.2 PIV with RIM**

The problems associated with the solid-liquid interface in PIV are overcome using refractive index matching method. Figure 5.11 illustrates a typical PIV image for 5% v/v

concentrated RIM slurry. RIM slurry consisted of 62.4 % KSCN solution as continuous phase and 3 mm size borosilicate glass beads as the dispersed phase.

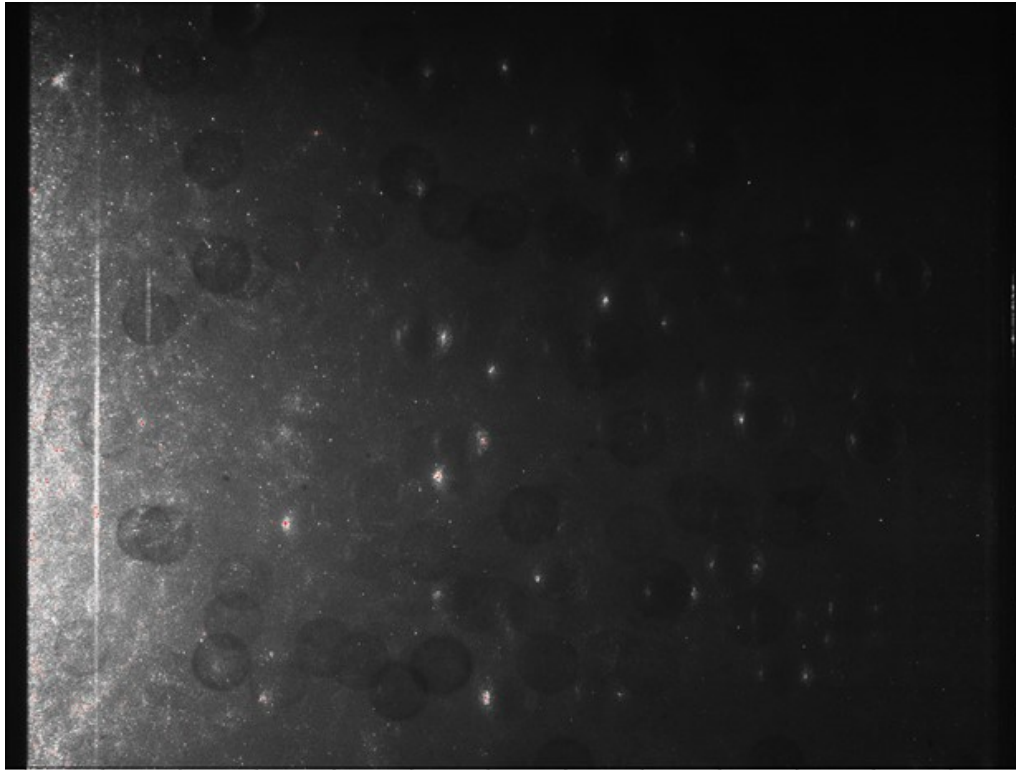


Figure 5.11: Raw PIV image for concentrated RIM slurry

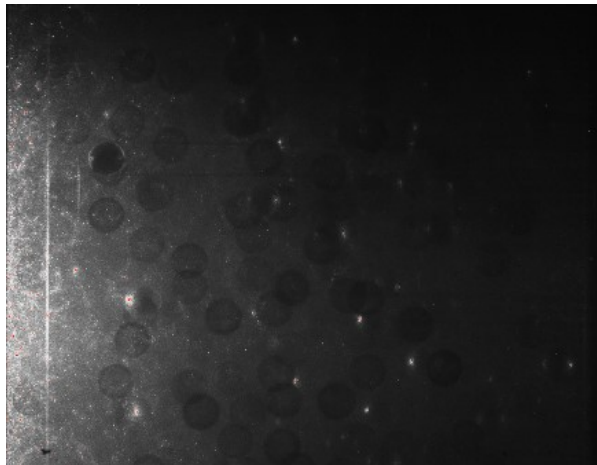
The PIV image clearly shows a significant reduction in light flaring and light scattering from solid-liquid phase boundary. The RIM technique helps to eliminate shadows casted by slurry particles. The PIV image has more visible seeding particles, making it possible to measure the continuous phase velocity since the beads do not block laser sheet light. There are enough seeding particles behind the particle to capture flow around them. It is also possible to see through the slurry beads to capture displacement of the seeding particles. However, there are still significant challenges in the processing of these PIV images. Edge of the solid boundary is quite indistinct in most of the region but noticed in some region of the image. Light is not evenly distributed in the image. The

front region from where laser sheet enters into the test section has more light. The light intensity decreases significantly in the radial direction. The background noise also is in non-uniform nature that further creates difficulty while processing such images. Furthermore, bead shadows and remaining glare in the image are result of imperfect RIM.

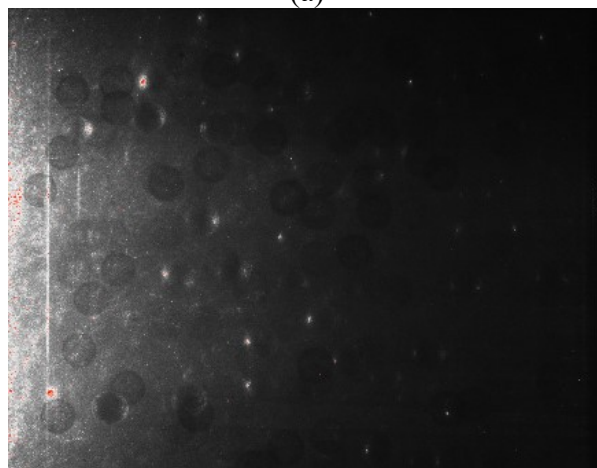
The present RIM image shows some general characteristics/features that are useful to study two-phase flows with combined application of PIV and RIM. However, other features as shown in RIM image are result of experimental issues unique to the existing PIV dataset due to the pump failure during measurements.

### **5.3.3 Pump incompatibility during measurement**

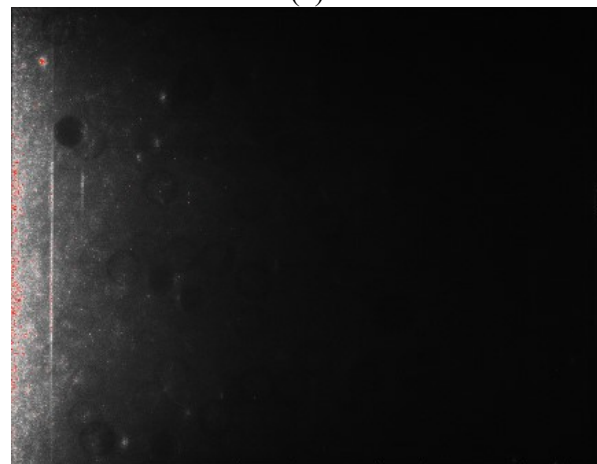
This section emphasizes the impact of the pump failure on the PIV measurements during the application of RIM technique. The pump incompatibility for the present vertical loop was discussed in Section 4.6.3 in detail.



(a)



(b)



(c)

Figure 5.12: PIV image number (a) 100 (b) 1000 (c) 5000 collected using RIM technique for 5 % concentrated RIM slurry

Figure 5.12 shows PIV raw image number (a) 100, (b) 1000 and (c) 5000 collected using RIM technique at vertical slurry loop for 5 % concentrated RIM slurry. It is observed from Figure 5.12 that light intensity significantly reduces with increase in image number from 100 to 5000 due to the black residue, which entered into the flow from lobe of the pump. For example, image number 5000 is almost completely black and cannot be considered for PIV analysis. The pump failure also causes the strong reduction in light intensity from the left of the image to the right of image. Deterioration in lobe of the pump is mainly due to abrasiveness of beads and corrosiveness of carrier fluid KSCN solution. Black residue started to come off from the deteriorated lobe in the pump. Black residue entered into the fluid flow and made the fluid completely dark black. Decoloured black fluid reduced light intensity in the image significantly within half an hour of experiments. In conclusion, slurry pump could not able handle presently used abrasive and corrosive slurry mixture at vertical loop.

During the loop operation, particles were damaged and scratched by the lobe pump. Damaged beads lost their transparency while new slurry beads were completely transparent. Hence, scratched beads were more visible in the RIM solution while the new beads were nearly invisible in the RIM solution as discussed in Section 4.6.3. That could be the reason why the edge boundary between solid and liquid was noticed more for some beads. Imperfect refractive index matching could be reason behind bead shadows in the RIM image as displayed in Figure 5.12. Refractive index matched tuning could not be possible to have perfect RIM mixture due to pump failure.

Several attempts were made and the manufacturer's recommendations were considered to improve the system. However, the pump incompatibility issue could not be

resolved. Finally, manufacturer confirmed that present rotary slurry pump is not well-suited with RIM slurry. Due to the pump failure, there is no PIV data available for two-phase flow. Unfortunately, this means that an investigation into turbulence modulation with these results is not currently possible. However, PIV results show major challenges dealing with large scale RIM loop for turbulence measurements.

#### ***5.4 Flow around a slurry particle***

This section discusses flow around a slurry particle at different radial locations for concentrated solid-liquid flow. These results are based on the non-RIM images described above. In-focus beads are considered for analysis at different radial locations. Care was taken to ensure that for the selected images, area around the slurry beads are not significantly influenced by other beads so that PIV is done for unobstructed surrounding fluid. A graphical custom made user interface for bead masking [73] developed in Matlab-2015 (MATLAB-R2015, The Mathworks Inc.) was used to locate the bead position precisely and to identify an area of interest for the PIV computation. The area of interest in PIV image was processed through a cross-correlation PIV algorithm with window size of  $32 \times 32$  pixel<sup>2</sup> with window overlap of 50 % and 2 passes.

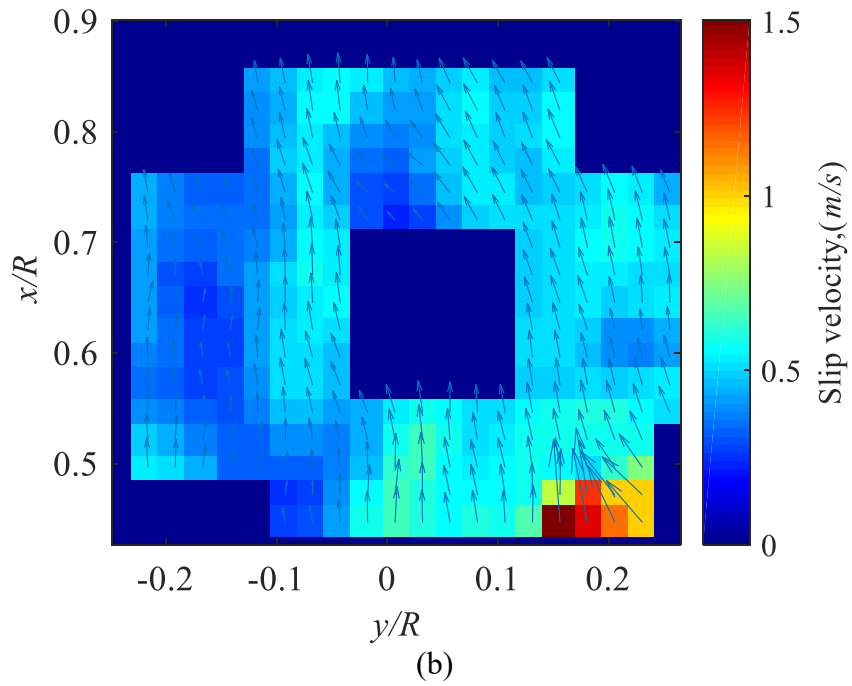
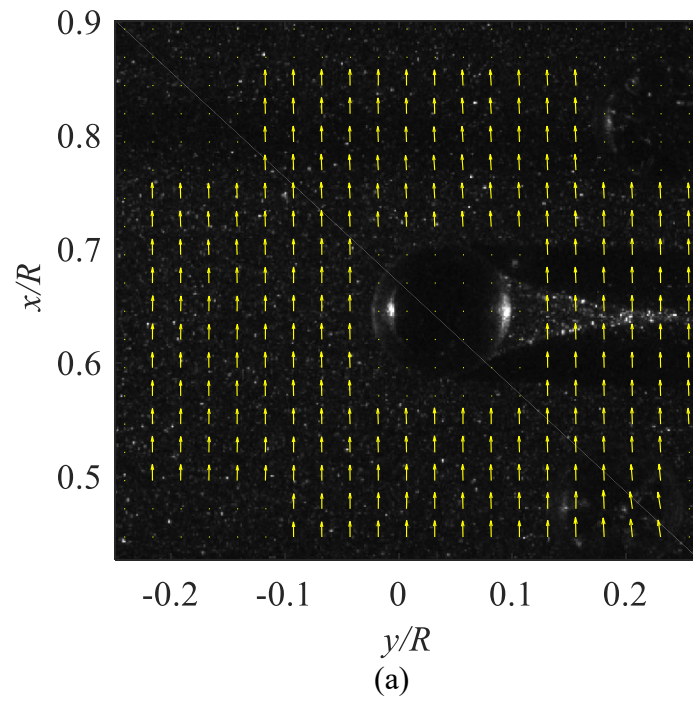
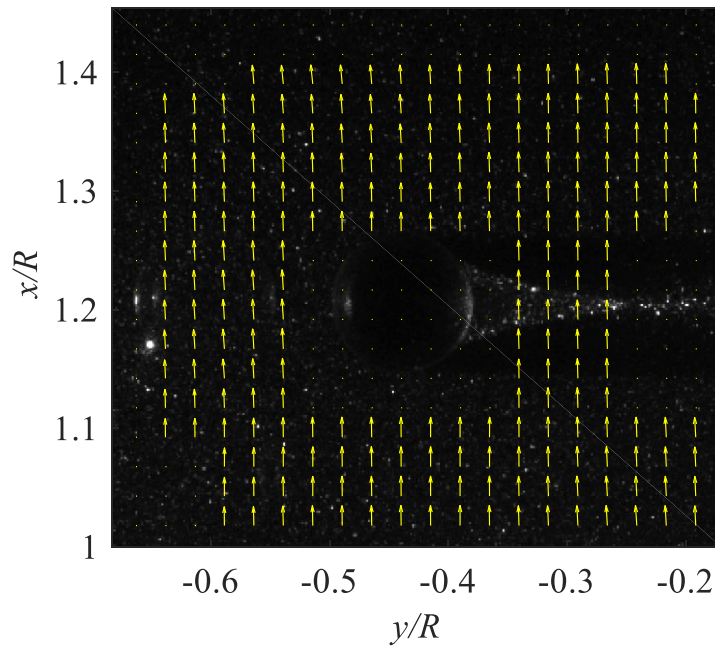
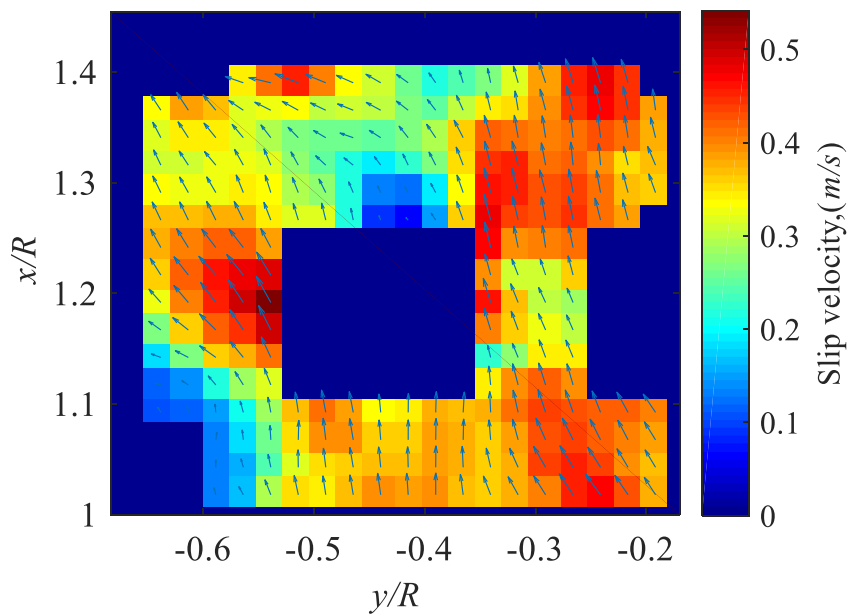


Figure 5.13: (a) Flow field around a bead in Eulerian reference frame (b) flow field around a bead relative to its own velocity in Lagrangian reference frame at bead centre radial location  $y/R = 0.09$



(a)



(b)

Figure 5.14: (a) Flow field around a bead in Eulerian reference (b) flow field around a bead relative to its own velocity in Lagrangian reference at bead centre radial location  $y/R = -0.43$

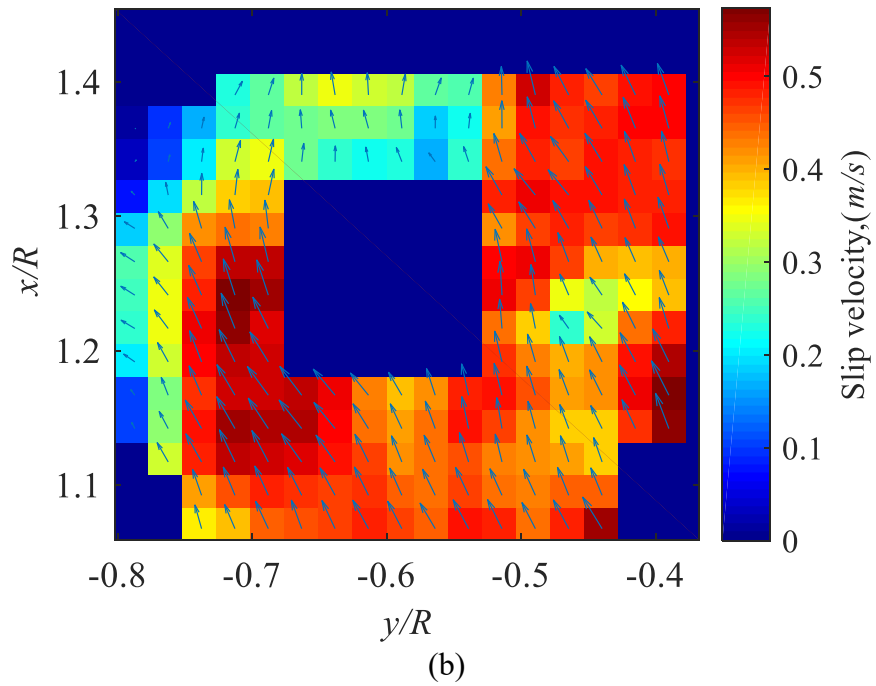
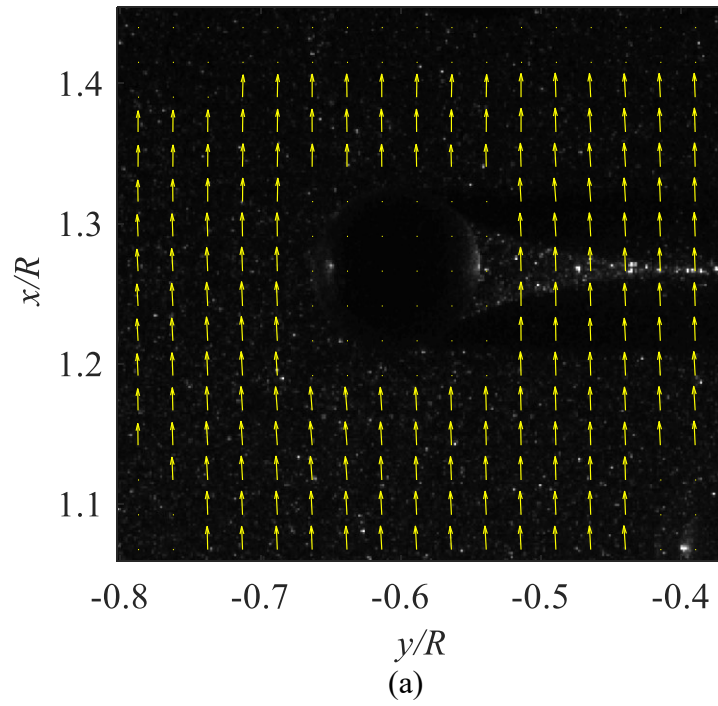


Figure 5.15: (a) Flow field around a slurry bead in Eulerian reference (b) flow field around a bead relative to its own velocity in Lagrangian reference at bead centre radial location  $y/R = -0.61$

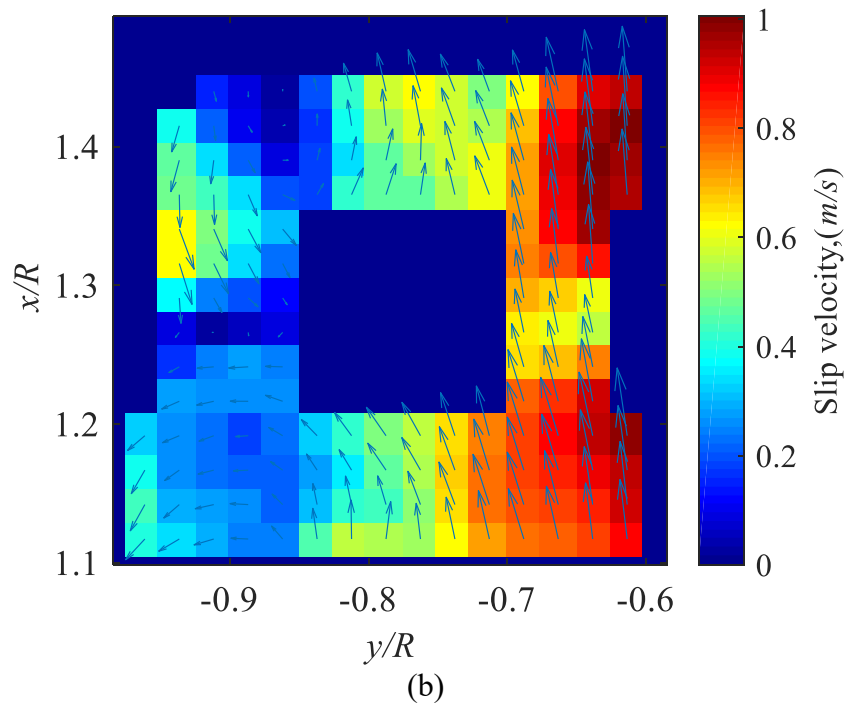
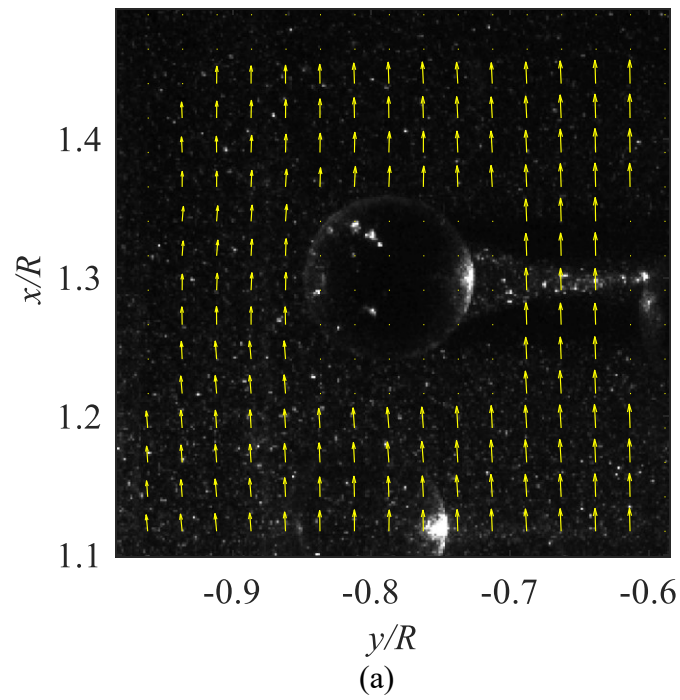


Figure 5.16: (a) Flow field around a bead in Eulerian reference (b) flow field around a bead relative to its own velocity in Lagrangian reference at bead centre radial location  $y/R = -0.80$

Figure 5.13-Figure 5.16(a) shows the flow around the bead with the background raw PIV image as the background at different bead centre location  $y/R = 0.09, -0.43, -0.61,$  and  $-0.80$ . In the figures,  $y/R = 0$  and  $y/R = 1, -1$  denote pipe centerline and pipe left wall and right wall, respectively and  $x/R$  denotes normalized stream-wise direction. Flow around the bead in the Eulerian reference frame in Figure 5.13-Figure 5.16 (a) in each figure, illustrates overall flow around a particle is going in upward direction for all radial locations. Figure 5.13-Figure 5.16(b) shows the vector flow field around the slurry bead relative to the bead's own velocity at different radial locations in Lagrangian reference frame. Background in the vector flow field displays magnitude of fluid velocity relative to bead velocity, also called slip velocity. Flow field in Figure 5.13-Figure 5.16(b) corresponds to beads centre location at  $y/R = 0.09, -0.43, -0.61,$  and  $-0.80,$  respectively.

It is also evident from Figure 5.13-Figure 5.16(b) that flow around the bead is in upward direction, reflecting the positive slip velocity observed at different radial locations in Lagrangian reference frame. At a couple of the radial locations, flow seems to be left biased with some radial flow due to undeveloped flow discussed earlier. However, Figure 5.16(b) displays negative slip velocity or fluid velocity lower relative to bead velocity near to pipe wall. Some of the vectors depicting downward direction in Figure 5.16(b) show that beads move relatively faster than fluid velocity in near wall region in Lagrangian reference frame. Figure 5.13-Figure 5.16(a), (b) do not have same vector scaling of the velocity field.

Additionally, slip velocity was also calculated near to centreline of flow ( $y/R = 0.09$ ). Slip velocity is estimated by calculating the relative velocity between the

fluid and the solid bead. To calculate slip velocity, first, the mean fluid velocity was calculated by averaging all the vectors around the bead in the area of interest shown in Figure 5.13(a). Second, displacement of the bead was measured to calculate bead velocity in a short time period of  $120\ \mu\text{s}$  between two PIV frames using earlier discussed MATLAB graphical custom made user interface algorithm [73]. The calculated slip velocity was 0.16 m/s. The positive slip velocity shows that the particle moves slower than fluid which agrees with the vector field shown in Figure 5.13(b).

It is also common to assume that the single spherical particle based terminal settling velocity can be considered as good approximation for the slip velocity [67]. The slip velocity and theoretical terminal settling velocity was compared all together. The terminal settling velocity of 3 mm size bead is 0.36 m/s as calculation shown in section 4.5.2, which is close to but greater than the slip velocity. However, this slip velocity is calculated based on only a single PIV snapshot and can only be used for a qualitative comparison.

## ***5.5 Summary and conclusion***

The PIV setup was discussed for turbulence measurement in a large-scale vertical slurry flow pipe loop. Mean and turbulent velocity profiles for single phase (water) are presented to validate the PIV system. The mean axial velocity was measured at different streamwise location and various Reynolds numbers for single phase flow. The change in velocity profile with axial position and the asymmetric flow profiles show that the flow is not fully developed. Possible reasons behind undeveloped flow could be the sharp lower bend creating secondary flow or unsteadiness flow due to pulsation coming out from

pump itself. Mean axial and radial velocity profiles are measured and compared with past literature. Streamwise Reynolds normal stress results are in good agreement with published results. However, there is large discrepancy between present and past available radial Reynolds normal stress at  $Re = 198\ 000$ . This is likely due to overall mean radial flow occurring in radial direction. The differences in the radial fluctuations further impact results of Reynolds shear stress.

The problems associated with PIV images obtained in the vertical flow loop without refractive-index matching are discussed for concentrated solid-liquid flow. The RIM technique helps reducing light scattering and flare at solid-liquid interfaces. Important characteristics of PIV image with application of RIM techniques are identified. The effect of the pump failure was discussed along with its impact on the PIV measurements. Investigation of turbulence modulation in concentrated slurry flow could not be analyzed due to the pump failure. Lastly, velocity field showing the flow around a slurry bead relative to its own velocity at different radial locations are studied for concentrated solid-liquid flow in Eulerian and Lagrangian reference frame. Snapshots of the flow around a slurry bead in a Lagrangian reference frame shows net relative movement in upward direction, reflecting the positive slip velocity observed at different radial locations except in near wall region.

## CHAPTER 6: CONCLUSIONS AND RECOMMENDATIONS

### 6.1 Conclusions

Three different types of experimental methodologies are presented for bench scale refractive index matching. These include: refractometer experiments, reflectance measurements, and refractive index matching with solid-liquid mixture. Refractometer was used to measure refractive indices of aqueous KSCN solutions for wide range of concentration  $c = 0 - 70.5\%$  (up to solubility limit at room temperature) and temperature range of  $T = 20 - 40\text{ }^{\circ}\text{C}$ , quantitatively. It was found that KSCN refractive index increases with concentration in quadratic manner for all solution temperatures. Additionally, refractive index does not change significantly with variation in temperature, showing less temperature sensitivity. An empirical model is provided for KSCN refractive index as function of temperature and concentration. Additionally, concentration and temperature sensitivity on refractive index is compared between KSCN solution and commonly used NaI solution. It was found that both solutions do not change significantly with variation in temperature. However, concentration gradient of KSCN solution is three times less than the popular index matched fluid NaI solution. It makes KSCN solution to be relatively better index matched fluid while tuning the concentration for index matching to predict perfect index matching point.

In reflectance measurements, scattered light from solid object is measured for different concentration of KSCN solution to account for the reflection and refraction from solid object in solid-liquid flows. It was observed that signal intensity or reflected light

from solid object decreases considerably with increase in KSCN solution refractive index. Results are compared with Fresnel equations of reflectance. Lastly, refractive index matching is performed with a packed bed solid-liquid mixture by capturing the calibration target dot images for different KSCN concentration in a beaker. It was noted that 62.4 % KSCN concentration is point of perfect refractive index matching in the case of borsolicates glass beads. At this concentration, beads were completely invisible in KSCN solution. Bench scale refractive index matching gives understanding about refractive index of KSCN solution quantitatively and qualitatively to implement RIM technique in combination with PIV at large scale vertical loop.

After bench scale refractive index matching, a large scale vertical flow loop was designed for refractive index matched measurements in turbulent concentrated solid-liquid flows. Loop was able to handle corrosive, toxic, and abrasive nature of concentrated slurry for wide range of Reynolds number. A detailed standard operating procedure was prepared to handle the abrasive and toxic slurry from safety point of view that had not been done before. Present loop design and operation was fairly different than other vertical loop used by previous researcher for slurry application due to toxic and corrosive nature of the slurry.

During commissioning, pressure drop was measured and compared across a fixed length of pipe for water with calculated pressure loss. Flow rates were also measured from magnetic flow meter for single phase and two-phase flow having different bead size and concentration at different pump speeds over a large time period. It was observed that flow meter does work for single phase flow. However, flow meter reading was not steady for concentrated slurry. It was concluded that either flow meter was not compatible with

concentrated slurry or present slurry pump created huge fluctuations in flow rate measurements.

Before and after running a set of experiments with the RIM slurry (KSCN solution + borosilicate bead), pump performance was measured for single phase water. It was noticed that pump performance deteriorated by 34 % for same pump speed for water. Additionally, slurry beads were damaged by the lobe of the pump that made beads visible in RIM solution. Black residue coming out from the lobe made the fluid completely dark black.

In the course of commissioning, the PIV set-up was also commissioned for turbulence measurement of the solid-liquid slurry flow in large-scale vertical pipe loop. During commissioning, mean and turbulent velocity profiles for single phase (water) were measured to validate the PIV system. To check the fully developed flow, mean axial velocity was measured at different streamwise locations and various Reynolds number. Mean axial velocity profiles did not overlap at altered streamwise locations. Additionally, velocity profile was either right or left biased by changing the Reynolds number. It means that profile was not symmetric due to undeveloped flow in region of test section. It was argued that undeveloped flow could be due to sharp lower bend or unsteady flow generated by the slurry pump.

Particle image velocimetry and its associated challenges are discussed without the application of refractive index matching in concentrated slurry flow at vertical loop. It was observed that PIV computation cannot be possible for turbulence study due to difficulties associated with PIV system in solid-liquid flow such as light scattering, shadow regions, and excessive light flare from solid-liquid interfaces. All these problems

are fixed by matching the refractive index of solid and liquid to eliminate solid-liquid interfaces. Refractive index matching technique is implemented in combination with PIV for concentrated suspensions for flow visualization. Important features of PIV image with RIM such as less light scattering, no shadow region etc. were discussed. However, significantly reduction in light intensity with increase in image number was noticed due to the black residue, which entered into the flow from the lobe of the pump. Effect of pump incompatibility on PIV measurements were discussed in detail. This project further focuses on many of challenges such as slurry pump failure, undeveloped flow etc. involved with large scale vertical loop for RIM suspensions and related data analysis.

Lastly, flow around a slurry bead in concentrated solid-liquid flow is studied for non-RIM slurry at different radial locations in vertical pipe loop. It was observed that vector field, showing flow around a bead relative to its own velocity were in upward directions in core region of the flow. It depicted positive slip occurring in the flow, suggesting fluid moving faster than beads. However, negative slip velocity was observed in near wall region displaying bead velocity higher than fluid velocity in that region.

In conclusion, key contributions from present study are:

- Evaluation of concentration and temperature effects on refractive index of KSCN solutions
- Comparative study of refractive index of KSCN and commonly used NaI solution for concentration and temperature sensitivity analysis
- Development of a larger-scale KSCN flow system to handle corrosive, abrasives and toxic nature of slurry

- The problems such as undeveloped flow, flow meter incompatibility, and pump failure encountered were problems anyone would face and thus are generally valuable (i.e. not limited only to the present study)

## ***6.2 Recommendations***

The primary objective of the present study about turbulence modulation measurement for concentrated slurry flow could not be achieved due to pump failure. In the future, the main goal could be accomplished by following recommendations:

- Installation of new centrifugal pump that could able to handle corrosive, toxic, abrasive concentrated slurry having rigid and coarse beads at vertical RIM suspensions loop
- If new centrifugal pump couldn't able solve the fluctuation in flow rate data for two-phase flow, compatible flow meter (9300-IMT96, Foxboro) is suggested
- Elimination of sharp lower bend could solve the issue of undeveloped flow
- Development of PIV recipe to encounter challenges such as very faint edge beads in front and behind of the plane, beads in the plane while processing PIV with RIM images to compute continuous phase fluid turbulence
- It would be a good idea to have some “marker” beads in the flow to analyze the dispersed phase turbulence using PTV in RIM slurry
- Once proper commissioning of vertical loop is completed along with PIV system. Additionally, PIV recipe or processing method is prepared to compute both continuous and disperse phase mean and turbulence statistics. For the first time,

turbulence modulation results could be achieved for 5 % concentrated slurry and 3 mm size beads

- Turbulence modulation investigation should be further extended for wide range of Reynolds number for 5 % concentrated slurry and 3 mm size beads
- Effect of different particle size and concentration on turbulence modulation should be studied for different Reynolds number
- Finally, development of a model to predict change of turbulence intensity of continuous phase in highly concentrated slurry flows for wide range of particle size, concentrations, and Reynolds number

## REFERENCES

- [1] M. C. Crowe, M. Sommerfeld and Y. Tsuji, “Multiphase flows with droplets and particles”, *CRC Press*, 1998.
- [2] S. A. Hashemi, “Velocity and concentration fluctuations in concentrated solid-liquid flows,” Thesis submitted at University of Alberta, 2013.
- [3] H. Tennekes, J. L. Lumley. “A first course in turbulence”, *MIT Press*; 1973.
- [4] S. Balachandar and J. K. Eaton, “Turbulent dispersed multiphase flow,” *Annu. Rev. Fluid Mech.*, vol. 42, no. 1, pp. 111-133, Jan. 2010.
- [5] C. C. Brennen, “Fundamentals of multiphase flows”. *Cambridge University Press*; 2005.
- [6] S. Geiß, A. Sadiki, A. Maltsev, A. Dreizler, and J. Janicka, “Investigations of Turbulence Modulation in Turbulent Particle Laden Flows,” *ZAMM - J. Appl. Math. Mech.*, vol. 81, no. S3, pp. 527–528, March 2001.
- [7] R. G. Gillies, “Pipeline flow of coarse particle slurries,” *Thesis submitted at University of Saskatchewan*, 1993.
- [8] S. Elghobashi, “On predicting particle-laden turbulent flows,” *Appl. Sci. Res.*, vol. 52, no. 4, pp. 309–329, 1994.
- [9] R. C. Chen and J. R. Kadambi, “Discrimination between solid and liquid velocities in slurry flow using laser Doppler velocimeter,” *Powder Technol.*, vol. 85, no. 2, pp. 127–134, Nov. 1995.
- [10] F. N. Krampa, "Two-fluid modelling of heterogeneous coarse particle" *Thesis submitted at University of Saskatchewan*. January, 2009.
- [11] A. Alajbegovic, A. Assad, F. Bonetto, R. T. Lahey JR, “Phase distribution and turbulence structure for solid/fluid upflow in a pipe,” vol. 20, no. 3, 1994.
- [12] Y. Tsuji, Y. Morikawa, and H. Shiomi, “LDV measurements of an air-solid two-phase flow in a vertical pipe,” *J. Fluid Mech.*, vol. 139, no. 1, p. 417, Apr. 1984.
- [13] C. T. Crowe, “On models for turbulence modulation in fluid-particle flows,” *Int. J. Multiph. Flow*, vol. 26, pp. 719-727, 2000.
- [14] S. Hosokawa and A. Tomiyama, “Turbulence modification in gas–liquid and solid–liquid dispersed two-phase pipe flows,” *Int. J. Heat Fluid Flow*, vol. 25, no. 3, pp. 489-498, Jun. 2004.
- [15] R. A. Gore and C. T. Crowe, “Effect of particle size on modulating turbulent intensity,” *Int. J. Multiph. Flow*, vol. 15, no. 2, pp. 279-285, 1989.
- [16] K. Kameyama, H. Kanai, H. Kawashima, and T. Ishima, “Evaluation of Particle Motion in Solid-Liquid Two-Phase Pipe Flow with Downward / Upward Flow Directions,” in *17th International Symposium on Applications of Laser Techniques to Fluid Mechanics Lisbon, Portugal*, 2014.

- [17] S. Sivakumar, M. Chidambaram, and H. S. Shankar, "On the Effect of Particle Size on Heat Transfer in Vertical Upflow of Gas-Solids Suspension," *Can. J. Chem. Eng.*, vol. 66, no. 1, pp. 1000-1004, 1988.
- [18] Y. Tsuji and Y. Morikawa, "LDV measurements of an air-solid two-phase flow in a horizontal pipe," *J. Fluid Mech.*, vol. 120, no. 1469-7645, pp. 384-409, 1982.
- [19] M. Sato, Y. Hanzawa, A. Hishida, K. and Maeda, "Interactions between particle wake and turbulence in a water channel flow," *Adv. Multiph. flow*, 1995.
- [20] K. T. Kiger and C. Pan, "Suspension and turbulence modification effects of solid particulates on a horizontal turbulent channel flow," *J. Turbul.*, vol. 3, no. 02, p. N19, 2002.
- [21] R. J. Adrian, "Twenty years of particle image velocimetry," *Exp. Fluids*, vol. 39, no. 2, pp. 159-169, Jul. 2005.
- [22] W. Merzkirch, "PIV in multiphase flow," The Second International Workshop on PIV'97-Fukui, Japan, pp. 165-171, July 8-11, 1997.
- [23] C. Brücker, "PIV in two phase flows." Lecture Series 2000-01 "Particle Image Velocimetry and associated techniques", pp. 1-28, 2000.
- [24] M. M. Cui and R. J. Adrian, "Refractive index matching and marking methods for highly concentrated solid-liquid flows," *Exp. Fluids*, vol. 22, no. 3, pp. 261-264, Jan. 1997.
- [25] S. Wiederseiner, N. Andreini, G. Epely-Chauvin, and C. Ancey, "Refractive-index and density matching in concentrated particle suspensions: a review," *Exp. Fluids*, vol. 50, no. 5, pp. 1183-1206, Nov. 2010.
- [26] Y. A. Hassan and E. E. Dominguez-Ontiveros, "Flow visualization in a pebble bed reactor experiment using PIV and refractive index matching techniques," *Nucl. Eng. Des.*, vol. 238, no. 11, pp. 3080-3085, Nov. 2008.
- [27] D. J. Wildman, J. M. Ekmann, J. R. Kadambi, and R. C. Chen, "Study of the flow properties of slurries using the refractive index matching technique LDV," *Powder Technol.*, vol. 73, no. 3, pp. 211-218, Dec. 1992.
- [28] Z. Peng, S. V. Ghatage, E. Doroodchi, J. B. Joshi, G. M. Evans, and B. Moghtaderi, "Forces acting on a single introduced particle in a solid-liquid fluidised bed," *Chem. Eng. Sci.*, vol. 116, pp. 49-70, Sep. 2014.
- [29] F. J. H. Gijzen, D. E. M. Palmén, M. H. E. Van Der Beek, F. N. Vosse, and M. E. H. Van Dongen, "Analysis of axial flow field in stenosed carotid-artery bifurcation models- LDA experiments," *J. Biomechanics*, vol. 29, no. 11, pp. 1483-1489, 1996.
- [30] B. Trifonov, D. Bradley, and W. Heidrich, "Tomographic reconstruction of transparent objects," *Eurographic Symposium on Rendering(2006)*, p. 55, 2006.
- [31] K. Bai and J. Katz, "On the refractive index of sodium iodide solutions for index matching in PIV," *Exp. Fluids*, vol. 55, no. 4, p. 1704, Mar. 2014.
- [32] P. Hutchinson, G. F. Hewitt, and A. E. Dukler, "Deposition of liquid or solid

- dispersions from turbulent gas streams: a stochastic model,” *Chem. Eng. Sci.*, vol. 26, no. 3, pp. 419–439, 1971.
- [33] R. A. Gore and C. T. Crowe, “Modulation of turbulence by dispersed phase,” *Journal of fluid engineering*, vol. 113, June, 1991.
- [34] T. Tanaka and J. K. Eaton, “Classification of turbulence modification by dispersed spheres using a novel dimensionless number,” *Phys. Rev. Lett.*, vol. 101, no. 11, pp. 1–4, 2008.
- [35] J. D. Kulick, J. R. Fessler, and J. K. Eaton, “Particle response and turbulence modification in fully developed channel flow,” *J. Fluid Mech.*, vol. 277, pp. 109–134, 1994.
- [36] S. L. Lee and F. Durst, “On the motion of particles in turbulent duct flows,” *Int. J. Multiph. Flow*, vol. 8, no. 2, pp. 125–146, 1982.
- [37] A. Y. Varaksin, Y. V. Polezhaev, and A. F. Polyakov, “Effect of particle concentration on fluctuating velocity of the dispersed phase for turbulent pipe flow,” *Int. J. Heat Fluid Flow*, vol. 21, pp. 562–567, 2000.
- [38] J. Kussin and M. Sommerfeld, “Experimental studies on particle behaviour and turbulence modification in horizontal channel flow with different wall roughness,” *Exp. Fluids*, vol. 33, no. 1, pp. 143–159, 2002.
- [39] R. Zissemler and O. Molerus, “Investigation of Solid-Liquid Pipe Flow with regard to Turbulence Modification,” *Chem. Eng. J.*, vol. 18, pp. 233–239, 1979.
- [40] F. Scarano, “Experimental Aerodynamics,” Course material at Delft university of Technology, February, 2013.
- [41] A. K. Prasad, “Particle image velocimetry,” *Review Article, Current science*, Vol 79, no. 1 pp. 51–60, July 2000.
- [42] R. J. Adrian, and J. Westerweel “Particle imaging velocimetry”, *Cambridge university press*, 2011.
- [43] R. Shokri, D. S. Nobes, S. Ghaemi, and R. S. Sanders, “Investigation of particle-fluid interaction at high Reynolds-number using PIV / PTV techniques,” *Int. Symp. Turbul. Shear Flow Phenomena*, pp. 7C–5:1–6, 2015.
- [44] R. Budwig, “Refractive index matching methods for liquid flow investigations,” *Exp. Fluids*, vol. 17, no. 5, pp. 350–355, Sep. 1994.
- [45] A. Averbakh, A. Shauly, A. Nir, and R. Semit, “Slow viscous flow of highly concentrated suspensions-Part I: Laser Doppler Velocimetry in Rectangular duct,” *Int. J. Multiph. Flow*, vol. 23, no. 3, pp. 409–424, 1997.
- [46] A. Zachos, M. Kaiser, and W. Merzkirch, “PIV measurements in multiphase flow with nominally high concentration of the solid phase,” *Exp. Fluids*, 1995.
- [47] J. M. Nouri, J. H. Whitelaw, and M. Yianneskis, “Particle Motion and turbulence in dense two-phase flows,” *Int. J. Multiph. Flow*, vol. 13, no. 6, pp. 729–739, 1987.

- [48] T. T. Nguyen, "A Method for Matching the Refractive Index and Kinematic Viscosity of a Blood Analog for Flow Visualization in Hydraulic Cardiovascular Models," *J. Biomech. Eng.*, vol. 126, no. 4, p. 529, Sep. 2004.
- [49] T. L. Narrow, M. Yoda, and S. I. Abdel-Khalik, "A simple model for the refractive index of sodium iodide aqueous solutions," *Exp. Fluids*, vol. 28, no. 3, pp. 282–283, Mar. 2000.
- [50] G. E. Jellison, L. A. Boatner, J. O. Ramey, J. a. Kolopus, L. A. Ramey, and D. J. Singh, "Refractive index of sodium iodide," *J. Appl. Phys.*, vol. 111, no. 4, p. 043521, 2012.
- [51] D. L. Jan, A. H. Shapiro, and R. D. Kamm, "Some features of oscillatory flow in model bifurcation," *American Physiological society*, 1989.
- [52] R. J. Harris, A. J. Sederman, M. D. Mantle, J. Crawshaw, and M. L. Johns, "A comparison of experimental and simulated propagators in porous media using confocal laser scanning microscopy, lattice Boltzmann hydrodynamic simulations and nuclear magnetic resonance," *Sci. Direct*, vol. 23, no. 2, pp. 355–357, Feb. 2005.
- [53] A. Aguilar-Corona, R. Zenit, and O. Masbernat, "Collisions in a liquid fluidized bed," *Int. J. Multiph. Flow*, vol. 37, no. 7, pp. 695–705, Sep. 2011.
- [54] P. Jean-franc, A. Abdenour, L. Fabrice, C. Sophie, and D. Jean, "Use of synchronised PIV to measure a pulsed flow velocity field in a discs and doughnuts column," in *10th International symposium on particle image velocimetry, Delft, Netherland*. 2013.
- [55] A. N. Bashkatov and E. a. Genina, "Water refractive index in dependence on temperature and wavelength: a simple approximation," *Opt. Technol. Biophys. Med. IV, 393*, vol. 5068, pp. 393–395, 2003.
- [56] E. Hecht, "Optics". *Pearson Education Limited*, 2015.
- [57] Properties of Borosicate glass bead, personal communication with Leon Parson, Chemglass Life Sciences, October 2014
- [58] N.P. Brown, N.I. Heywood, "Slurry handling: design of solid liquid system" *Elsevier Applied Science, London and New York* 1991.
- [59] MSDS, "Potassium Thiocyanate Solution, 1.0M," pp. 2008–2009, 2009.
- [60] Safety data sheet, "Silica particles," Potters Inc. p. 2008, 2008.
- [61] Safety data sheet, "Borosilicates glass beads," Sigma Aldrich Inc.
- [62] J. Kiijarvi, "Darcy Friction Factor Formulae in Turbulent Pipe Flow", *Lunowa Fluid Mech. Pap.*, pp. 1–11, 2011. *Fluid Mech. Pap.*, pp. 1–11, 2011.
- [63] J. Xu, Y. Wu, Z. Zheng, M. Wang, B. Munir, H. I. Oluwadarey, H. I. Schlaberg, and R. a. Williams, "Measurement of solid slurry flow via correlation of Electromagnetic Flow Meter, electrical resistance tomography and mechanistic modelling," *J. Hydrodyn. Ser. B*, vol. 21, no. 4, pp. 557–563, Aug. 2009.
- [64] X. Yuming and X. Zhiqiang, "Electromagnetic Flowmeter Measurement and

- Numerical Computation of Laminar Flow Transport Pipeline Flow Quantity,” *Second Int. Symp. Electron. Commer. Secur.*, pp. 169-173, 2009.
- [65] “Article on magnetic flowmeter fundamentals,” *Rosemount measurement*, September, 1995.
- [66] N. I. Heywood, and K. Mehta, “A survey of non-invasive flowmeters for pipelines flow of high concentration non-settling slurries,” *11<sup>th</sup> international conferecne on hydraulic transport of solids in pipes*, Belford, UK, pp131-55, October, 1988.
- [67] S. V. Ghatage, M. J. Sathe, E. Doroodchi, J. B. Joshi, and G. M. Evans, “Effect of turbulence on particle and bubble slip velocity,” *Chem. Eng. Sci.*, vol. 100, pp. 120–136, Aug. 2013.
- [68] R. P. King, “Introduction to practical fluid flow” Butterworth-Heinemann Press, 2002.
- [69] “Performance curve, Positive Displacement Rotary Pumps,” *Lobe pro company*. December, pp. 1–8, 2001.
- [70] “Product manual of Davis-8”, LaVision, GmbH.
- [71] M. P. Schultz and K. a. Flack, “Reynolds-number scaling of turbulent channel flow,” *Phys. Fluids*, vol. 25, no. 2, pp. 0-13, 2013.
- [72] J. Takeuchi, S. Satake, N. B. Morley, T. Yokomine, T. Kunugi, and M. A. Abdou, “PIV Measurements of turbulence statistics and near-wall structure of fully developed pipe flow at high Reynolds number,” *in 6<sup>th</sup> International symposium on particle image velocimetry California , USA*, pp. 1-9, Sept 2005.
- [73] D. Breakey, Y. K. Agrawal, P. Amini, S. Ghaemi, D. Nobes, R. S. Sanders, “Turbulence modulation in concentrated high-Reynolds-number solid-liquid flows”, *In Proceedings of the 9<sup>th</sup> International Conference on Multiphase Flow*, pp. 1-6, 2016.

## APPENDIX

### *Appendix A1: Clean-up procedure of the loop with fresh water*

Loop was cleaned with domestic cold water after all solution was delivered back to storage tank for future use. The purpose of cleaning the loop with fresh water is to wash up all the surfaces that were exposed with KSCN.

- 1) Open the valve V15. Close V15 when water in feed tank is at certain level 'C'.

All valves numbers are labelled in Figure 4.2.

- 2) Open V2, V3, V5, V7 and V8. Other valves must be closed
- 3) Run the slurry pump at a speed of 3 - 4 m/s.
- 4) Water will circulate in the loop as V7 opened and V6 closed. Once air has been taken out, wait for some time to rinse the overhead section. Open V6 and close V7.
- 5) Keep adding water from V15 while opening V20 and draining this water into the waste disposal tank with the help of the peristaltic pump.
- 6) -Open the valve V9 and V10 to flush the top vent line. Diluted KSCN solution will collect into pail. Open V4, V12 and V18 to flush the dampening pot.
- 7) Once loop is flushed, shut down the pump.
- 8) Open all valves and use the peristaltic pump to drain remaining diluted KSCN solution to the waste tank.

***Appendix A2: Reference check list to operate slurry loop***

Table A.1 illustrates valve numbers and their opening closing status at particular experimental operation procedure in the loop. All valve numbers are labelled in Figure 4.2. Symbols ‘O’ and ‘C’ are used for opened and closed valve positions respectively. Steps A - J represents steps followed in experimental operation procedure discussed in section 4.4.

Table A.1: Check list of valves at different step in procedure											
Steps Valve #	A	B	C	D <sub>Left</sub>	D <sub>Right</sub>	E	F	G	H	I	J
1	C	O	C	C	C	C	C	C	C	C	C
2	C	C	O	O	O	O	C	C	O	O	O
3	C	C	C	O	C	O	C	C	O	O	O
4	C	C	O	C	O	C	C	C	C	C	O
5	C	C	O	O	C	O	O	O	O	O	O
6	C	C	C	C	O	O	O	O	O	C	O
7	C	C	C	C	C	C	C	C	C	O	O
8	C	C	C	O	O	O	O	O	O	O	O
9	C	C	C	O	O	C	C	C	C	C	O
10	C	C	C	O	O	C	C	C	C	C	O
11	C	C	C	C	C	C	C	C	C	C	O
12	C	C	O	C	C	O	O	O	O	O	O
13	O	O	O	O	O	C	O	O	O	O	O
14	C	C	C	C	C	C	C	O	O	O	C
15	C	C	C	C	C	C	C	C	C	C	C
16	C	C	C	C	C	C	O	O	C	C	C
17	C	C	C	C	C	C	O	O	C	C	C
18	C	C	O	C	C	C	C	C	O	C	O
19	OPENS AUTOMATICALLY IN CASE OF EMERGENCY										
20	C	C	C	C	C	C	C	C	C	C	O
21-27	C	C	C	C	C	C	C	C	C	C	C

V21 - V27 includes valve numbers 21, 22, 23, 24, 25, 26 and 27 all. V19 is a pressure relief valve which opens in case of emergency.

### ***Appendix A3: Standard operational procedure for pressure loss measurement***

De-aerated water was used for pressure loss measurement across two pressure taps in the downside of the loop as mentioned in Figure 4.1. Domestic hot water of 50 °C was fed into the feed tank. Water was allowed to cool down overnight to reduce the dissolved air content in the water. The purging and bleeding procedure of the differential pressure transducer is following:

- 1) Charge the loop as mentioned in section 4.4 (Steps: C and D).
- 2) Pressurize the loop at 40 psi as mentioned in section 4.4 (Step: F).
- 3) Make sure that V1, V2, V3, V4, V7, V9, V10, V11, V18 and V20 are closed. Valves V5, V6, V8, V12, V16, and V17 must be opened. Valves are labelled in Figure 4.2
- 4) V21, V22, V23, V24, V25, V26 and V27 are closed.
- 5) Open V21 and V23 for the high pressure side. Close V21 and V23 when water starts coming out. Now open V22 and V24 for the low pressure side. Close V22 and V24 when water starts coming out.
- 6) Open V22, V26, V27, V25 and then V23 in sequence to purge the air from the polyline connected to the differential pressure transducer.
- 7) Close V23 when water starts to come out. This process makes sure that all air is being purged.
- 8) Partially open the bleed screws as shown in Figure 4.2 on the high pressure and low pressure side to remove any remaining air in the pressure transducer cell.

- 9) Once purging and bleeding is done, close V27. Now the system is ready for recording pressure measurements.